Glacial Processes on Earth and Mars:

New Perspectives from Remote Sensing and Laboratory Analyses

by

Alicia Marie Rutledge

A Dissertation Presented in Partial Fulfillment
of the Requirements for the Degree
Doctor of Philosophy

Approved April 2015 by the
Graduate Supervisory Committee:

Philip Christensen, Chair
Everett Shock
Amanda Clarke
Thomas Sharp
Kelin Whipple

ARIZONA STATE UNIVERSITY

May 2015

ABSTRACT

Chemical and physical interactions of flowing ice and rock have inexorably shaped planetary surfaces. Weathering in glacial environments is a significant link in biogeochemical cycles – carbon and strontium – on Earth, and may have once played an important role in altering Mars' surface. Despite growing recognition of the importance of low-temperature chemical weathering, these processes are still not well understood. Debris-coated glaciers are also present on Mars, emphasizing the need to study ice-related processes in the evolution of planetary surfaces. During Earth's history, subglacial environments are thought to have sheltered communities of microorganisms from extreme climate variations. On Amazonian Mars, glaciers such as lobate debris aprons (LDA) could have hosted chemolithotrophic communities, making Mars' present glaciers candidates for life preservation. This study characterizes glacial processes on both Earth and Mars.

Chemical weathering at Robertson Glacier, a small alpine glacier in the Canadian Rocky Mountains, is examined with a multidisciplinary approach. The relative proportions of differing dissolution reactions at various stages in the glacial system are empirically determined using aqueous geochemistry. Synthesis of laboratory and orbital thermal infrared spectroscopy allows identification of dissolution rinds on hand samples and characterization of carbonate dissolution signals at orbital scales, while chemical and morphological evidence for thin, discontinuous weathering rinds at microscales are evident from electron microscopy. Subglacial dissolution rates are found to outpace those of the proglacial till plain; biologically-mediated pyrite oxidation drives the bulk of this acidic weathering.

Second, the area-elevation relationship, or hypsometry, of LDA in the midlatitudes of Mars is characterized. These glaciers are believed to have formed ~500 Ma during a climate excursion. Hypsometric measurements of these debris-covered glaciers enable insight into past flow regimes and drive predictions about past climate scenarios. The LDA in this study fall into three major groups, strongly dependent on basal elevation, implying regional and climatic controls on ice formation and flow.

I show that biologically-mediated mineral reactions drive high subglacial dissolution rates, such that variations within the valley can be detected with remote sensing techniques. In future work, these insights can be applied to examining Mars' glacial regions for signs of chemical alteration and biosignatures.

DEDICATION

To my grandfathers

for the lessons they taught me.

ACKNOWLEDGMENTS

I could not have completed my graduate work without the help of many people. First I would like to thank Phil Christensen for taking a chance on an aerospace engineer and introducing me to planetary geology. I must also thank Everett Shock for turning me (occasionally without consulting me) into a part-time geochemist and a full-time field junkie. Thank you to Amanda Clarke, Kelin Whipple, and Tom Sharp, as well as the late Ronald Greeley, for the stellar geology education I've received at ASU. To Henrietta Cathay, for helpful discussions on electron microscopy methods and interpretations. To my fellow graduate students and collaborators for helpful discussions and immense support along the path, including but not limited to Briony Horgan, Christopher Edwards, Elizabeth Rampe, Lauren Edgar, Melissa Bunte, Kristen Paris, Jeff Havig, Trinity Hamilton, Eric Boyd, Peter Canovas, Natalie Hinkel, Kristen Bennett, Marina Foster, Rebecca Smith, Michael Veto, Scott Dickenshied, and many others at the Mars Space Flight Facility and SESE. To Tara Fisher and other administrative staff, for making the business side of science immensely less stressful. Thank you to my dear friends, Tiffany Cook and Amanda Lampton, for believing in me for all these years. I would like to thank my family, especially my parents and brother, for their unwavering support, encouragement, and love. Finally, thank you to my husband, Jean-François, for reading more glacial weathering-related papers than any other volcanologist should ever have to.

This work was supported by the NASA Earth and Space Science Fellowship, and through grants associated with NASA's THEMIS instrument aboard the spacecraft Mars Odyssey.

TABLE OF CONTENTS

Page

Page

CHAPTER

Page

APPENDIX

LIST OF TABLES

LIST OF FIGURES

Figure Page

CHAPTER 1

INTRODUCTION

Approximately 10% of terrestrial landmass on Earth and up to 30% of Mars's surface is covered by ice. The interactions of flowing ice with rock - chemical and physical - are inexorably shaping the surfaces of planets in our solar system. Chemical weathering in glacial environments is a significant link in biogeochemical cycles, such as the carbon cycle and the strontium cycle, on Earth, and may have once played an important role in altering Mars' surface. Despite growing recognition in recent years of the importance of low-temperature chemical weathering in terrestrial glaciated catchments, the mechanisms controlling these processes are still not well understood [*Anderson*, 2007]. On Mars, the importance of midlatitude icy deposits has only recently been recognized [*Head et al.*, 2005; *Holt*, 2008; *Fastook et al.*, 2011; *Levy et al.*, 2015]. Glaciers on Earth are reservoirs of water, powerhouses of mechanical and chemical weathering, and storehouses of nutrients in global biogeochemical cycles [*Anderson et al.*, 2000]. In past climates (*i.e.* Snowball Earth), subglacial environments are thought to have sheltered communities of microorganisms from extreme climate variations [*Hamilton et al.*, 2013]. Diverse and active microbiomes persist today, using the continual exposure of fresh mineral surfaces at the glacier bed for energy. On Amazonian Mars, approximately 500 million years ago, glacial ice could have potentially hosted similar chemolithotrophic communities, making Mars' present-day glaciers especially significant to astrobiology. In this study we characterize glacial processes on Earth and Mars.

Glacial erosion is thought to be primarily driven by physical processes such as abrasion, fracture, and plucking, but in recent years the relative importance of chemical weathering at cold temperatures has been studied.

Chapters 2 through 4 examine the weathering system of Robertson Glacier, Alberta, Canada. This alpine glacier is of key interest in past chemical and astrobiological studies due to the documented presence of subglacial microbes, some of which are thought to oxidize pyrite and add sulfuric acid to the system [*Sharp et al.*, 2002; *Hamilton et al.*, 2013; *Boyd et al.*, 2014]. Chapter 5 examines debris-covered glacial features on Mars, past flow regimes, and distribution with respect to elevation as signal of past climate.

Chapter 2 quantifies the weathering regime of Robertson Glacier using aqueous geochemical methods. The study demonstrates that, through iterative methods, cation abundances in solution can be transformed into quantifiable mineral abundances. This makes it possible to determine the minerals being actively weathered, and by which process. The study finds that the subglacial system is dominated by carbonate dissolution through sulfuric acid coupled with pyrite oxidation, and the proglacial system is dominated by carbonic acid dissolution of carbonate minerals. These findings imply that the proglacial moraine is an oxygen-limited system with a slower overall weathering rate, while the regularly replenished glacier bed has a relatively faster overall rate of weathering, contributing to overall erosion of the alpine valley.

Chapter 3 demonstrates the utility of remote sensing data for the study of chemical weathering in inaccessible regions such as alpine glaciated valleys. Thermal

infrared (TIR) laboratory spectroscopy is used to characterize the weathering of cobbles in the glacial foreground, in the subglacial environment, and in supraglacial debris. Laboratory spectra indicate the formation of leached weathering rinds compared to inner, less weathered rock, due to dissolution of carbonate minerals from the surfaces of rocks. TIR remote spectra from the Advanced Spaceborne Thermal Emission and Reflection Radiometer (ASTER) instrument show that this "leaching" signature can be detected from orbital imagery at 90 m resolution. The methods developed in this chapter can be used to explore inaccessible, alpine or Arctic glaciated regions for weathering signatures.

Chapter 4 shows that discontinuous weathering rinds characterize the surfaces of clastic-carbonate cobbles from Robertson Glacier. These rinds are porous, thin, and form through preferential dissolution of carbonate minerals. Weathering rind voids are strongly associated with the oxidation of pyrite, indicating possible dissolution by sulfuric acid in localized microenvironments. Their overall thickness is most likely controlled by low-temperature reactions rates, fluid flow rates, and glacial comminution.

Chapter 5 explores the distribution of large glacial features in the midlatitudes of Mars. Lobate debris aprons (LDA) are icy features around scarps in several locations on the planet and subsequently experienced viscous flow. They are estimated to contain the largest nonpolar ice reservoir on the surface of Mars [*Levy et al.*, 2014]. They are thought to have formed during past climate excursions between 700 and 100 Ma and subsequently became covered in debris during the end of their emplacement, armoring the surfaces and preventing or slowing sublimation to the atmosphere [*Fastook et al.*, 2014].

Recent studies have found that mountain glacier loss since the 1970s has accelerated due to human influences on climate change [*Marzeion et al.*, 2014]. Additionally, in recent years, glaciers' significance as both agents of weathering and role as living ecosystems has begun to be recognized. Glacier beds are active, dynamic weathering systems, harboring diverse communities of chemolithotrophic microorganisms, and they have a detectable effect on large-scale weathering signatures. The rate of loss of glacial ice will translate into the effective loss of habitat for subglacial microbial communities, and in turn change the weathering budget of formerly-glaciated catchments. Thus, the major goals of the project are to quantify weathering inputs to the glacial energy budget, to link in situ sampling with remote sensing capabilities, and to use remote sensing to inform our knowledge of glacial flow on the surface of Mars.

CHAPTER 2

AQUEOUS GEOCHEMISTRY OF ROBERTSON GLACIER

2.1. Introduction and Background

Glaciers and ice fields currently cover approximately 10% of the Earth's land surface [*Mitchell et al.*, 2013] and have a significant impact on global biogeochemical cycles, in particular through the comminution of bedrock and chemical weathering [*Anderson*, 2007]. Glacial chemical weathering is also of importance for study because of the potential for negative feedbacks to global climate through the carbon cycle [*Sharp et al.*, 1995] and association with extremophile life [*Boyd et al.,* 2010; *Boyd et al.*, 2011]. The low temperatures, anoxic conditions, and lack of light in subglacial environments promote unique weathering pathways that can produce alteration minerals including weathering rinds, sulfates, iron oxides, carbonate and silica coatings, and poorly crystalline phases [*Hallet*, 1975, 1976; *Whalley et al.,* 1990; *Mitchell et al.*, 2001; *Wadham et al.*, 2007; *Raiswell et al.*, 2009, *Rutledge and Christensen*, 2012].

Past studies have used aqueous geochemistry of glacial melt to investigate glacial weathering [*Anderson et al*., 2000; *Tranter,* 2003; *Fortner et al*., 2005; *Anderson*, 2007; *Wadham et al.*, 2007]. Studies of glacier outwash stream chemistry and marginal glacier sediment microbial communities have found that subglacial weathering pathways are closely linked to microbially-mediated redox reactions [*Bottrell and Tranter*, 2002; *Skidmore et al.*, 2005]. Abundant and active microbial populations have been shown to inhabit the persistently cold environments in terrestrial ice, marginal subglacial sediments, and proglacial meltwaters [*Sharp et al.*, 1999, *Skidmore et al.,* 2000, 2005;

Boyd et al., 2011, *Hamilton et al.*, 2013] and are thought to be primarily supported through chemotrophic redox reactions involving iron sulfide minerals, resulting in weathering of the underlying bedrock [*Sharp et al*., 1999; *Tranter et al.,* 2002; *Skidmore et al.*, 2005].

Carbonate dissolution has been found to dominate solute fluxes from glaciated catchments [*Sharp et al.*, 1995; *Fairchild et al.*, 1999a; *Hodson et al.*, 2002; *Anderson*, 2007]. However, in many of these cases, carbonate minerals comprise only a few percent of the bedrock. The disproportionate amount of carbonate dissolution is most likely due in part to the roughly five orders of magnitude difference in rate constants between carbonate and silicate minerals [*Anderson*, 2007]. Other potential reasons for the mismatch include a disproportionate amount of calcite (Moh's hardness of 3) being ground into powder with a relatively larger surface area through glacial action, and the fact that calcite dissolution is less sensitive to temperature effects than silicates under otherwise equal conditions [*Morse and Arvidson*, 2002].

Sulfide oxidation is the next most important process in subglacial environments [*Sharp et al.*, 1995; *Anderson*, 2007]. Trace amounts of sulfide minerals have been found to contribute a disproportionate amount of solute flux in glaciated valleys, much like carbonate minerals [*Sharp et al.*, 1995; *Sharp et al.*, 2002; *Anderson et al.*, 2003]. Sulfide oxidation provides protons that drive additional carbonate weathering, leading to significantly enhanced amounts of dolomite and calcite being dissolved [*Sharma et al.*, 2013]. Sulfide oxidation is closely linked to subglacial microbial community processes [*Hamilton et al.*, 2013; *Mitchell et al.*, 2013].

Research on carbonate systems has shown that in subglacial environments, chemical weathering is dominated by coupled pyrite oxidation and carbonate dissolution [*Fairchild et al.*, 1994; *Tranter*, 1996; *Anderson et al.,* 2000; *Tranter*, 2003; *Szynkiewicz et al.,* 2013]. As this study is in a primarily carbonate ($CaCO_3$, calcite and $CaMg(CO_3)_2$, dolomite) catchment with evidence for pyrite oxidation [*Sharp et al.*, 2002; *Skidmore et al.*, 2005], we assume that the bulk of solutes in solution are controlled by the following reactions:

Calcite dissolution by carbonic acid:

$$CaCO_{3(s)} + CO_{2(g)} + H_2O \rightarrow Ca^{+2}_{(aq)} + 2HCO_3^-{}_{(aq)} \quad (1)$$

Dolomite dissolution by carbonic acid:

$$CaMg(CO_3)_{2(s)} + 2CO_{2(g)} + 2H_2O \rightarrow Ca^{+2}_{(aq)} + Mg^{+2}_{(aq)} + 4HCO_3^-{}_{(aq)} \quad (2)$$

Calcite dissolution by sulfuric acid:

$$FeS_{2(s)} + 2CaCO_{3(s)} + \tfrac{1}{2}\, H_2O + 15/4\, O_{2(g)} \rightarrow$$
$$2Ca^{+2}_{(aq)} + 2CO_2^-{}_{(g)} + 2SO_4^{-2}{}_{(aq)} + FeOOH_{(s)} \quad (3)$$

Dolomite dissolution by sulfuric acid:

$$FeS_{2(s)} + CaMg(CO_3)_{2(s)} + 3/2\, H_2O + 15/4\, O_{2(g)} \rightarrow$$
$$Ca^{+2}_{(aq)} + Mg^{+2}_{(aq)} + 2CO_2^-{}_{(g)} + 2SO_4^{-2}{}_{(aq)} + H_2O_{(aq)} + FeOOH_{(s)} \quad (4)$$

Robertson Glacier valley presents a unique testbed to untangle these acid dissolution reactions with respect to acid sources and types of carbonates minerals.

2.2. Materials and Methods

2.2.1 Field Site Description

Robertson Glacier (50˚44'N, 115˚20'W) is one of two northern drainages of the Haig Icefield in Peter Lougheed Provincial Park, Kananaskis Country, Alberta, Canada. The glacier is approximately 2 km long, spans an elevation range from 2370 to 2900 m, and terminates on a flat till plain with glacially smoothed bedrock surfaces exposed along the glacier margins (Figure 3.1).

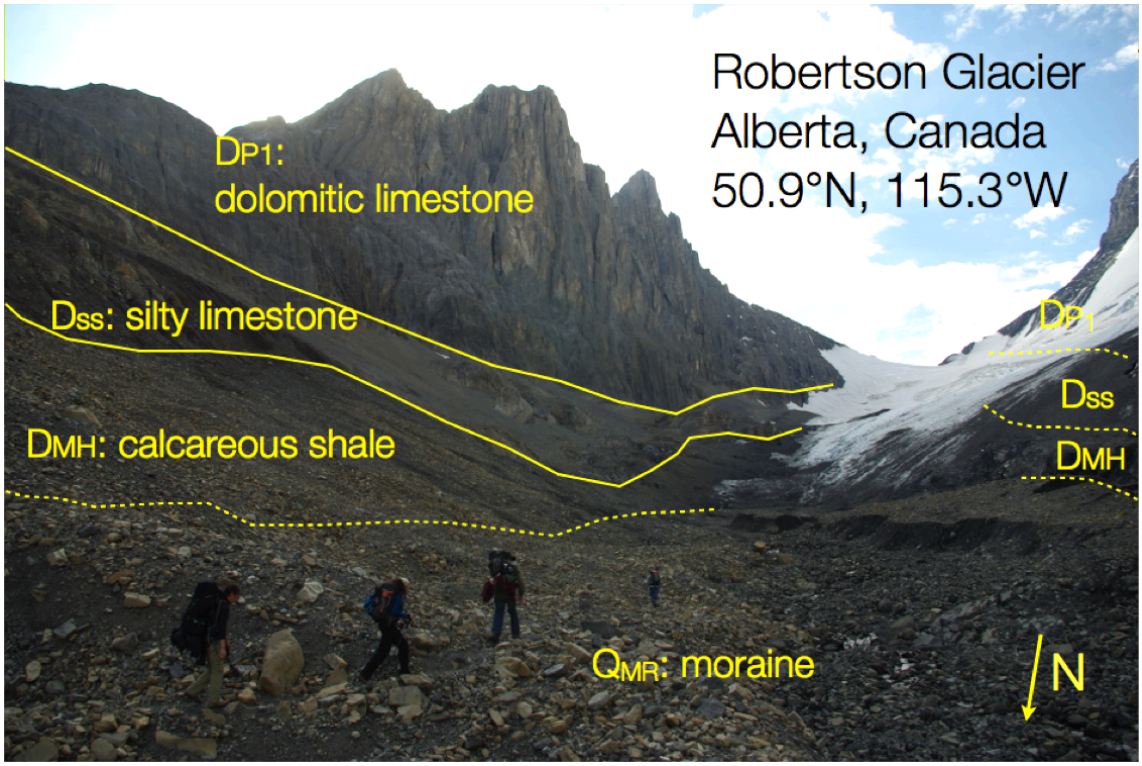

Figure 2.1. View south from Robertson Glacier moraine. Major geologic units and contacts labeled (inferred contacts under ice labeled with dashed lines). D_{MH}: Mount Hawk Formation; D_{SS}: Sassenach Formation; D_{Pl}: Lower unit of the Palliser Formation. Geochemists for scale.

The glacial valley follows a NW-SE trending upright anticline, exposing three Upper Devonian units on both walls: the Mount Hawk Formation (D_{MH}), overlain by the Sassenach Formation (D_{SS}), which is in turn overlain by the lower unit of the Palliser Formation (D_{P1}) [*McMechan*, 1988]. These units, part of the Winterburn Group, were deposited in the Western Canada Sedimentary Basin during the Late Devonian (~380 mya) during a series of marine transgressions and regressions [*Switzer et al.*, 2012] and subsequently folded by the Bourgeau Thrust Fault. This regional thrust fault also resulted

in small associated normal faults [*McMechan*, 1988]. Glacial action has enlarged and eroded the valley; lateral moraines form the neoglacial moraine deposits (Q_{MR}) identified by *McMechan* [1988]. These units are labeled in Figure 2.1.

The oldest unit, the Mount Hawk Formation, forms the floor of the valley and is composed of calcareous shale and argillaceous limestone. Bedrock surfaces crop out in places through the till plain. The Sassenach Formation, composed of interbedded quartzose siltstone and silty limestone, rests unconformably on the Mount Hawk Formation to form the lower elevation slopes of the valley. The Sassenach Formation, also known as the Upper Gramima Silt, represents one of the most significant global mass extinction events of the Phanerozoic [*Switzer et al.*, 2012]. The clastic component of the Sassenach Formation is thought to represent marine-reworked detrital/windblown material deposited in the Western Canada Sedimentary Basin [*McLaren and Mountjoy*, 1962]. The lower unit of the Palliser Formation, which weathers to form the highest elevation cliffs, is composed primarily of massive dolomitic limestone.

Robertson Glacier has eroded the valley walls and deposited recent lateral and ground moraines. The ground moraine is at present being downcut by glacial outwash streams, leaving perched terraces composed of poorly sorted sedimentary deposits. The till terraces contain rock types representing all three major bedrock units, indicating an upstream, glacially-transported origin. Robertson Glacier itself also has a discontinuous coating of supraglacial debris, consisting of bands of englacial rock and sediment exposed through ablation, as well as several recent rockfall deposits. The rockfall deposits are identifiable by morphology and proximity to the glacier margins.

2.2.2 Meltwater Collection and Analyses

Meltwaters were collected from Robertson Glacier on 11 September 2009, 14 October 2010, and 25 September 2011. Sample locations are outlined in Figure 2.2. Water was filtered immediately in the field through a series of 0.8 and 0.2-mm filters (Supor, made of hydrophilic polyether-sulfone, Pall Scientific). Samples were collected after the filters were flushed with 20 ml of sample to minimize contamination. Samples for ion chromatography analysis of major ions were stored in 60-ml polypropylene bottles that were acid-washed, cleaned, and oven-dried before use in the field. pH and temperature were measured in the field using a WTW 330i meter and probe, and conductivity and temperature were measured with a YSI 30 conductivity meter. Alkalinity was determined with a Hach Digital Titrator, and dissolved oxygen was measured in the field with an AccuVac Ampule in a Hach DR/2400 Portable Spectrometer. A field blank (18.2 MW deionized water brought to the field in a 1-liter Nalgene bottle) was sampled using the equipment described above.

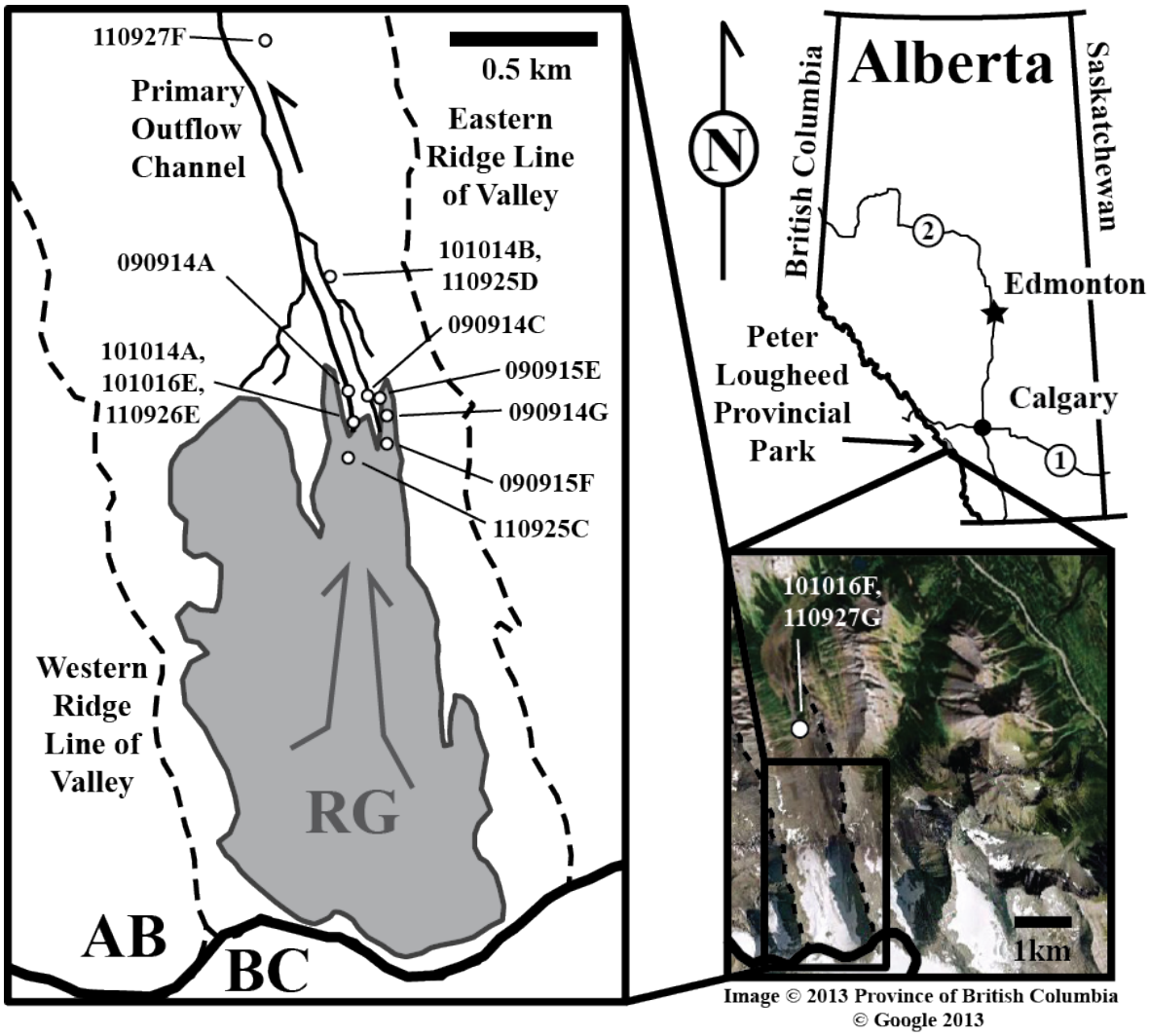

Figure 2.2. Location map of Robertson Glacier and Peter Lougheed Provincial Park within Alberta, Canada. Water sample locations labeled along the outwash stream, on glacier ice (shaded gray), and farther down-valley. AB = Alberta; BC = British Columbia.

Dissolved inorganic cation (Ca^{+2}, Mg^{+2}, Na^{+}, K^{+}) and anion (Cl^{-}, SO_4^{-2}, F^{-}, and NO_3^{-}) concentrations were measured using ion chromatography (anions: Dionex DX 600 Dual IC System; cations: Dionex DX 120 IC System). Certified standards were used to quantify cations and anions (Dionex Combined 6 Cations Standard II and Alltech

Multicomponent Certified Anion Standard Mix 6). Standard deviations (RSD%) for IC values were based upon duplicate analyses. Dissolved organic and inorganic carbon was determined by elemental analysis coupled to isotope-ratio mass spectrometry. Alkalinity (HCO_3^-) was also calculated by charge balance using methods similar to *Lafreniere and Sharp* [2005]. All ions and field blank compositions are reported in Appendix A. Ions of particular interest to this study are reported in Table 2.1.

Table 2.1. Water Compositions of Interest at Robertson Glacier

		Concentrations in mM						
Location	Sample #	Ca^{+2}	RSD %	Mg^{+2}	RSD %	SO_4^{-2}	RSD%	HCO_3^-*
Subglacial	090914C	0.329	2.18	0.038	1.53	0.033	0.24	0.647
	090915E	0.331	1.66	0.030	1.66	0.023	0.62	0.671
	101014A	0.675	0.03	0.284	0.02	0.571	0.09	0.746
	101016E	0.595	0.03	0.245	0.09	0.461	0.42	0.725
	110925A	0.405	1.44	0.060	2.41	0.111	0.91	0.702
	110926E	0.390	1.49	0.129	1.31	0.187	6.05	0.650
Side seeps	101014B	0.720	0.02	0.448	0.04	0.403	0.33	1.500
(Proglacial)	110925D	0.472	0.68	0.486	0.58	0.390	0.16	1.078
	110927F	0.559	0.44	0.544	0.38	0.446	0.14	1.311
	110927G	0.383	0.08	0.117	0.34	0.065	0.31	0.881
Outwash	090914A	0.337	0.64	0.044	0.25	0.075	0.05	0.606
stream	101016F	0.825	0.04	0.439	0.04	0.531	0.07	1.445
Snow	101015C	0.003	3.29	0.000	0.00	0.002	0.92	0.000
&	101016H	0.056	0.21	0.000	0.00	0.004	0.45	0.078
Ice melt	101016G	0.099	0.29	0.005	0.21	0.003	0.30	0.190
	090915F	0.221	0.80	0.008	0.24	0.001	2.12	0.452
	090915G	0.513	1.76	0.078	1.47	0.055	0.09	1.066
	110925C	0.290	4.11	0.018	5.70	0.001	1.51	0.658

Associated field blanks subtracted from each sample.
RSD = instrument error
*$HCO3^-$ calculated from charge balance (Appx. A)

2.2.3 Solute Source Tracking

Table 2.1 and Appendix A show that the dominant (by an order of magnitude) ions in solution are associated with carbonate dissolution reactions. If we assume that these reactions, defined in Section 2.1, control the bulk of observed solutes, it can be seen that Equations (1) and (2), carbonic acid weathering of carbonate minerals, result in anion:cation ratios of 1:2, while reactions (3) and (4), sulfuric acid dissolution of carbonate minerals due to oxidation of pyrite, result in anion:cation ratios of 1:1. Figure 2.3 illustrates these ratios with measurements (corrected for snow/ice contribution to solute totals) from Table 2.1 overlain. All measurements plot between the end-members of carbonic acid dissolution and sulfuric acid dissolution, implying that both processes are active in the Robertson Glacier catchment.

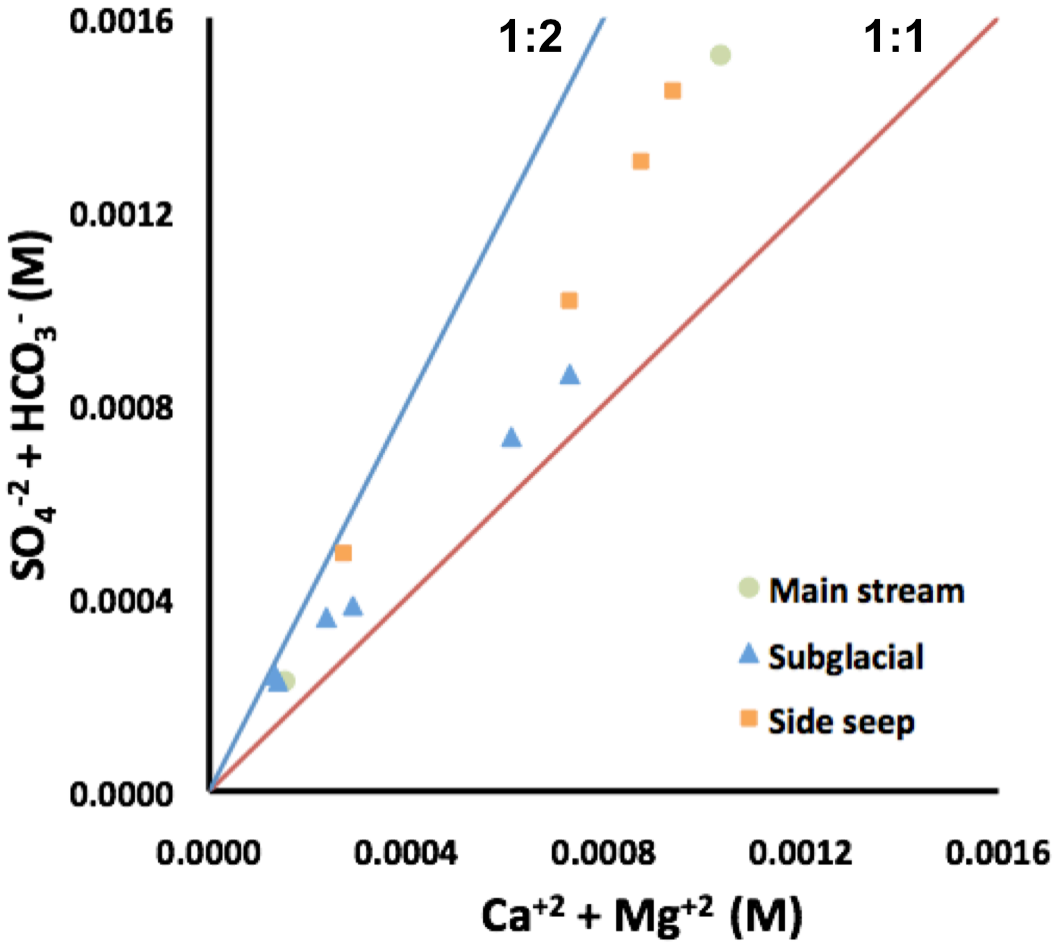

Figure 2.3. Subglacial (blue), side seep or proglacial (orange), and main outwash stream (green) measurements of total major cations ($Ca^{+2} + Mg^{+2}$) are plotted versus total major anions ($SO_4^{-2} + HCO_3^-$). Measurements have maximum snow/ice solute contributions subtracted (see Table 2.1). These measurements all plot between the ratios outlined for carbonic acid dissolution (1:2, blue) and sulfuric acid dissolution (1:1, red).

The relative contribution of each reaction (Eq. 1-4) to the abundance of each ion is empirically determined through the following method. Measured solutes are compared

to solute ratios that should result from the occurrence of each reaction. Cations are compared to other cations (Figure 2.4), cations to anions (Figures 2.5 – 2.8), and anions in solution are compared to each other (Figure 2.9). The relative ratios of measured ions are compared to those expected for the dissolution of calcite and dolomite by different acids (Eq. 1-4).

An example of this ion ratio method is shown in Figure 2.4. When idealized dolomite (i.e. a mineral composition of equal amounts of calcium and magnesium, $CaMg(CO_3)_2$) dissolves, equal proportions Ca^{+2} and Mg^{+2} are released into solution, moving abundances up the 1:1 line (Figure 2.4B). When calcite ($CaCO_3$) dissolves, only Ca^{+2} is released into solution. Abundances would plot to the right of the 1:1 line (Figure 2.4C). Measured subglacial samples in this study plot to the right of the 1:1 line, indicating both calcite and dolomite dissolved during weathering (Figure 2.4D). If calcite is precipitated out of solution, Ca^{+2} is removed from the system. Abundances would then plot closer to or to the left of the 1:1 line (Figure 2.4E). Measured side seep samples in this study plot close to or to the left of the 1:1 line, indicating calcite deposition at these sites. Distance to the left of the line is taken as the "minimum precipitated calcite" for those samples (Figure 2.4F). Similar plots, shown in Figures 2.5 – 2.9, of major cations (Ca^{+2}, Mg^{+2}) vs. major anions (HCO_3^-, SO_4^{-2}) were used to methodically work through all possible combinations of Equations 1-4.

This method is iteratively applied to a series of such proportionate plots until a solution is found that satisfies all four defining equations.

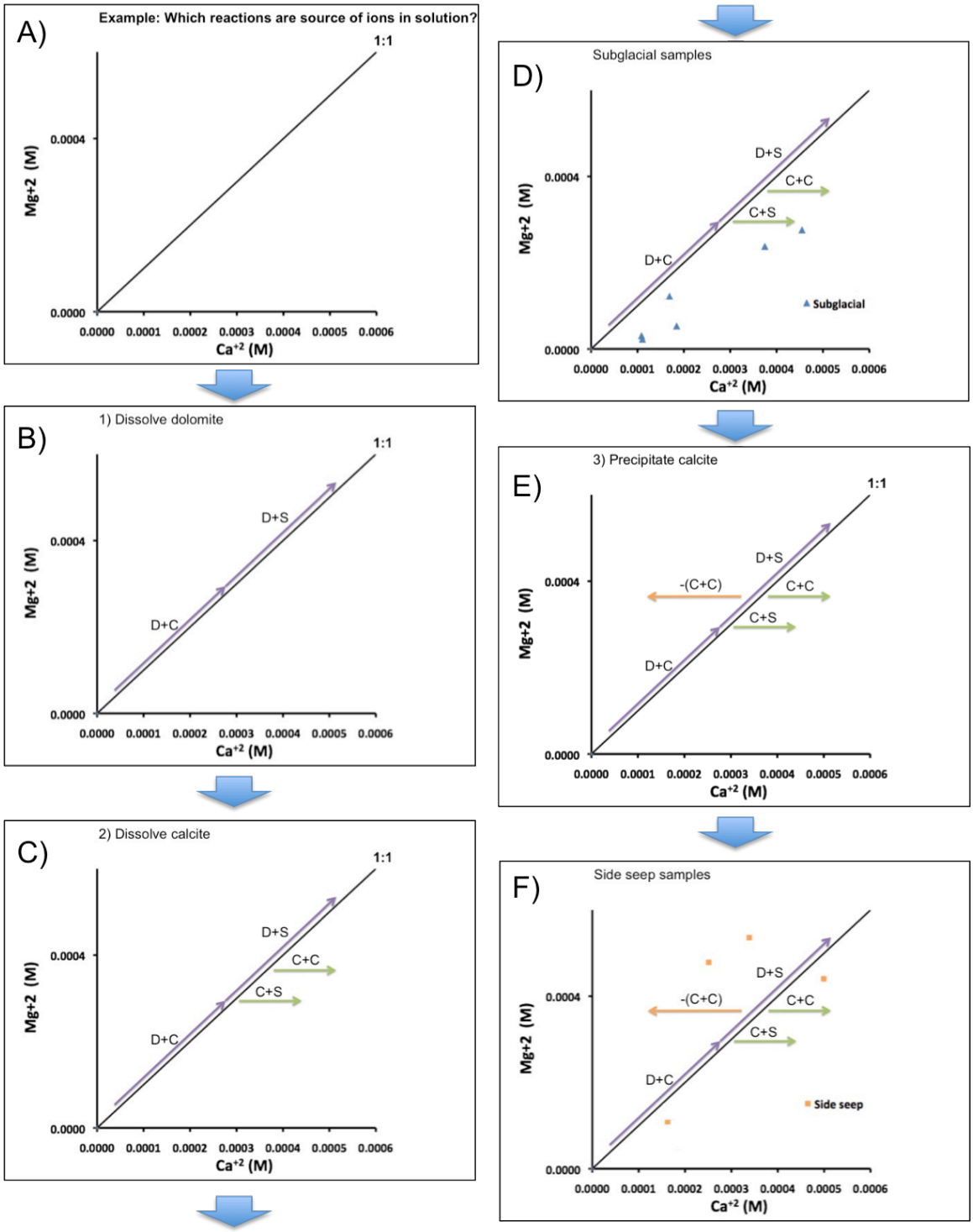

Figure 2.4. Flowchart showing iterative plots for Ca^{+2} vs. Mg^{+2} ions as an example of the empirical method of determining relative reaction contributions of each major solute.

Figure 2.4 (cont'd). "C+C" = carbonic acid dissolution of calcite; "D+C" = carbonic acid dissolution of dolomite; "C+S" = sulfuric acid dissolution of calcite; and "D+S" = sulfuric acid dissolution of dolomite.

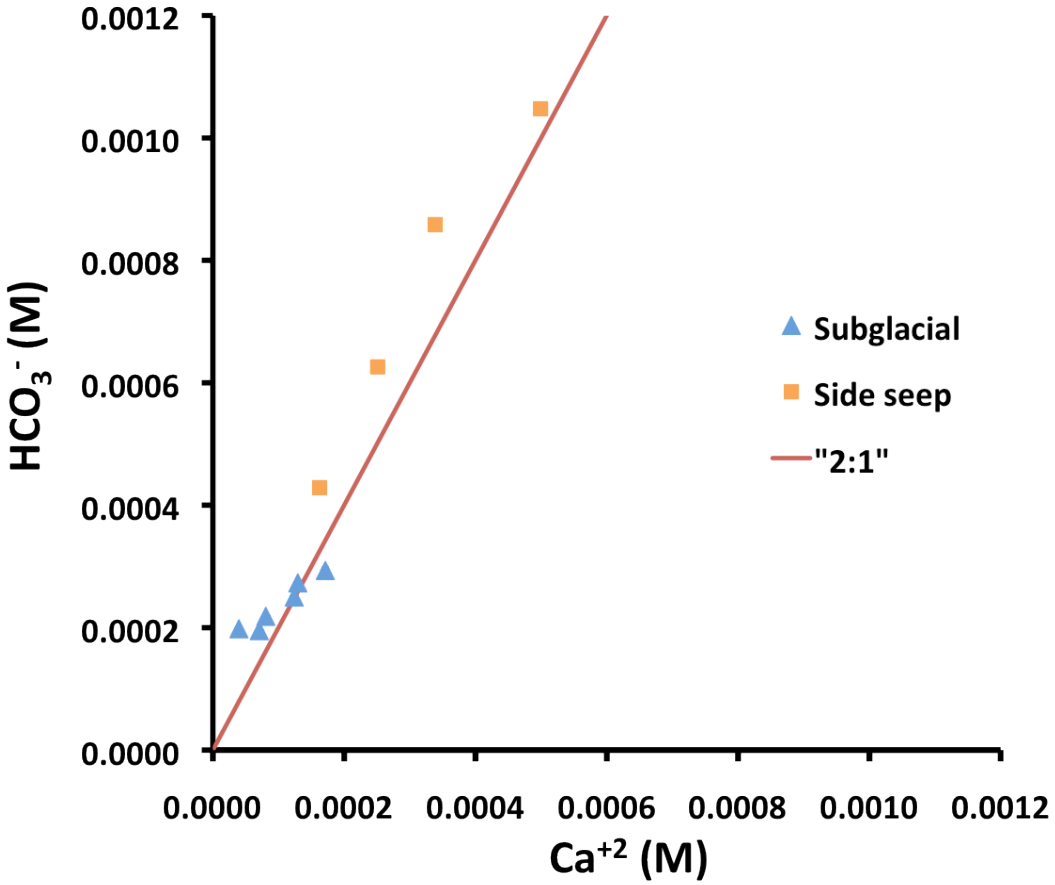

Figure 2.5. Ca^{+2} vs HCO_3^- abundances for subglacial meltwaters and proglacial "side seep" waters at Robertson Glacier. The 2:1 anion:cation ratio line indicates carbonic acid dissolution of calcite.

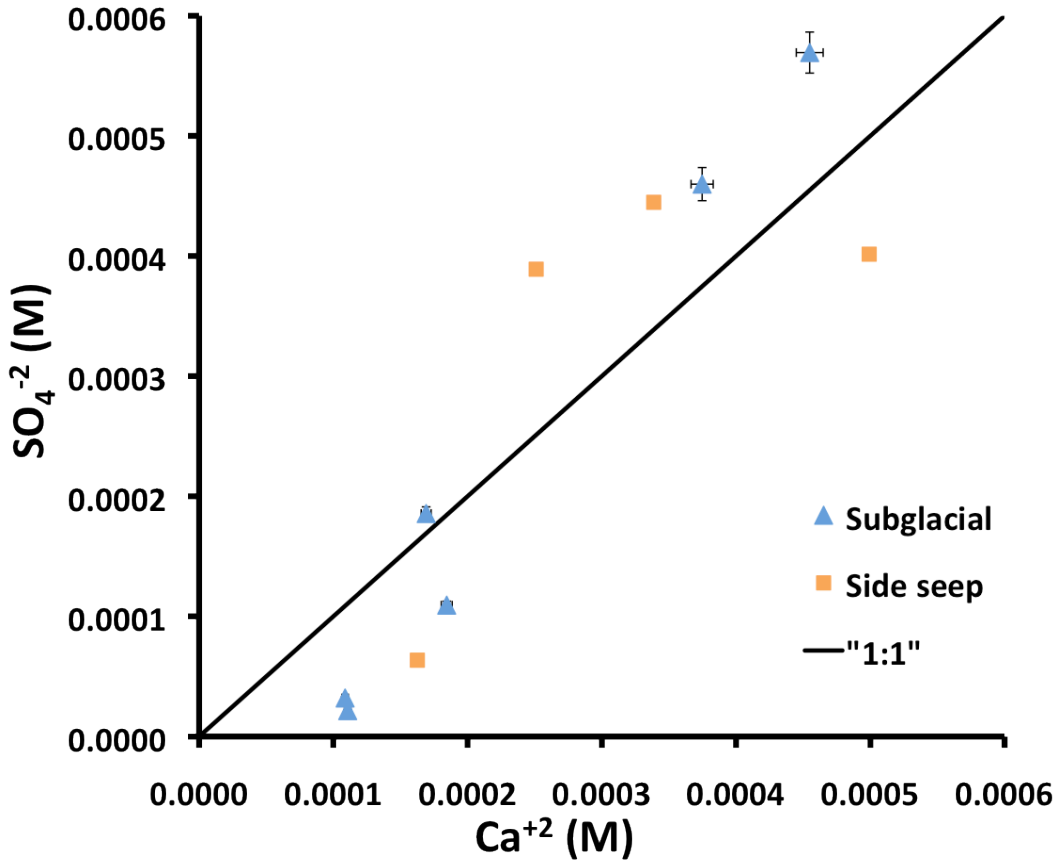

Figure 2.6. Ca^{+2} vs SO_4^{-2} abundances for subglacial meltwaters and proglacial "side seep" waters at Robertson Glacier. The 1:1 anion:cation ratio line indicates sulfuric acid dissolution of calcite.

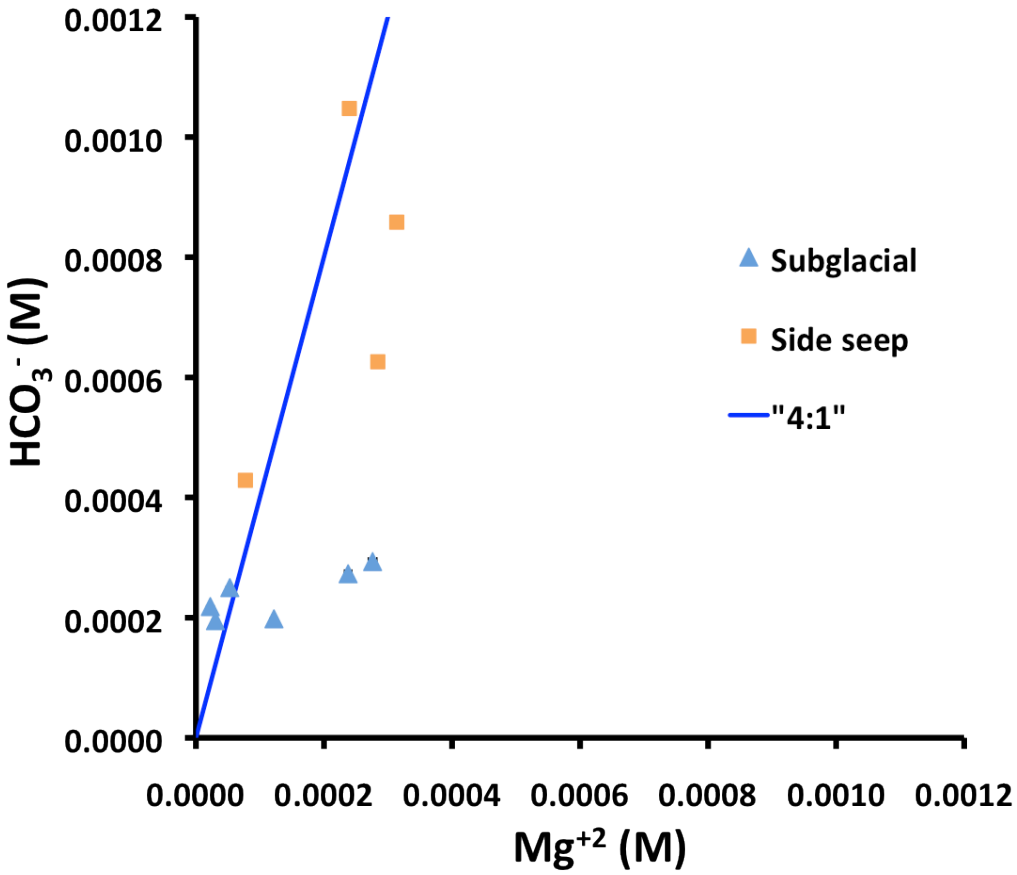

Figure 2.7. Mg^{+2} vs HCO_3^- abundances for subglacial meltwaters and proglacial "side seep" waters at Robertson Glacier. The 4:1 anion:cation ratio line indicates carbonic acid dissolution of dolomite.

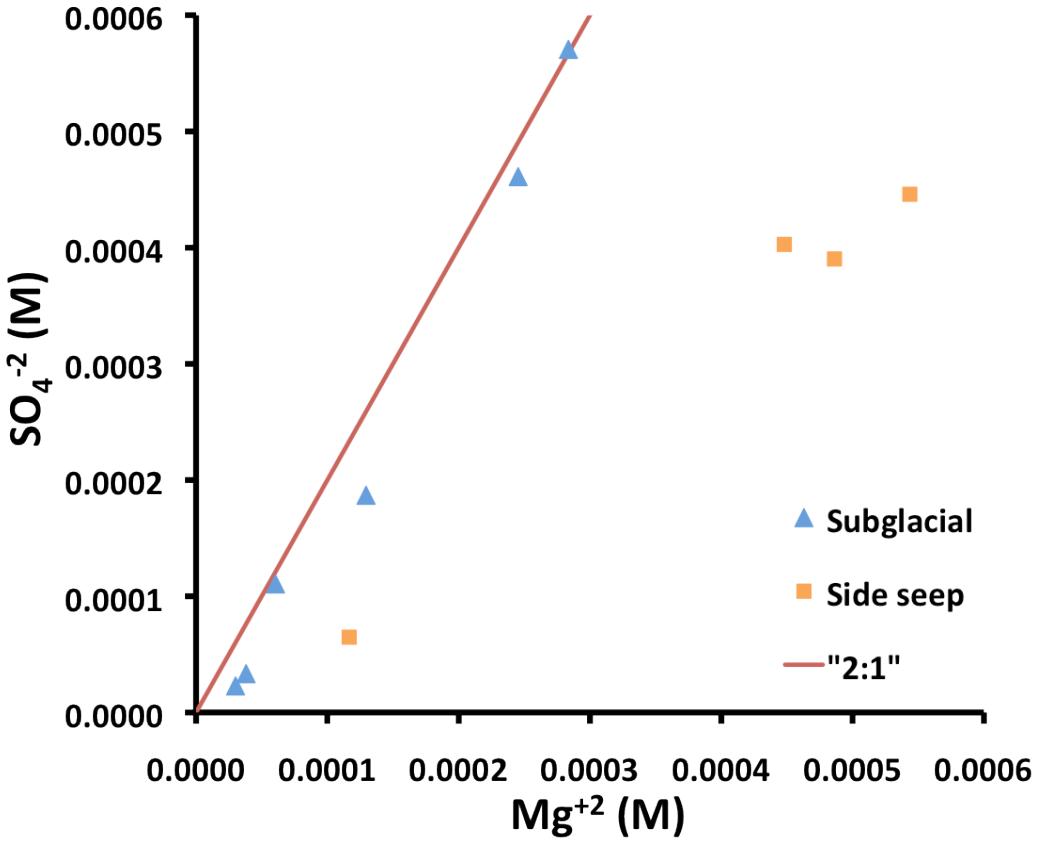

Figure 2.8. Mg^{+2} vs SO_4^{-2} abundances for subglacial meltwaters and proglacial "side seep" waters at Robertson Glacier. The 2:1 anion:cation ratio line indicates sulfuric acid dissolution of dolomite. Departure from that line indicates anther source of Mg^{+2}.

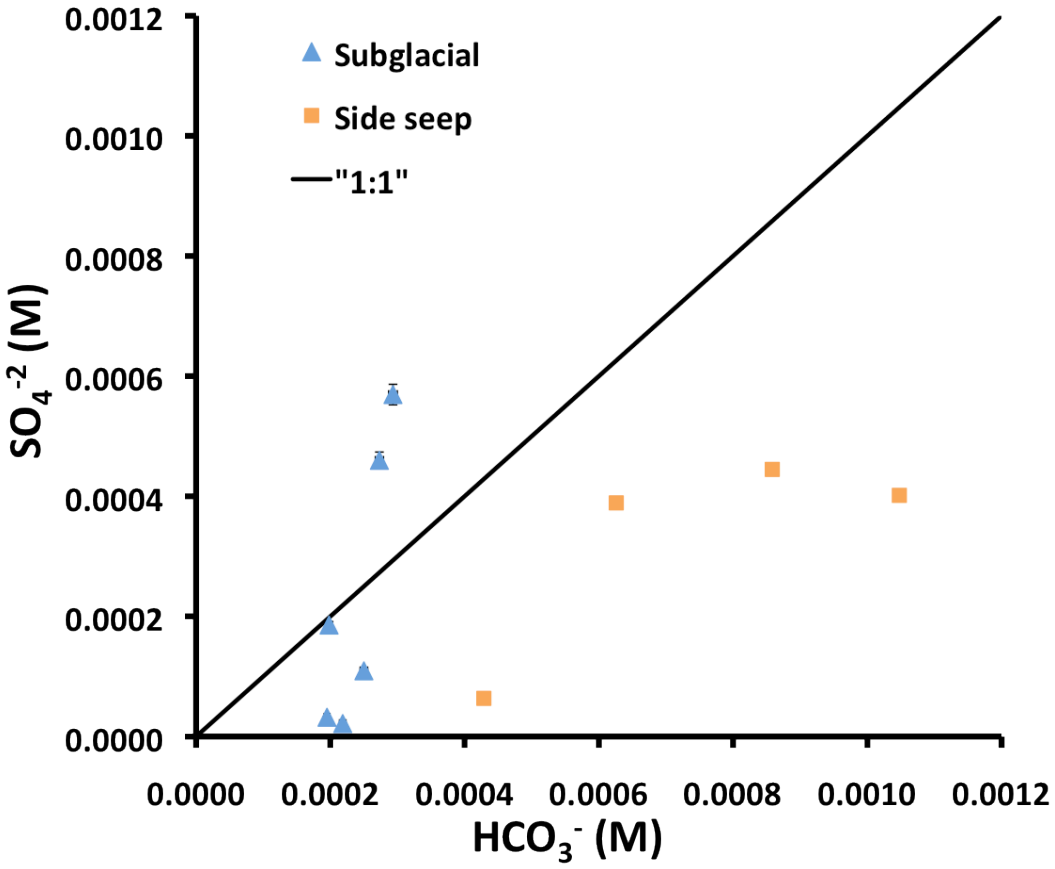

Figure 2.9. HCO_3^- vs SO_4^{-2} abundances for subglacial meltwaters and proglacial "side seep" waters at Robertson Glacier. Abundances of each anion increase with different dissolution processes: HCO_3^- results from carbonic acid dissolution of carbonate minerals, and SO_4^{-2} results from sulfuric acid dissolution of carbonate minerals.

2.3. Results and Discussion

The empirical method defined above resulted in average values for subglacial and proglacial (side seeps) dissolution. The distinct signatures of calcite and dolomite dissolution by two forms of acidic weathering are separated using this method. Tables 2.2

and 2.3 show type examples of the results of the solute tracking method. The subglacial sample shown in Table 2.2 contains solutes due to sulfuric acid dissolution of dolomite and carbonic acid dissolution of calcite, with the greater amount of solutes originating from sulfuric acid dissolution of dolomite. The final row of zero or near-zero values demonstrates that the solute tracking method accounted for nearly all the ions in solution.

The proglacial "side seep" sample shown in Table 2.3 contains solutes due to carbonic dissolution of dolomite, as well as sulfuric acid dissolution of calcite and dolomite. Input from carbonic acid dissolution of calcite was zero in this unique solution of the four defining equations. The greatest amount of solute can be accounted for by carbonic acid dissolution of dolomite, with the next most important process being sulfuric acid dissolution of calcite. The final row of zero or near-zero values demonstrates that the solute tracking method accounted for nearly all the ions in solution.

Table 2.2. Relative Contributions of Subglacial Dissolution Reactions

	Sample 101014A (subglacial)			
	Ca^{+2} (mM)	Mg^{+2} (mM)	HCO_3^- (mM)	SO_4^{-2} (mM)
C+C	0.147	0.000	0.293	0.000
D+C	0.000	0.000	0.000	0.000
D+S	0.276	0.276	0.000	0.552
C+S	0.000	0.000	0.000	0.000
Total calculated	0.423	0.276	0.293	0.552
Actual measurement	0.455	0.276	0.293	0.569
Actual - calc	0.032	0.000	0.000	0.017

C+C= carbonic acid dissolution of calcite; D+C= carbonic acid dissolution of dolomite
D+S= sulfuric acid dissolution of dolomite; C+S= sulfuric acid dissolution of calcite

Table 2.3. Relative Contributions of Proglacial Dissolution Reactions

	Sample 110927G (side seep)			
	Ca^{+2} (mM)	Mg^{+2} (mM)	HCO_3^- (mM)	SO_4^{-2} (mM)
C+C	0.000	0.000	0.000	0.000
D+C	0.107	0.107	0.429	0.000
D+S	0.002	0.002	0.000	0.004
C+S	0.060	0.000	0.000	0.060
Total calculated	0.169	0.109	0.429	0.064
Actual measurement	0.163	0.109	0.429	0.064
Actual - calculated	-0.006	0.000	0.000	0.000

C+C= carbonic acid dissolution of calcite; D+C= carbonic acid dissolution of dolomite
D+S= sulfuric acid dissolution of dolomite; C+S= sulfuric acid dissolution of calcite

Based on the results outlined above, Figure 2.10 shows a schematic diagram of likely weathering paths and the associated dominant weathering processes. It can be seen that the subglacial meltwaters contain cations resulting from 1) the dissolution of dolomite by sulfuric acid, 2) the dissolution of calcite by sulfuric acid, and 3) the dissolution of calcite by carbonic acid. The side seep waters contain cations resulting from 1) the dissolution of dolomite by carbonic acid, 2) the dissolution of calcite by sulfuric acid, and 3) the dissolution of dolomite by sulfuric acid. The side seep waters also show evidence for calcite precipitation, based on the methods described in Figure 2.4.

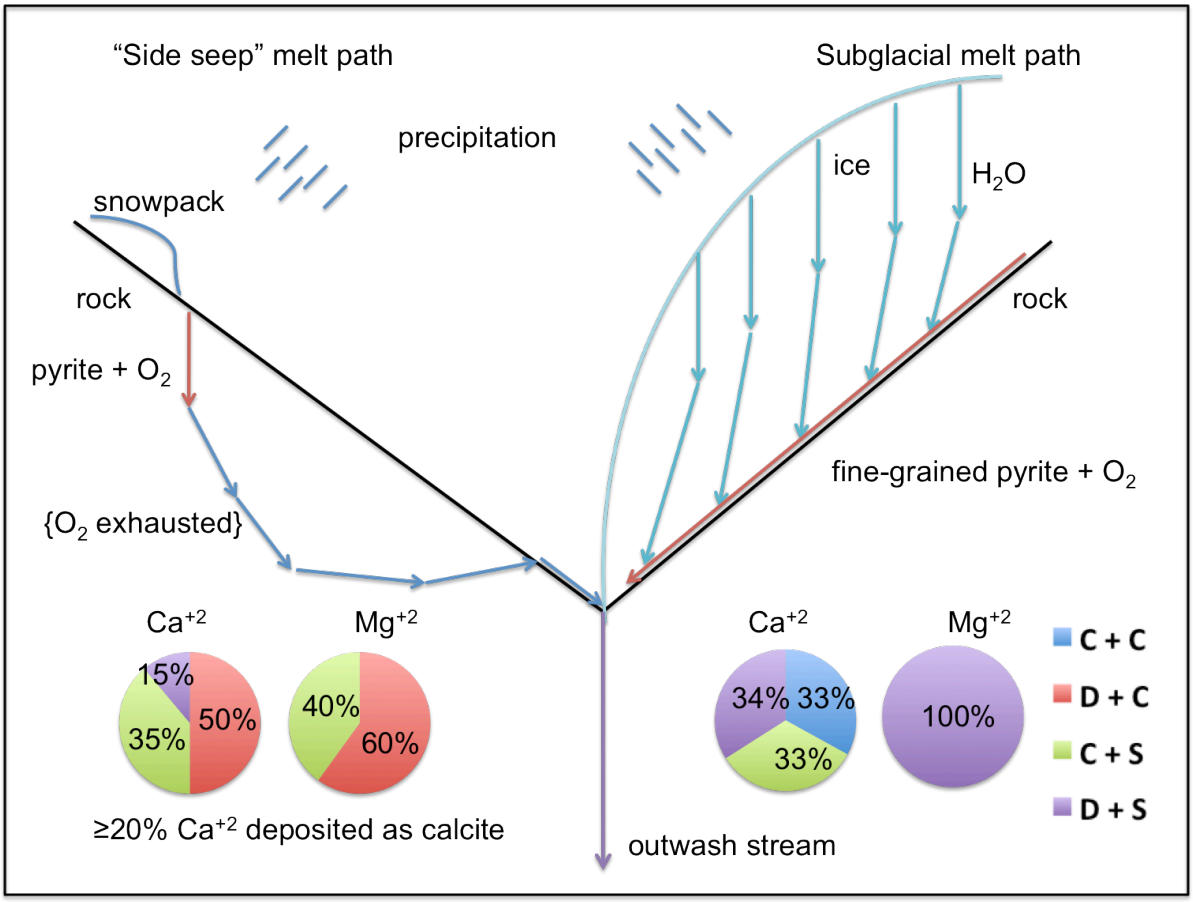

Figure 2.10. A model of subglacial and proglacial (side seeps) weathering processes, with measurements superimposed. The relative amounts of solutes due to weathering processes is shown as such: (1) carbonic acid dissolution of calcite: "C+C", blue; (2) carbonic acid dissolution of dolomite: "D+C", red; (3) sulfuric acid dissolution of calcite: "C+S", green; and (4) sulfuric acid dissolution of dolomite: "D+S", purple. Subglacial weathering is dominated by a "short-duration" flowpath, resulting in sulfuric-acid dissolution dominated weathering system. The side seep systems are dominated by a "longer-duration" flowpath including a greater amount of carbonic acid dissolution of dolomite and the precipitation of calcite.

The subglacial system shows evidence for greater amounts of dolomite and calcite dissolution by sulfuric acid than the proglacial system. As sulfuric acid is formed in nature through oxidation of sulfides [*Sharp et al.*, 1995], these results indicate the probable oxidation of pyrite in the subglacial and proglacial environments (see Chapter 4 for more discussion of observed pyrite oxidation). At Robertson Glacier, this process is most likely enhanced by microbial action [*Sharp et al., 2002*; *Hamilton et al.*, 2013]. A continual supply of oxygen is required in order for this process to occur at the inferred rate. A steady supply of oxygen could be entering the subglacial system through oxygenated supraglacial meltwater (sourced from snow and ice melt and precipitation) draining through the crevasses to the subglacial bed. Additionally, a steady supply of fresh pyrite must be readily available. Fresh surfaces could be supplied through subglacial grinding of bedrock. In the proglacial plain, finely powdered bedrock contains pyrite crystals, but it is not being resupplied in the same manner as the subglacial till. In order for pyrite oxidation and sulfuric acid dissolution to dominate the subglacial weathering system, the resupply of oxygen must be occurring on a steady timescale, as the kinetics of dolomite dissolution make it less reactive than calcite [*Fairchild et al.*, 1994]. There is also input from carbonic weathering of calcite observed in the subglacial meltwaters, indicating that the fluid is in contact with the atmosphere (i.e. contains dissolved carbon dioxide) and able to produce relatively weak carbonic acid. These factors taken together indicate that the subglacial weathering system is the relatively "short-duration" weathering path, dominated by sulfuric acid dissolution of carbonate minerals (Figure 2.5. It is likely that chemolithotrophic microbial populations are

involved in this process [*Hamilton et al.*, 2013], making the subglacial bed a rich ecosystem due to a continual supply of fresh mineral surfaces through glacial grinding and oxygenated water through crevasse-driven resupply.

The proglacial, or "side seep" system measured solutes, however, show evidence for relatively more carbonic acid dissolution from dolomite, indicating a "long-duration" reaction path, as inferred from the kinetics of dolomite [*Fairchild et al*., 1994]. Meltwaters derived from snowmelt and precipitation potentially have longer residence times in the proglacial till than in the subglacial channels. As there is still some input from sulfuric acid dissolution of calcite and dolomite, we infer that this process takes place in the upper soil layers, where the waters are oxygenated. Once the oxygen is used up by pyrite oxidation, carbonic acid dissolution takes over and ultimately dominates the system. Thus, pyrite-oxidizing microbial populations are most likely confined to the upper soil layer, making the proglacial plain a less attractive habitat.

2.4. Conclusions

Herein, the weathering regime of Robertson Glacier is quantified using aqueous geochemical methods. It is demonstrated that, through iterative methods, one can transform cation abundances in solution to quantifiable mineral abundances. This makes it possible to determine the minerals subjected to active weathering, and the dominant weathering reactions. We find that the subglacial system is dominated by carbonate dissolution by sulfuric acid coupled with pyrite oxidation, and the proglacial system is dominated by carbonic acid dissolution of carbonate minerals. These findings imply that the proglacial moraine is an oxygen-limited system with a slower overall weathering rate,

while the regularly replenished glacier bed has a relatively faster overall rate of weathering, contributing to erosion of the alpine valley.

Aqueous geochemistry data show that multiple carbonate dissolution reactions are occurring in different zones of the valley. The subglacial system is dominated by carbonate dissolution due to sulfuric acid, which is formed through microbial pyrite oxidation in subglacial sediments, while the deglaciated till plain is dominated by carbonic acid dissolution due to atmospheric interactions. These findings imply a more active microbial population in the subglacial environment, which is in line with previous studies [*Sharp et al.*, 2002; *Boyd et al.*, 2011; *Hamilton et al.*, 2013]. The subglacial environment appears to be a habitat for chemolithoautotrophic microbes, providing a steady supply of fresh mineral surfaces and oxygenated meltwaters.

These findings have important implications for astrobiology. While Mars is a volcanic planet, covered primarily by mafic rocks such as basalt, past studies have found that even at catchments dominated by noncarbonate crystalline rock such as gneiss and metasedimentary rock, carbonate dissolution contributes more than half – sometimes dramatically more – of the total solute flux [*Sharp et al.*, 1995; *Anderson et al.*, 2000; *Tranter et al*., 2002]. This implies that carbonate dissolution, sometimes coupled with sulfide oxidation, is the dominant weathering process in most subglacial environments [*Anderson*, 2007].

The surface of Mars has long been known to have been mechanically affected by ice processes [*Lucchitta*, 1981] and modern-day debris-covered glaciers made of water ice have been observed [*Holt et al.*, 2008]. When these glaciers flowed under past climate conditions, probably generating liquid water at their bases, carbonate dissolution should

have played a primary role in chemically weathering the basaltic bedrock. Consequently, the conditions under these glaciers – wet, dark, with a steady supply of fresh mineral surfaces – would have made excellent habitats for chemolithotrophic life.

CHAPTER 3

THERMAL INFRARED SPECTROSCOPY OF ROBERTSON GLACIER

3.1. Introduction and Background

Glaciers and ice fields currently cover approximately 10% of the Earth's land surface [*Mitchell et al.*, 2013] and have a significant impact on global biogeochemical cycles, in particular through the chemical weathering of bedrock [*Anderson et al.*, 2000; *Anderson*, 2007]. Glacial chemical weathering produces a wide range of alteration signatures such as dissolution rinds and iron oxides [*Whalley et al.,* 1990; *Raiswell et al.,* 2009; *Rutledge et al.*, 2013] but is not well characterized in great part due to the difficulty of accessing these mountainous and often isolated glaciated regions [*Anderson*, 2007]. Compositional remote sensing is one way of bridging the distance to these inaccessible areas.

Thermal infrared (TIR) spectroscopy is a powerful tool for the compositional analysis of geologic materials. The shape, position, and depth of vibrational absorption features in infrared spectra are diagnostic of a material's mineralogy [*Vincent and Thompson*, 1972]. The spectral signatures of minerals add linearly when mixed, assuming the proportions of minerals match their exposed surface areas [*Ramsey and Christensen*, 1998]. This technique has been applied to determine the mineralogy of rocks in laboratory settings [*Ruff*, 1998; *Hamilton and Christensen*, 2000; *Wyatt et al*. 2001; *Michalski et al.*, 2004, 2006; *Rampe et al.*, 2013] and by remote sensing [*Gillespie*, 1992; *Ramsey et al.*, 1999; *Bandfield et al.*, 2000; *Christensen et al.*, 2000a; *Bandfield et al.*, 2002; *Michalski et al.*, 2004], through linear spectral deconvolution. The spectral

signature from a rock originates in the upper tens of microns of the rock surface, making TIR spectroscopy ideal for examining weathering products such as a leached rind.

Previous studies have shown the utility of remote sensing data in studying rock composition in glacial regions [*Casey*, 2012; *Casey et al.*, 2012]. TIR and near-infrared (NIR) satellite data has been used to characterize soils and minerals over large areas [*Rockwell and Hofstra*, 2008; *Vicente and Filho*, 2011]. *Casey and Kääb* [2012] showed that TIR data can be used in conjunction with visible and near-infrared imagery to estimate percent glacial surface dust and composition of glacial surface debris. The study focused on determining trace elements and mineralogy in volcanic and granitic terrains, however, and does not address the effects of weathering. *Michalski et al.* [2004] demonstrated that the removal of primary minerals in granitic rock surfaces can in fact be detected using TIR remote sensing, making this a valid technique for studying weathering at large scales. In this study, similar techniques are applied to carbonate rock weathering.

In this study, Advanced Spaceborne Thermal Emission and Reflection Radiometer (ASTER) data is used to detect evidence of glacial weathering in the front range of the Canadian Rockies using remotely detected infrared spectra. Orbital observations are ground-truthed using laboratory infrared spectroscopy of field samples. The major goal of this chapter is to link in situ sampling with remote sensing capabilities.

3.1.1 Geology of Robertson Glacier Valley

Robertson Glacier (50˚44'N, 115˚20'W) is one of two northern drainages of the Haig Icefield in Peter Lougheed Provincial Park, Kananaskis Country, Alberta, Canada. The glacier is approximately 2 km long, spans an elevation range from 2370 to 2900 m,

and terminates on a flat till plain with glacially smoothed bedrock surfaces exposed along the glacier margins (Figure 3.1).

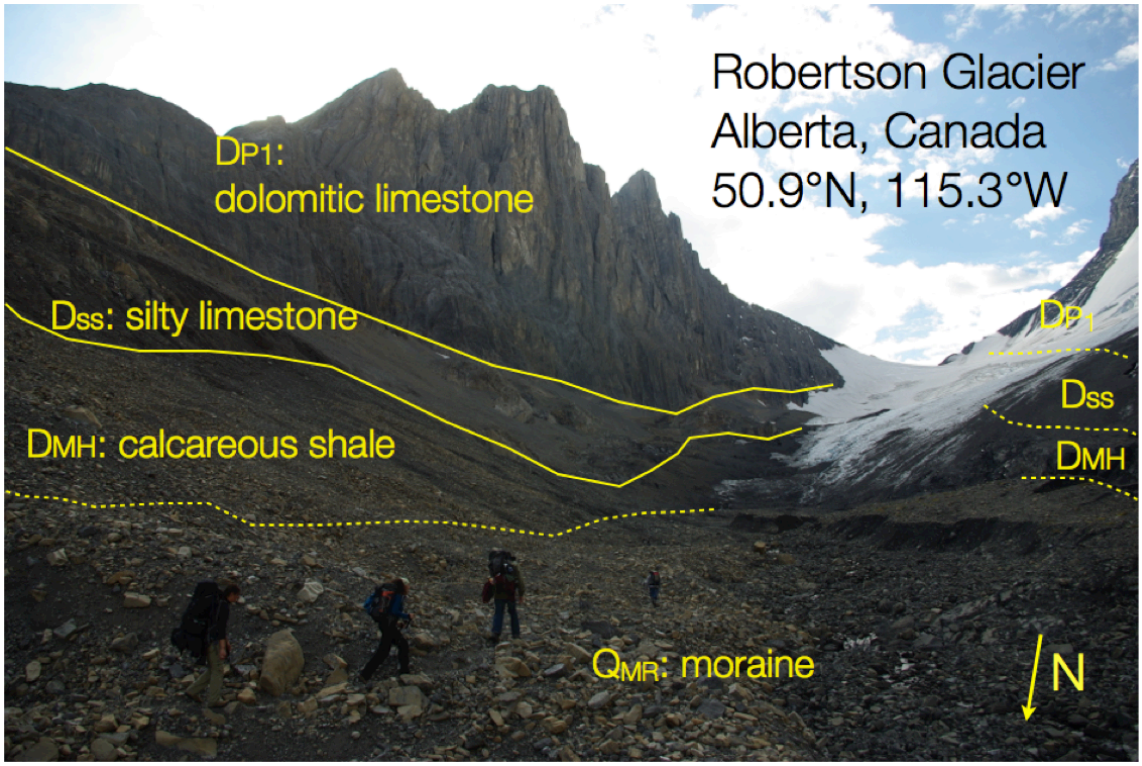

Figure 3.1. View south from Robertson Glacier moraine. Major geologic units and contacts labeled (inferred contacts under ice labeled with dashed lines). D_{MH}: Mount Hawk Formation; D_{SS}: Sassenach Formation; D_{Pl}: Lower unit of the Palliser Formation. Geochemists for scale.

The glacial valley follows a NW-SE trending upright anticline, exposing three Upper Devonian units on both walls: the Mount Hawk Formation (D_{MH}), overlain by the Sassenach Formation (D_{SS}), which is in turn overlain by the lower unit of the Palliser

Formation (D_{P1}) [*McMechan*, 1988]. Glacial action has enlarged and eroded the valley; lateral moraines form the neoglacial moraine deposits (Q_{MR}) identified by *McMechan* [1988]. These units are labeled in Figure 3.1.

The oldest unit, the Mount Hawk Formation, forms the floor of the valley and is composed of calcareous shale and argillaceous limestone. Bedrock surfaces crop out in places through the till plain. The Sassenach Formation, composed of interbedded quartzose siltstone and silty limestone, rests unconformably on the Mount Hawk Formation to form the lower elevation slopes of the valley. The lower unit of the Palliser Formation, which weathers massively to form the highest elevation cliffs, is composed primarily of dolomitic limestone. The geologic setting is further described in Chapter 2.

3.2. Laboratory Spectroscopy of Field Samples

3.2.1 Sample Collection and Preparation

Over the course of two field seasons (October 2010 and September 2011), samples were collected from 24 sites on and around Robertson Glacier (Figure 3.2), including supraglacial samples from the glacier's ablation zone, subglacial samples from melt-back ice caves at the glacier terminus, and proglacial samples from moraine deposits in the downstream valley. At each sample site, several cobbles representing the dominant rock type were selected. An effort was made to avoid sampling talus from recent rock falls, in order to target rocks altered by glacial action. Talus was defined as angular, fresh rocks contained in aprons originating at the valley walls. Exceptions were made in order to gain "fresh" rock from the higher elevation bedrock.

Samples large enough were sawed to expose "fresh" surfaces, and the cobbles' natural surfaces were treated as the "weathered" surfaces. A total of 74 surfaces were prepared, 37 "fresh" and 37 "weathered." A comprehensive list of samples, identifying which cobbles were large enough for the "fresh/weathered" preparation are listed in Appendix B.

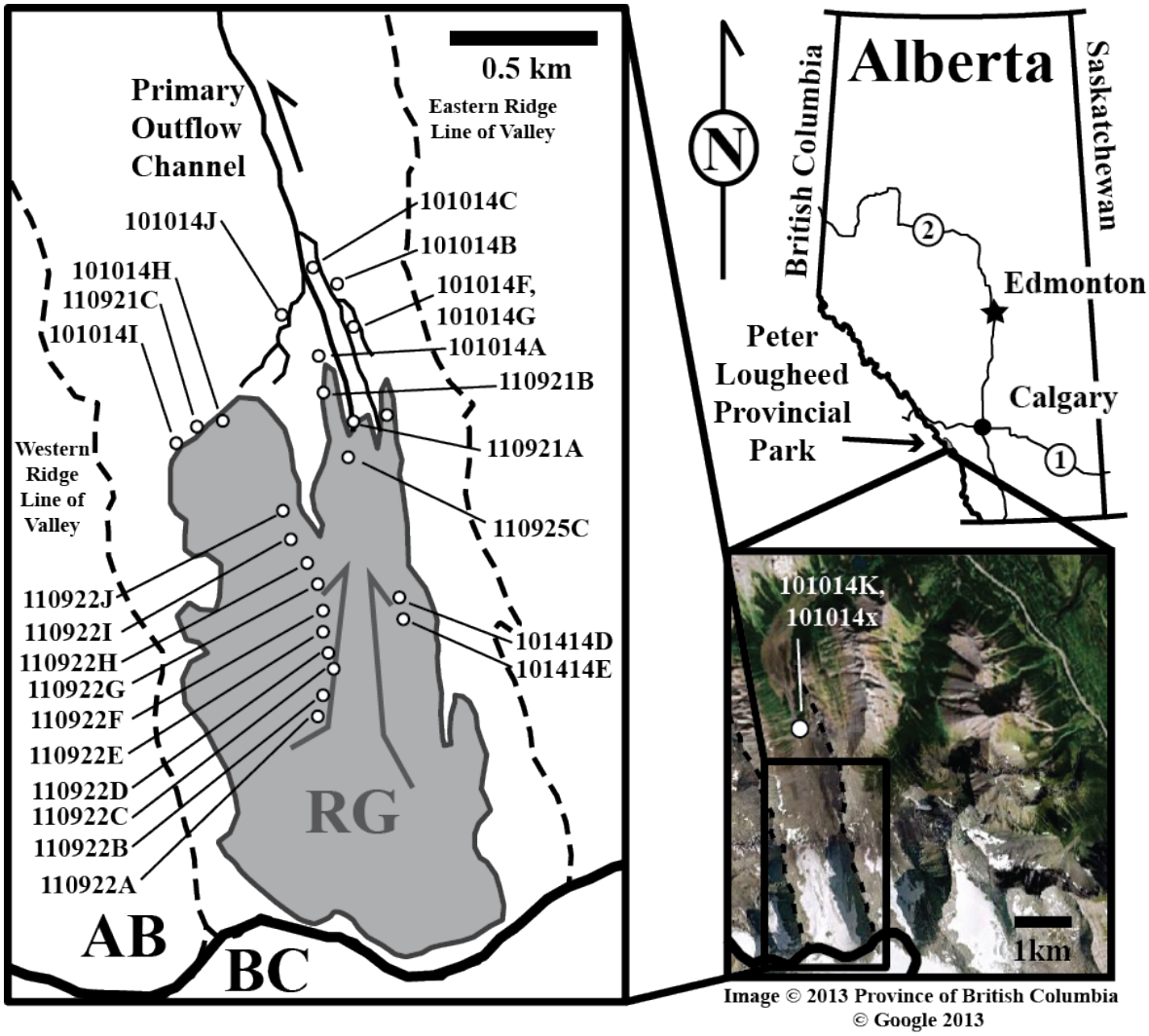

Figure 3.2. Locations of rock sample collection at Robertson Glacier (RG) over 2010 and 2011 field seasons. Gray shaded areas represent extent of present-day ice. Peter Figure

3.2. (cont'd) Lougheed Provincial Park is located at the border of Alberta (AB) and British Columbia (BC), Canada.

3.3.2 Laboratory Spectroscopy Methods

Emission spectra of fresh and weathered sample surfaces were measured at the Arizona State University Mars Space Flight Facility, using a Nicolet Nexus 670 spectrometer with 2 cm^{-1} spectral resolution and ~3 cm field of view. The setup, described in detail in *Ruff et al.* [1997] is configured to directly measure emitted energy, and the sample chamber was purged with N_2 gas to minimize spectral contributions from water vapor and CO_2 during measurement.

Emission spectra were recorded during several sessions following each field season. Samples were heated overnight to 80˚C to increase the signal-to-noise ratio and 180 spectra, collected over the course of ~3 minutes, from 200-2000 cm^{-1} with 2 cm^{-1} spectral resolution, were co-added. Calibrated blackbodies at 70˚C and 100˚C blackbodies were measured periodically in order to calibrate raw data to radiance. Radiance spectra were then converted to emissivity by normalizing to the Planck curve corresponding to the sample temperature [*Ruff et al.*, 1997].

Emissivity spectra of rocks were deconvolved to end-member abundances using a linear deconvolution algorithm described by *Ramsey and Christensen* [1998]. In this method, an input library of known emissivity spectra is used to model the measured spectrum of a sample by weighting the appropriate library end-members as to minimize the error difference between the measured and modeled spectra. A library of 30 emissivity spectra was assembled using the Arizona State University thermal emission

spectral library [*Christensen et al*., 2000b] and several other sources (Table 3.1). End-members were chosen based on *a priori* knowledge of the field site's primary lithologies (e.g. *McMechan* [1998]; *Sharp et al.* [2002]) and possible weathering products present (amorphous components, sulfates, iron oxides).

Table 3.1. TIR Spectral Library

Mineral group	Spectral end-member	Composition and source
Silicates	Silica 589-dark 20070323	SiO_3[a]
	Opal-A	$SiO_2 \cdot n(H_2O)$[b]
	Quartz	SiO_2[b]
Feldspars	Albite WAR-0612	$NaAlSi_3O_8$[c]
	Labradorite WAR-4524	$Ab_{50}An_{50}$-$Ab_{30}An_{70}$[c]
	Microcline BUR-3460	$KAlSi_3O_8$[c]
Amorphous	Allophane 044	Si:Al 0.44[d]
	Allophane 092	Si:Al 0.92[d]
	Aluminosilicate gel ALLO560	Si:Al 5.6[d]
Clay minerals	Halloysite ECL:HAL001	$Al_2Si_2O_5(OH)_4$[e]
	Hectorite	$Na_{0.3}(Mg,Li)_3Si_4O_{10}(OH)_2$[e]
	Illite Imt-1 <0.2 microns	$(K_{1.35},Na_{0.02})Al_{3.41}[Si_{7.26}(Fe_{0.67},Mg_{0.55})O_{20}](OH)_4$[c]
	Illite/Smectite ECL:ILS103	$K_{1\text{-}1.5}Al_4(Si_{7\text{-}6.5}Al_{1\text{-}1.5}O_{20})(OH)_4$[e]
	Kaolinite Kga-1b	$Al_4Si_4O_{10}(OH)_8$[c]
	Montmorillonite Swy-2	$Na_{0.33}(Al_{1.67}Mg_{0.33})Si_4O_{10}(OH)_2$[c]
	Montmorillonite ECL:MON106	$(½Ca,Na)_{0.7}(Al,Mg,Fe)_4((Si,Al)_8O_{20})(OH)_4 \cdot nH2O)$[e]
	Nontronite ECL:NON104	$Na_{0.3}Fe_2^{3+}(Si,Al)_4O_{10}(OH)_2 \cdot nH_2O$[e]
	Saponite Eb-1 <0.2 microns	$(Li_{0.09}Mg_{2.72}Fe^{3+}_{0.03}Al_{0.07})(Al_{0.04}Si_{3.96})O_{10}(OH)_2$[d]
Sulfates	Anhydrite S16	$CaSO_4$[f]
	Bassanite S11	$CaSO_4 \cdot 1/2H_2O$[f]
	Gypsum S8	$CaSO_4 \cdot 2H_2O$[f]
Carbonates	Calcite C9	$CaCO_3$[c]
	Calcite C8	$CaCO_3$[c]
	Calcite C27	$CaCO_3$[c]
	Dolomite C20	$CaMg(CO_3)_2$[c]
	Dolomite C19	$CaMg(CO_3)_2$[c]
	Magnesite C55	$MgCO_3$[c]
Oxides	Goethite GTS2	FeOOH[g]
	Goethite GTS4	FeOOH[g]
	Hematite BUR-2600	Fe_2O_3[c]

[a] *McDowell and Hamilton* [2009], [b] *Michalski et al.* [2003], [c] *Christensen et al.* [2000b], [d] *Rampe et al.* [2012], [e] *Cloutis et al.* [2007], [f] *Lane et al.* [2006], [g] *Glotch et al.* [2004]

The deconvolution model also included a blackbody component to account for spectral contrast differences between the library and measured spectra, and phase abundances were normalized after excluding the blackbody end-member, as it contains no mineralogical information [*Hamilton et al.*, 1997]. The error associated with linear deconvolution has been empirically determined to be 0-15% for rock-forming minerals [*Feely and Christensen*, 1999]. In addition, a common error that occurs with this method is the inclusion of inaccurate minerals at the 1-5% level, due to mathematical modeling of noise or other non-compositional information contained in emissivity spectra [*Ramsey and Christensen*, 1998].

3.3 Results from Laboratory Spectroscopy

In general, emissivity spectra of weathered surfaces exhibit shallower absorption features than those of fresh surfaces (Figure 3.3). Weathered carbonate absorptions tend to narrow, while silicate (quartz) absorption features tend to broaden compared to fresh spectra. Spectra of weathered surfaces have shallower band depths than fresh surfaces, probably due to scattering on fresh natural surfaces that reduces the spectral contrast due to the presence of small cavities that act as blackbody cavities. Some of the spectral contrast reduction could also be due to particle size effects, as natural surfaces have rock flour clinging to them in some cases.

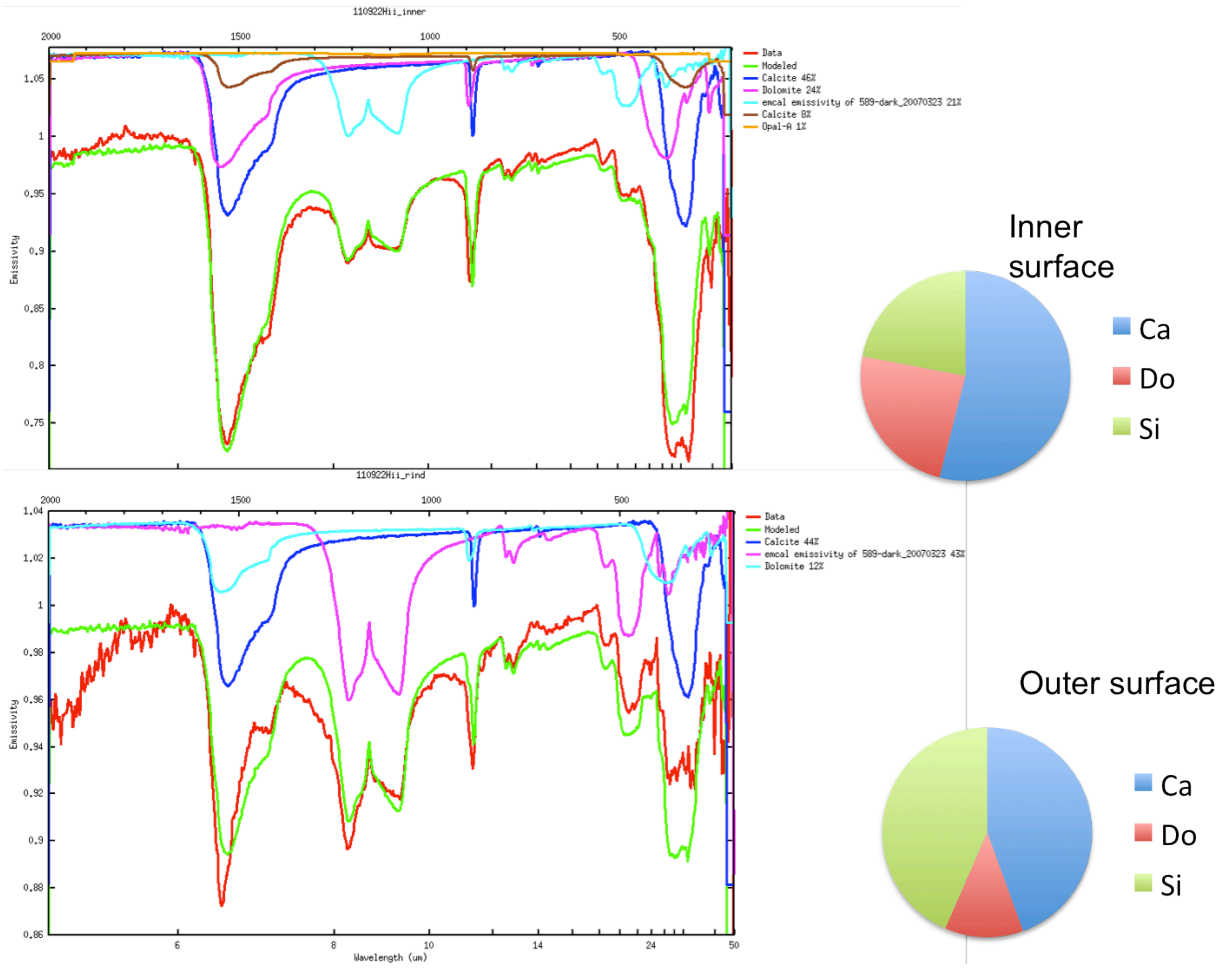

Figure 3.3. Example of measured (red) and modeled (green) spectra for inner "fresh" rock surfaces and outer "weathered" rock surfaces. Spectral end-members used in each model are shown in other colors. The outer surface contains a relatively greater proportion of silicate with respect to carbonate.

Each fresh and weathered sample was measured for amounts of carbonate and silicate minerals, as illustrated in Figure 3.3, and total carbonate abundances for each fresh/weathered sample pair evaluated. Carbonate abundances for inner (fresh) and outer (weathered) surfaces are plotted in Figure 3.4. The 1:1 line in the figure represents an unweathered surface (i.e. the inner "fresh" surface has the same carbonate abundance as the outer "weathered" surface). The majority of samples (subglacial, supraglacial, and proglacial) fall below or on the 1:1 line within error bars. Points below the line indicate samples with a depleted outer surface with respect to carbonates, and points on or near the line indicate samples with little carbonate removal. The general trend indicates a removal of carbonate minerals from the outermost surface, implying the presence of dissolution rinds on a majority of rock samples.

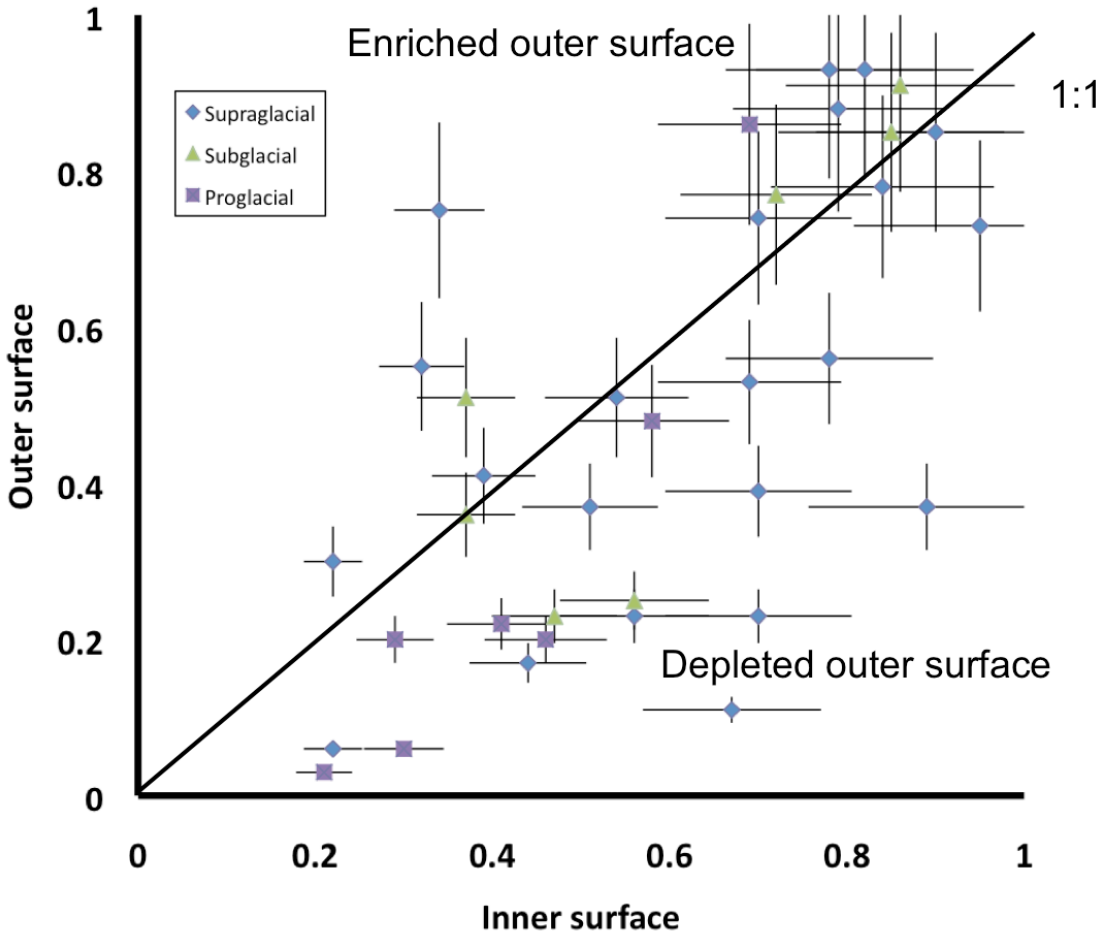

Figure 3.4. Relative carbonate abundances of inner "fresh" rock surfaces and outer, "weathered" rock surfaces, including bars representing a maximum 15% possible error due to spectral deconvolution. The majority of samples - subglacial, supraglacial, and proglacial - fall below the 1:1 line, indicating a depleted outer surface with respect to carbonates.

The samples that plot above the 1:1 line in Figure 3.4 can be interpreted as relatively enriched surfaces with respect to carbonates. Two scenarios could explain this potential enrichment: local deposition of carbonate minerals onto rock surfaces, or "checkerboard" mixing of the host rock with small calcite veins at laboratory spectroscopy scales (~3 cm). Checkerboard mixing at these scales can result in an artificially elevated carbonate measurement, as the spectrometer used in this study cannot resolve individual, compositionally distinct features <3 cm in size. Chapter 4, microscopic investigations of these weathered surfaces, reveals the presence of small calcite veins cross-cutting the surfaces of several samples. The outliers in Figure 3.4 that plot far above the 1:1 line are most likely due to the presence of these veins.

3.4. Orbital Spectroscopy of ASTER Data

Infrared imagery of the region was collected with the Advanced Spaceborne Thermal Emission and Reflection Radiometer (ASTER) satellite instrument aboard the NASA Earth Observing System satellite Terra. The ASTER instrument has 14 bands between 0.52-11.65 mm at 15-90 m/pixel resolution [*Kahle et al.* 1991; *Yamaguchi et al.*, 1998]. ASTER's TIR emissivity data was used to remotely characterize the alteration mineralogy at the field sites. These bands, which have a ground spatial resolution of 90 m, are described in Table 3.2.

Table 3.2 Measured Spectral Performance of ASTER TIR Bands

ASTER Band	Central wavelength (μm)	Band width (μm)
10	8.291	0.344
11	8.634	0.347
12	9.075	0.361
13	10.657	0.667
14	11.318	0.593

Data from ASTER User's Guide (Earth Remote Sensing Data Analysis Center, 2005)

Carbonate and silicate minerals are especially well characterized by strong vibrational absorption features within the 8-14 μm window measured by the five TIR bands of the ASTER sensor [*Hook et al.*, 1999]. Reference spectra of carbonate and quartz minerals including diagnostic spectral absorptions are shown in Figure 3.5, at laboratory and ASTER resolutions. In Figure 3.5a, the emissivity absorption features of quartz at ASTER bands 10 and 12 are due to fundamental asymmetric Si-O stretching vibrations [*Salisbury and D'Aria*, 1992]. In Figure 3.5b, the emissivity absorption features of calcite and dolomite as ASTER band 14 are related to out-of-plane bending modes of the CO_3 ion [*Clark*, 1999]. Dolomite exhibits a greater decrease in emissivity than calcite between bands 13 and 14, due to the greater width and shorter wavelength position of the bending feature of dolomite 11.15 μm relative to the bending feature of calcite at 11.27 μm [*Rockwell and Hofstra*, 2008]. However, this difference is only apparent when comparing dolomite and calcite exposures of great enough areal extent, due to the ASTER TIR spatial resolution of 90 m per pixel. ASTER bands 14, 12, and 10 are useful in characterizing the silicate and carbonate minerals present at Robertson Glacier.

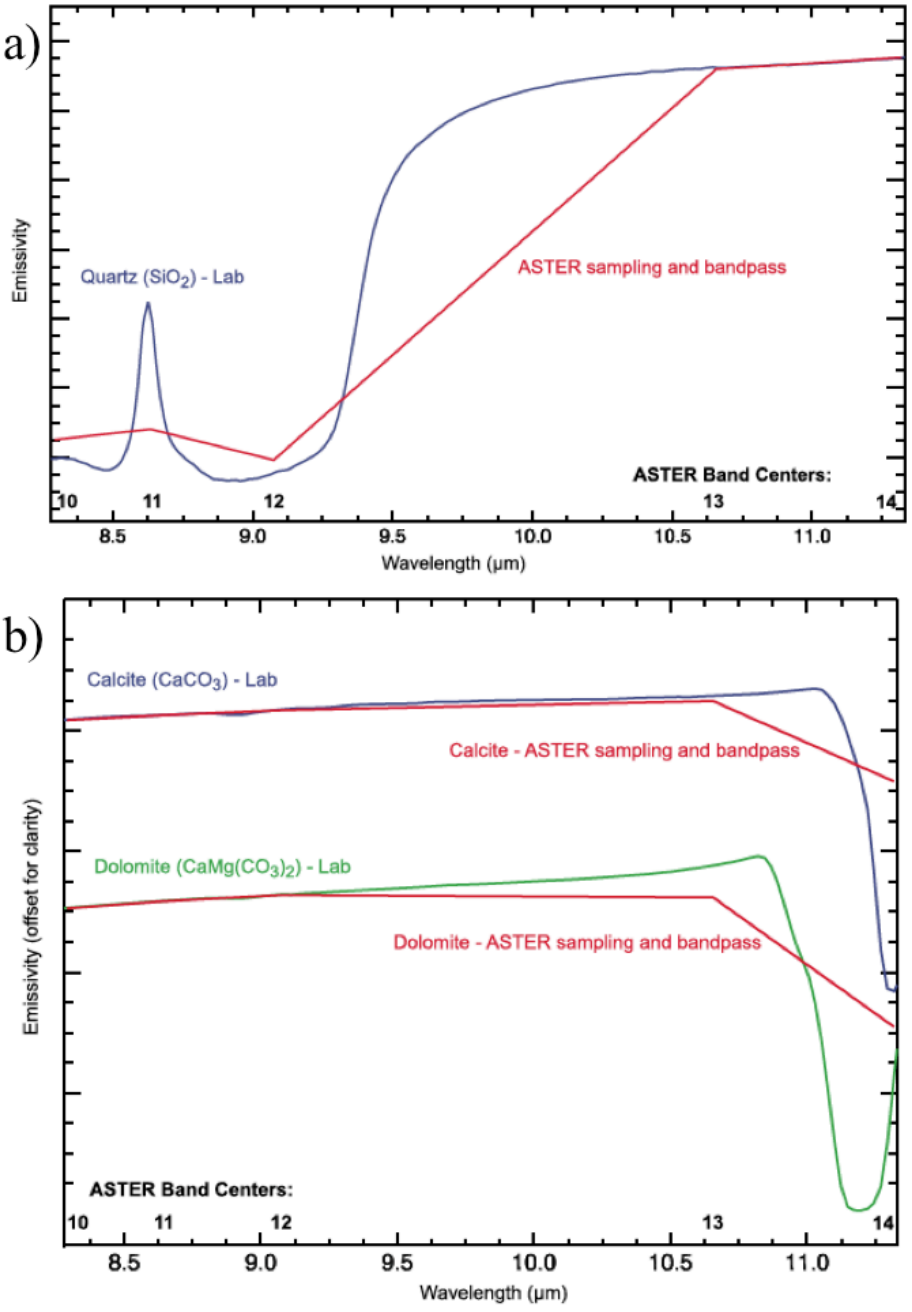

Figure 3.5. Sample laboratory spectra of a) quartz, and b) calcite and dolomite. Spectra convolved to ASTER resolution shown in red. After *Rockwell and Hofstra* [2008].

3.4.1 ASTER investigation of Robertson Glacier

ASTER Level 2 surface emissivity data products (AST_05) from the Land Processes Distributed Active Archive Center (LP DAAC) of the United States Geological Survey (USGS) are produced from Level 1B data (calibrated radiance) using a MODTRAN-based atmospheric correction and a temperature-emissivity separation algorithm developed by *Gillespie et al.* [1998]. Level 1B data are processed from Level 1A format (uncorrected radiance at sensor) by the Earth Remote Sensing Data Analysis Center of Japan. A relatively-cloud free ASTER scene was acquired in August 2010 from the LP DAAC. This time frame was chosen to avoid excessive snow cover. Unfortunately, the tradeoff for minimizing snow cover meant that alpine vegetation was more abundant at the end of summer, effectively masking the composition of northern portions of Robertson Glacier's moraine.

In order to highlight the compositional differences between rock units, a decorrelation stretch of the ASTER scene was performed using DaVinci (davinci.asu.edu), an open-source software package developed at Arizona State University. A decorrelation stretch, (DCS) is a three-band image stretch, based on principal-component analysis, designed to maximize variation within a scene [*Gillespie et al.*, 1986]. In this case it is used to maximize compositional variation and map those relative differences to colors. DCS have been used before to map compositional variation on terrestrial [*Cooper et al.*, 2012] and planetary surfaces [*Edwards et al.*, 2008; *Edwards et al.*, 2011]. ASTER Bands 14, 12, and 10 were selected for mapping Robertson Glacier and the surrounding region as they exhibit distinctive absorption features for silicate and carbonate minerals (Figure 3.5).

Figure 3.6 shows the DCS image, oversampled from 90 m to 15m spatial resolution and draped over ASTER visible-near-infrared band 2 (0.66 μm) in order to better visualize topography and highlight different rock units. Based on field observations and the geological map of the region [*McMechan*, 1988], blues and greens are inferred to represent relatively carbonate-rich rock, while pink and purple tones are inferred to represent relatively silicate rich rock units. Large expanses of snow and ice are marked by hatches, and vegetation is dark gray.

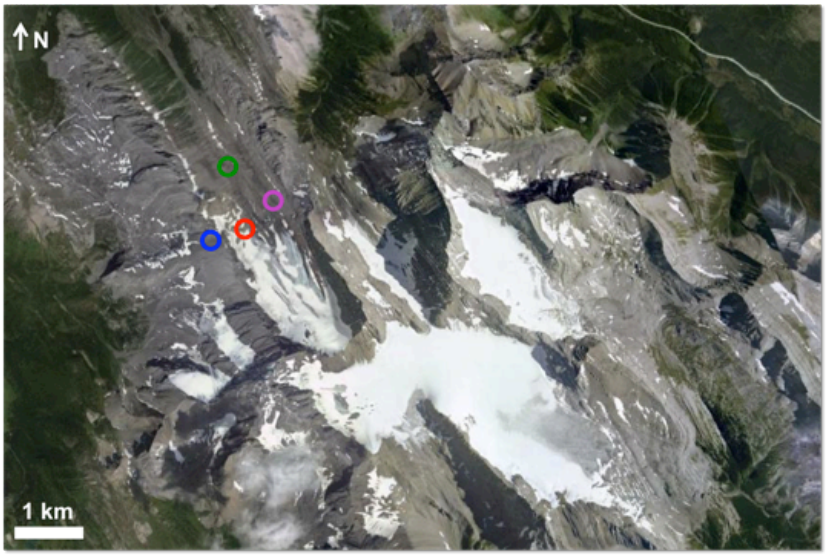
N
1 km

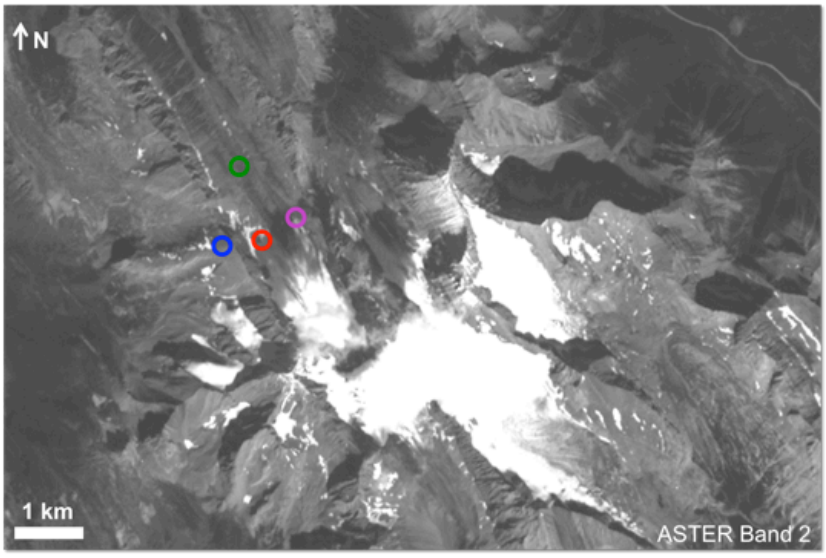
N
1 km
ASTER Band 2

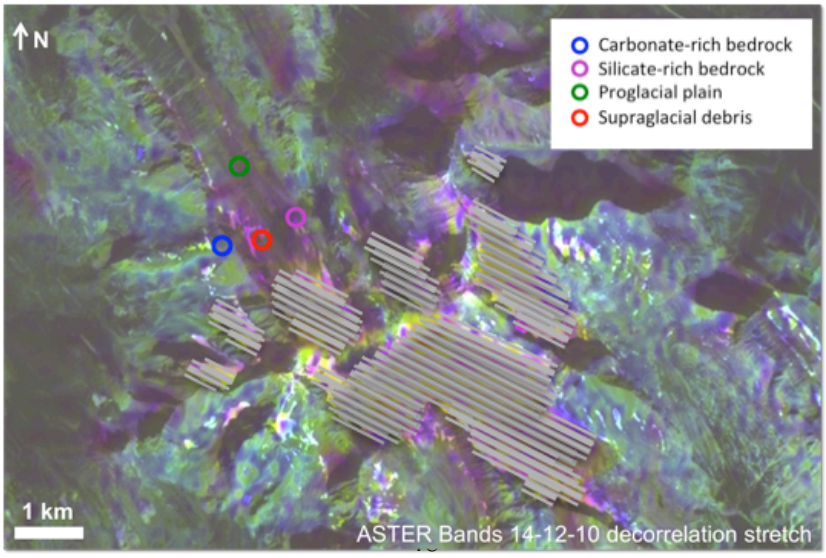
N
Carbonate-rich bedrock
Silicate-rich bedrock
Proglacial plain
Supraglacial debris
1 km
ASTER Bands 14-12-10 decorrelation stretch

Figure 3.6. Google Earth overview, ASTER Band 2, and ASTER decorrelation stretch (Bands 14-12-10) of Robertson Glacier valley. Within the DCS image, blue and green Figure 3.6 (continued). colors indicate relatively carbonate-rich rock, while pink colors are indicative of relatively silicate-rich rock. Ice and snow are masked out for clarity, and dark gray indicates vegetation. Spectral regions of interest are indicated with colored circles.

Five-point TIR spectra were extracted from the regions of interest (see Figure 3.6 for locations) and examined for evidence of carbonate dissolution as seen in laboratory spectra. Figure 3.7 illustrates the orbital spectra used to investigate Robertson Glacier for evidence of weathering by dissolution. It can be seen that the supraglacial debris exhibits a deeper silicate absorption feature than any of the surrounding rock units. This is inferred to be evidence for carbonate leaching from the surface of this rock debris.

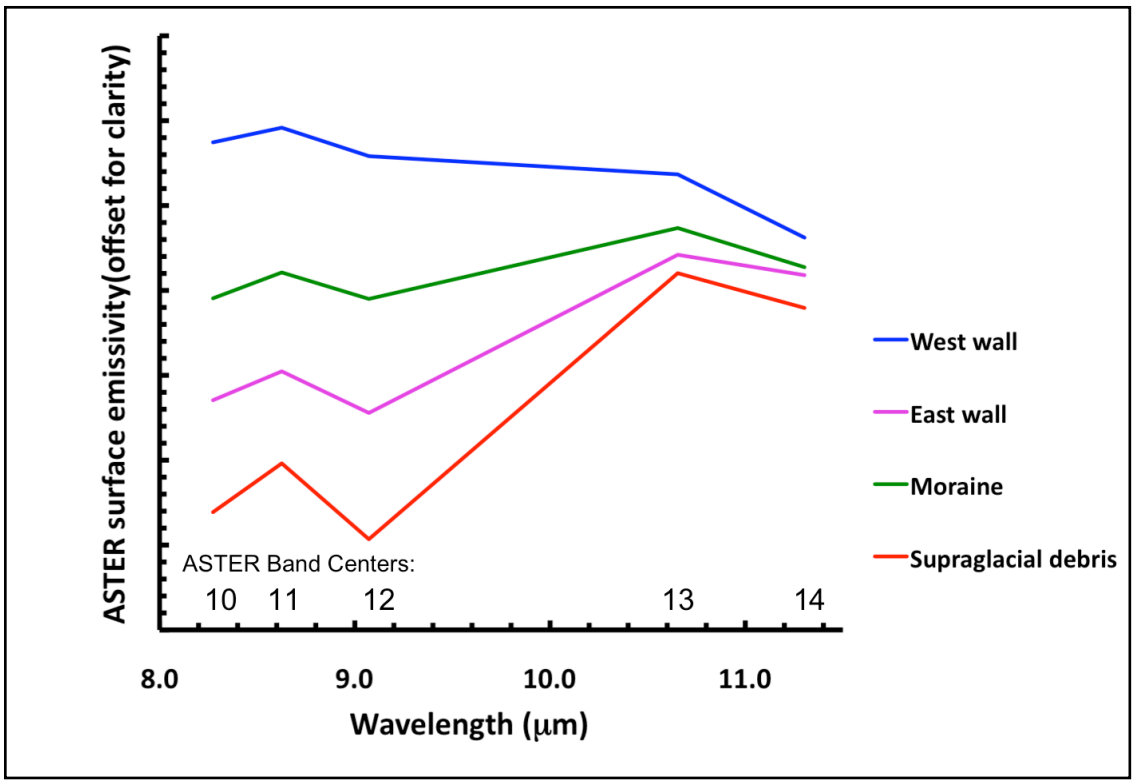

Figure 3.7. ASTER spectra of regions of interest at Robertson Glacier. Locations of sampled pixels are shown in Figure 3.6. Spectra vary from carbonate-rich (west wall) to silicate-rich (east wall). The supraglacial debris shows an even deeper silicate absorption than the east wall, yet still contains a carbonate absorption feature, and the moraine pixels exhibit a shallow silicate absorption feature as well as a carbonate absorption feature.

3.4.2 Examination of Nearby Glacial Valleys

The methods developed at Robertson Glacier valley were applied to surrounding glaciated valleys: French Glacier, a NW-facing, narrow, steep-walled valley parallel to Robertson Valley, and the broad, wide valley of Haig Glacier, which drains to the SE (Figure 3.8). Spectra from French Glacier show that the moraine is made up of leached carbonate-silicate rocks, following the same trend as Robertson Glacier. When comparing sidewall spectral signatures to that of the French Glacier moraine, deeper carbonate absorption is seen in the moraine spectrum. This implies a similar carbonate dissolution process to that of Robertson Glacier is taking place in and around French Glacier. However, moraine spectra from the main Haig Glacier outwash plain compared to the source headwalls do not show deepening carbonate absorptions and thus no obvious signals of carbonate dissolution.

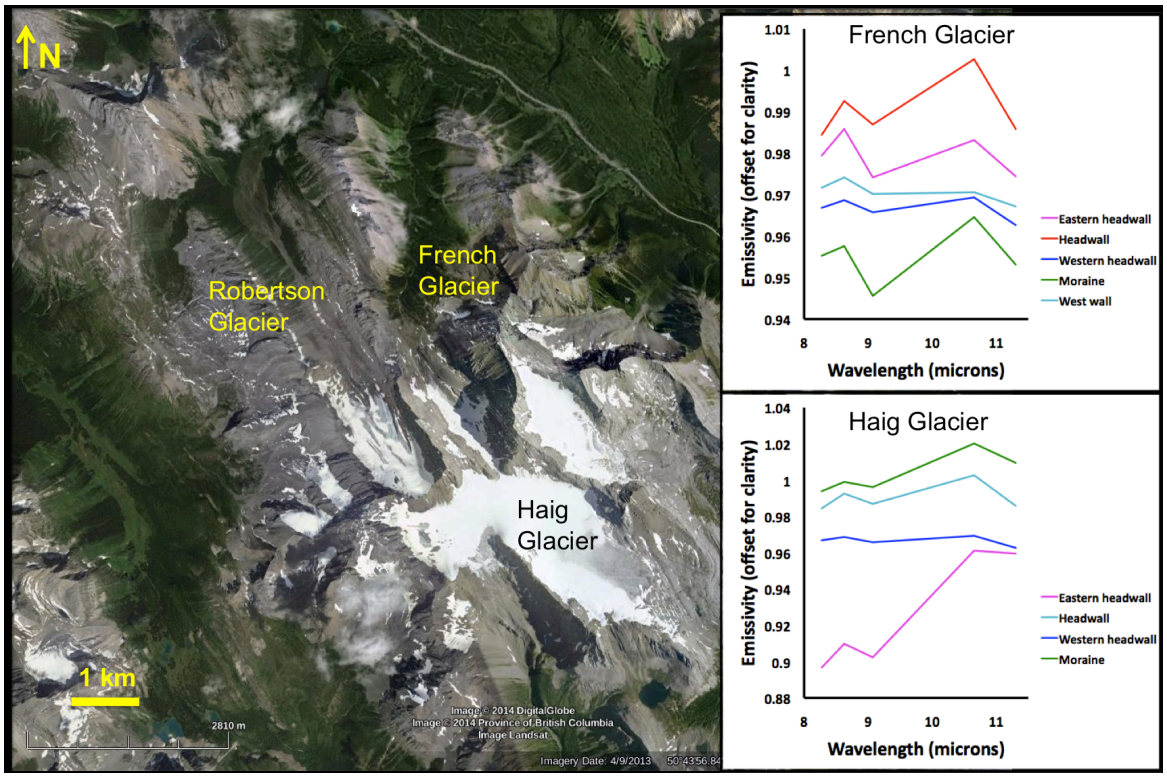

Figure 3.8. Spectral comparison of regions of interest in French Glacier, another NW glaciated valley, and the Haig Glacier drainage, a SE-facing valley. The base imagery is from Google Earth, 2013.

3.5. Discussion and Conclusions

Laboratory spectra results indicate the presence of weathering rinds formed through the dissolution of carbonates. A general trend of decreasing carbonate abundances from the inner to the outer surfaces of rocks is consistent with the alteration regime indicated by the aqueous geochemistry of the glacial environment (Chapter 2). A similar spectral signature indicating a dissolution-weathered rock deposit is observed at 90 m scales in Robertson and French Glacier valleys, while no such trend is observed at SE-facing Haig Glacier.

The lack of a dissolution signature at Haig Glacier could be the result of: (1) a different weathering regime than that of the NW-facing valleys in which carbonate dissolution is not the dominant process; (2) lower rates of carbonate dissolution, perhaps due to a lack of subglacial, pyrite-oxidizing microbial communities; (3) higher rates of weathered material removal, *i.e.* greater ice and snow melt due to insolation and higher associated transportation rate of bedload, or some combination of these. *Wasiuta et al.* [2015] found that atmospheric conditions differed greatly between the opposing Robertson and Haig Valleys, suggesting that their orientation relative to the physiography of the Western Canadian Cordillera exerts the greatest control over differing weather patterns. This suggests that hypothesis (3) is the most likely scenario.

CHAPTER 4

MICROSCOPIC INVESTIGATIONS OF WEATHERING RINDS

4.1. Introduction and background

4.1.1 Formation of Rock Rinds in Cold Regions

Geochemical processes occurring in glacial regions are not well understood, though the importance of chemical weathering at low temperatures has begun to be recognized in recent decades [*Fairchild et al.*, 1999b; *Anderson et al.*, 2000; *Dixon et al.*, 2002]. While traditional models of weathering in cold regions assume that physical processes (*e.g.* frost) are dominant [*Tricart*, 1969; *Washburn*, 1979], more recent studies have led to a new framework in which chemical and biological processes play an important role [*Darmody et al.*, 2000; *Etienne*, 2002; *Thorn et al.,* 2007]. *Dixon and Thorn* [2005] found that chemical weathering in periglacial terrains to be the same as elsewhere, only with generally slower rates. However, except for a few key studies [*Dixon et al.*, 2002; *Etienne*, 2002; *Dixon et al.*, 2006] the formation of weathering rinds on rocks in glacial regions has not been studied. *Dixon et al.* [2002] performed an in-depth study of weathering rinds forming in metamorphic rocks, but the topic of carbonate-clastic weathering rinds is still understudied.

Colman and Pierce [1981] defined weathering rinds as zones of oxidation whose inner boundaries are approximately parallel to the rock surface. *Dixon et al.* [2002] defined weathering rinds as zones of alteration on the outer surfaces of rock debris in which the original rock fabric has been modified and/or where the mineral constituents of the original material have undergone chemical alteration. On the other hand, rock

coatings are defined as chemical accretions on a rock surface whose components have been largely derived externally instead of from the underlying rock. However, under favorable conditions they may be derived from their host rock through chemical weathering [*Dorn*, 1998]. Coatings generally exhibit abrupt boundaries with the host rock, though this is not always true in the case of underlying rock with strong cleavage [*Dixon et al.*, 2002].

Weathering rind formation mechanisms are not well understood, though several studies have shed light on rind formation in granite and schist [*Hodgkins et al.*, 1997; *Thorn et al.*, 2001; *Dixon et al.*, 2002]. *Etienne* [2002] demonstrated the role of biology in rind formation on basaltic terrain in periglacial environments. *Dixon et al.* [2002] showed that geochemically complex rock rinds and coatings form concurrently in plagioclase feldspar-rich rock in a subaerial Arctic environment due to low temperature processes.

Previous detailed studies of low temperature weathering rind formation have primarily focused on the development of weathering rinds on granite, while the faster-weathering carbonates have been largely overlooked. This is most likely due to the fact that carbonate weathering occurs through dissolution, and rarely involves deposition on the same surface. The dissolution of carbonates results in diagnostic rock textures such as microcavities, and can result in silicate minerals armoring a rock surface as the carbonate minerals are removed into solution. This paper describes weathering rinds and/or coatings in carbonate-clastic rocks in a glaciated valley.

4.1.2 Geology of Robertson Glacier Valley

Robertson Glacier (50˚44'N, 115˚20'W) is one of two northern drainages of the Haig Icefield in Peter Lougheed Provincial Park, Kananaskis Country, Alberta, Canada. The glacier is approximately 2 km long, spans an elevation range from 2370 to 2900 m, and terminates on a flat till plain with glacially smoothed bedrock surfaces exposed along the glacier margins (Figure 4.1).

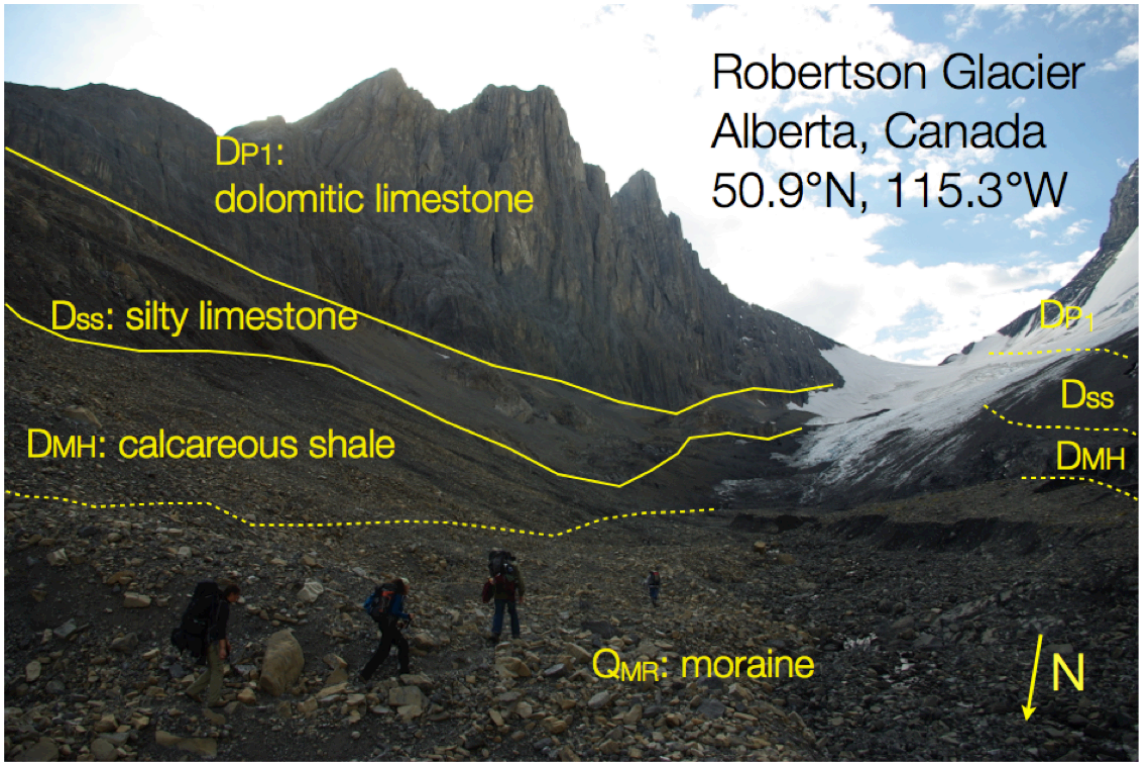

Figure 4.1. View south from Robertson Glacier moraine. Major geologic units and contacts labeled (inferred contacts under ice labeled with dashed lines). D_{MH}: Mount Hawk Formation; D_{SS}: Sassenach Formation; D_{Pl}: Lower unit of the Palliser Formation. Q_{MR}: Neoglacial moraine. Geochemists for scale.

The glacial valley follows a NW-SE trending upright anticline, exposing three Upper Devonian units on both walls: the Mount Hawk Formation (D_{MH}), overlain by the Sassenach Formation (D_{SS}), which is in turn overlain by the lower unit of the Palliser Formation (D_{P1}) [*McMechan*, 1988]. Figure 4.1 shows these rock units. The oldest unit, the Mount Hawk Formation, forms the floor of the valley and is composed of calcareous shale and argillaceous limestone. The Sassenach Formation, composed of interbedded quartzose siltstone and silty limestone, rests unconformably on the Mount Hawk Formation to form the lower elevation slopes of the valley. The lower unit of the Palliser Formation, which weathers massively to form the highest elevation cliffs, is composed primarily of dolomitic limestone. The geologic setting is further described in Chapter 2.

Figure 4.2 shows the location of Robertson Glacier in Alberta, Canada. Aqueous geochemical and thermal infrared spectroscopy studies (Chapters 2 and 3) provide evidence for dissolution of carbonate rocks at Robertson Glacier, potentially forming weathering rinds (Figure 3.4). However, several samples from Chapter 3 appeared to exhibit surfaces enriched with carbonate relative to silicate (Figure 3.4), possibly indicative of rock coatings. This study uses microscopic techniques to interrogate the surfaces of representative samples in order to determine whether weathering rinds, rock coatings, or both, are present.

4.2. Methods

4.2.1 Sample Collection and Preparation

As part of an overarching study investigating the chemical weathering regime and habitability of Robertson Glacier, samples were collected over the course of two field seasons (October 2010 and September 2011) from four sites on and around Robertson Glacier (Figure 4.2), including subglacial samples from melt-back ice caves at the glacier terminus and proglacial samples from moraine deposits in the downstream valley. At each sample site, several cobbles representing the dominant rock type were selected.

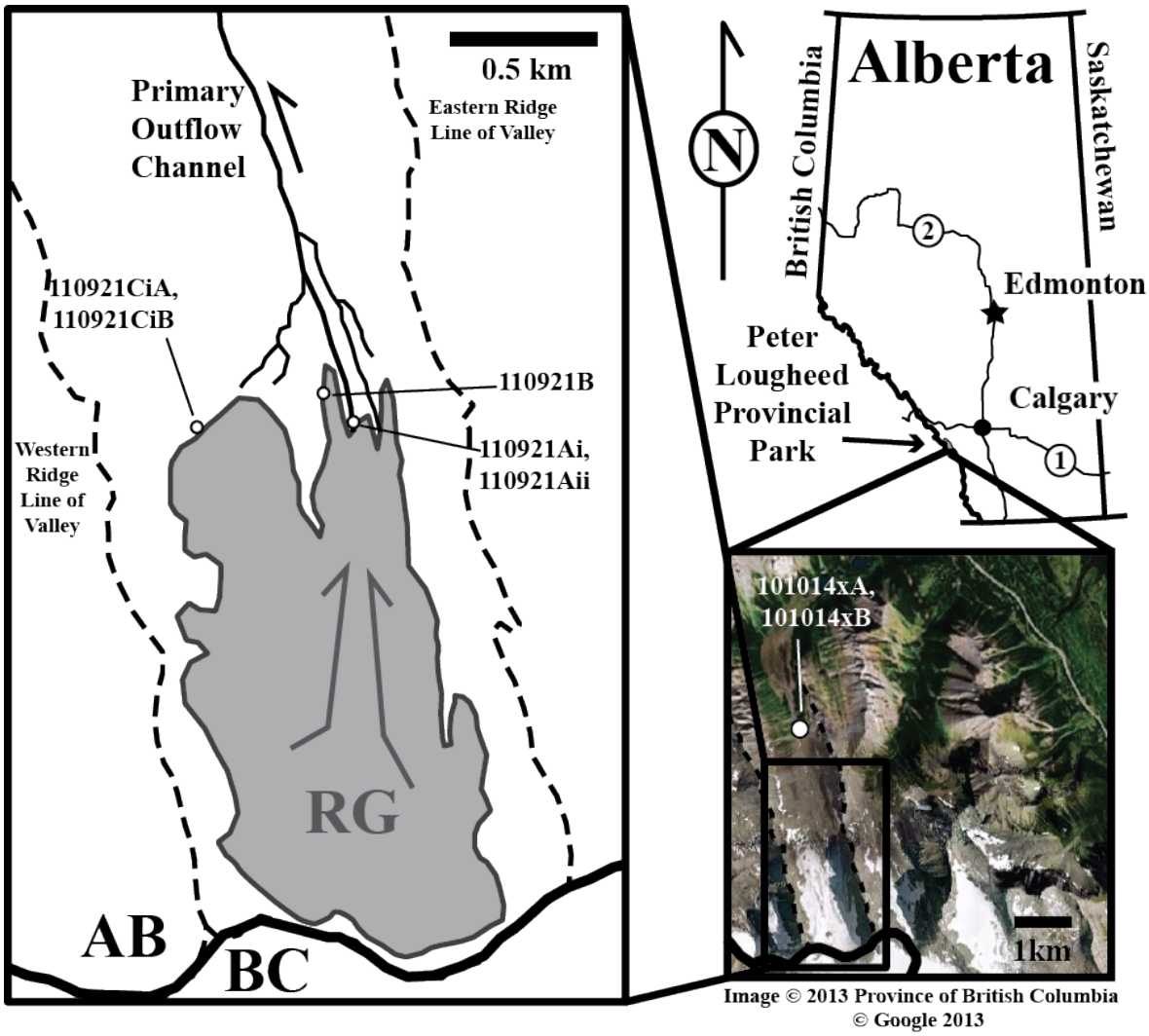

Figure 4.2. Location of samples collected for microscopic analysis at Robertson Glacier, Canada. Location of Robertson Glacier in Peter Lougheed Provincial Park, Alberta, Canada.

Polished thin-sections of seven representative samples, several of each formation (see Appendix B) were prepared by Petrographic Services (Montrose, CO, USA). Rock tablets (approximately 27 x 46 mm) were cut from the exterior surface inwards, to

facilitate examination of the weathered rind. These tablets were impregnated with epoxy (EpoTek 301, Epoxy Technologies, Billercia, MA) to preserve the weathered surfaces. These sections were mounted on glass slides with epoxy (FH-5313A, Andover Corporation, CT) before subsequent grinding, and were then hand-finished to a thickness of 30 ± 2 μm. The samples were examined under reflected and transmitted light in order to identify features of interest along the weathered edges (Figure 4.3). Before loading into the electron microprobe, the samples were carbon-coated in order to eliminate surface charging, which interferes with imaging and analysis.

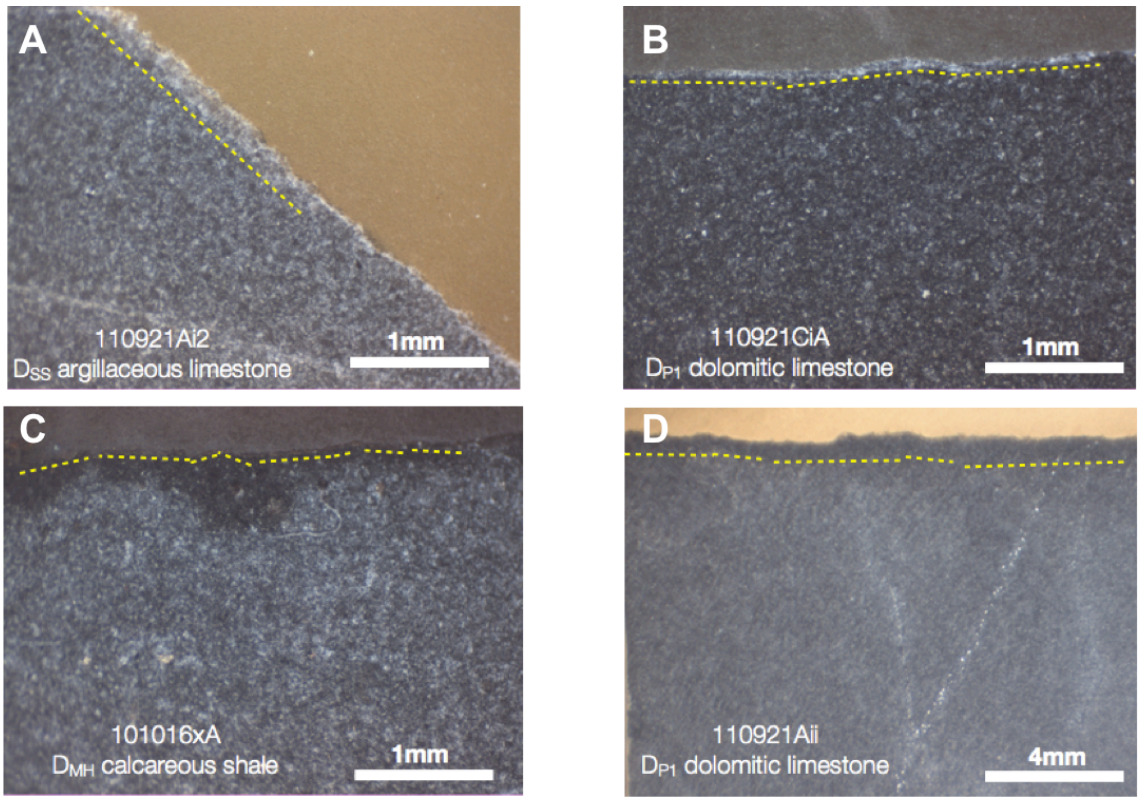

Figure 4.3. Examples of potential thin, discontinuous rinds/coatings observed under reflected light. (A) Subglacial Sassenach Fm sample exhibiting a light-toned surface with an apparently abrupt contact with the underlying rock; this is inferred to be a relict calcite vein. (B) Supraglacial Palliser Fm sample exhibiting a light-toned surface with an abrupt contact with the underlying rock; inferred to be a relict calcite vein. (C) Proglacial Mount Hawk Fm sample exhibiting a darker surface with an apparently gradational contact with the underlying rock; this is inferred to be a dissolution rind. (D) Subglacial Palliser Fm sample exhibiting a darker surface with an apparently gradational contact with the underlying rock, inferred to be a dissolution rind. Note the light-toned veins (inferred to be calcite) cutting through (A) and (D).

4.2.2 Electron Microprobe Analysis

The electron microprobe (the JEOL JXA-8530F Hyperprobe) at the LeRoy Eyring Center for Solid State Science (LE-CSSS), Arizona State University was used to characterize these weathered surfaces at microscopic scales. The microprobe's scanning electron microscope (SEM) uses a focused beam of electrons to scan the surface of the thin section and register an image of various signals. The probe was operated at 15-20 keV and 10-30 nA.

This study utilized backscattered electrons (BSE), secondary electron imaging (SEI), and energy-dispersive X-ray spectroscopy (EDS) [*e.g. Goldstein et al.*, 1981; *Reimer*, 1985]. BSE images show variations in chemical composition based on average atomic number. Materials with lower average atomic numbers appear dark, while materials with higher average atomic numbers appear bright [*Ball and McCartney*, 1981]. SEI images are useful for investigating surface topography and morphology of samples constituents. EDS was used to make chemical maps of sample edges ranging in magnification from 40X to 2,500X. EDS was also used to collect compositional information in transects from the outer weathered edge of each sample inward. In order to measure chemical depletion/enrichment of weathered surfaces, EDS measurements were averaged over 10 μm x 100 μm areas, profiling approximately 1000 μm into each sample rind. Figures 4.9 and 4.10 show examples of one transect.

4.3. Results

4.3.1. Micromorphology

Weathering rinds developed on rock surfaces in the Robertson Glacier catchment display both directly measureable chemical alteration and morphological evidence for chemical weathering. While EDS element maps do not show obvious chemical weathering trends at the millimeter scale (Figure 4.4), closer examination reveals morphological weathering textures. Porous textures at multiple scales are observed in the weathering rinds. Large voids (probable dissolution pockets) are present in samples (*e.g.* Figures 4.5 and 4.6), indicative of rock porosity allowing fluid circulation to a minimum depth of 450 μm. These voids are inferred (due to observed locations) to have initially formed along mineral grain boundaries, and to have increased in volume through dissolution. Figure 4.6 demonstrates the initial stage of dissolution, wherein local fluids exploit preexisting planes of weakness, causing dissolution and resulting in widened fractures parallel to the rock surface.

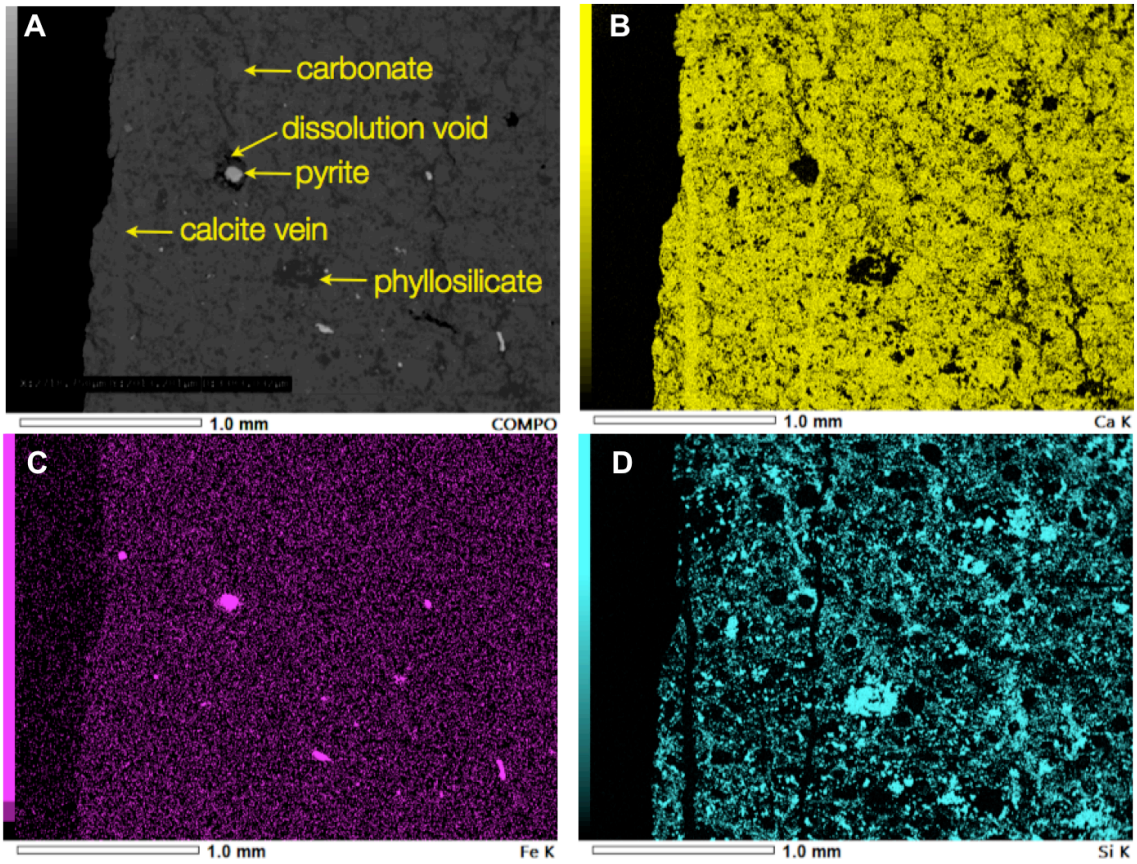

Figure 4.4. Proglacial Mount Hawk Fm sample. (A) Backscattered electron image (40X magnification), location outline in (A); (B) EDS chemical map of Fe; (C) EDS chemical map of Si; and (D) EDS chemical map of Ca. A ~0.1 mm diameter calcite vein can be seen paralleling the weathered surface. At this scale no obvious chemical trends are observed, but potential dissolution-induced voids surrounding the Fe-bearing crystals can be seen.

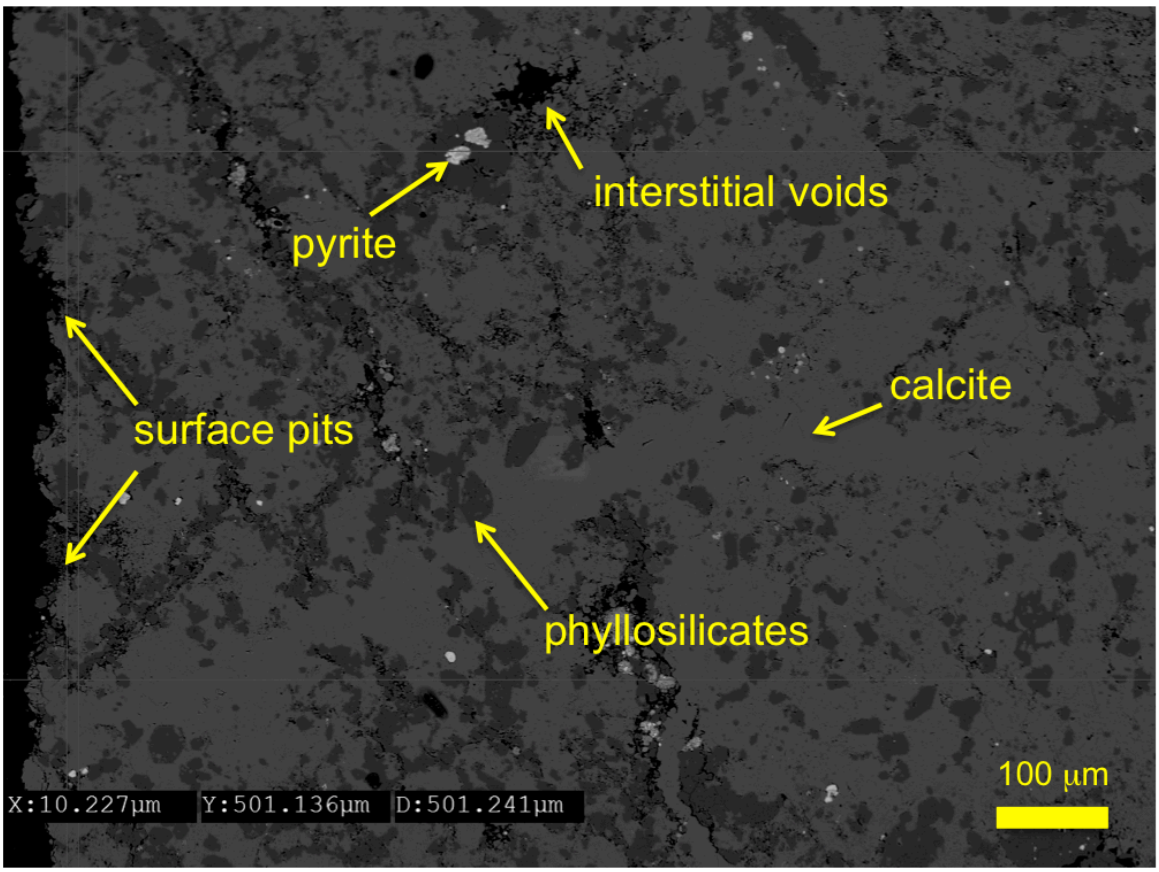

Figure 4.5. Backscattered electron image of proglacial Mount Hawk Fm (magnification 110X), sample 101016xB. This sample is a second thin section prepared from the same cobble as 101016xA, and represents the same groundmass and weathered surface. Pyrite crystals (bright shades), calcite crystals (light gray) and silicate minerals (dark gray) are visible. The rock has been weathered by chemical dissolution to form interstitial voids and surface pitting.

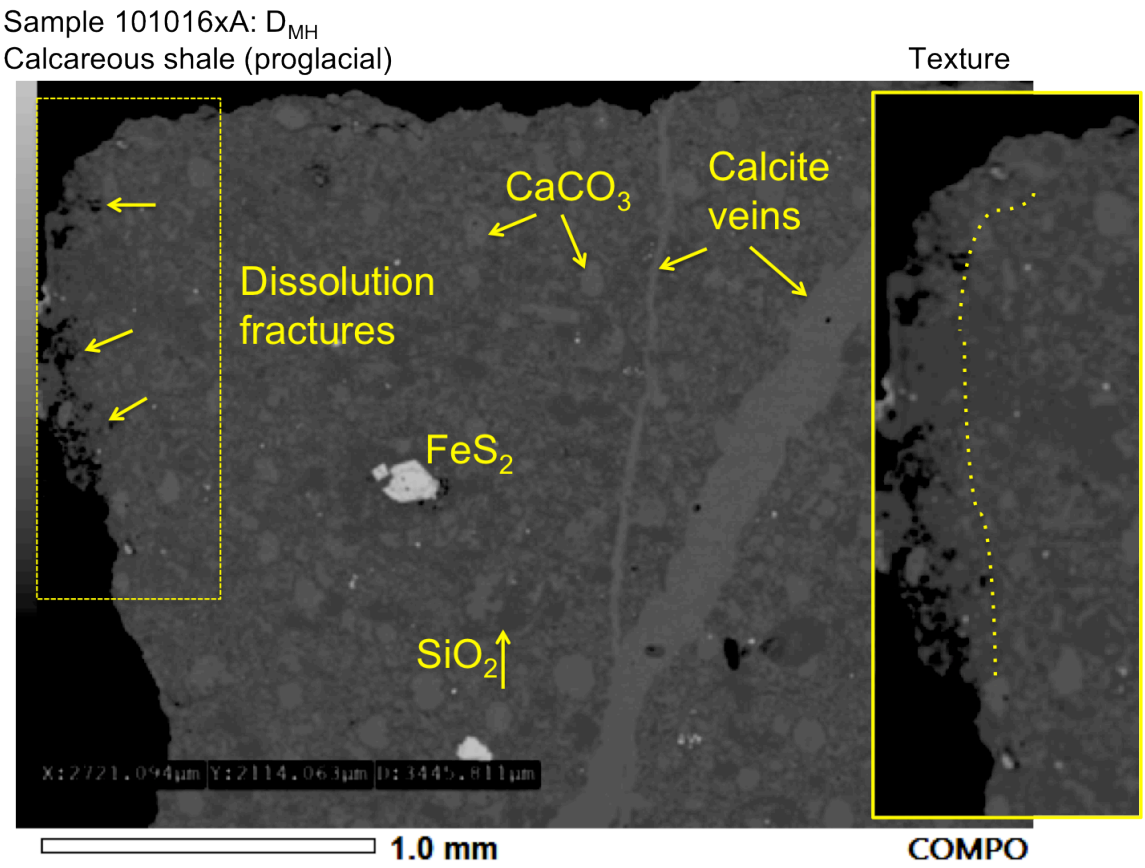

Figure 4.6. Backscattered electron (BSE) image of proglacial Mount Hawk Fm sample exhibiting dissolution features and/or fractures at the surface, as well as calcite veins of varying thicknesses. This type of near-surface fracturing has often been attributed to frost action, but here is interpreted to be the result of exploitation by fluids of existing fractures in close proximity to fluids.

While some samples appear to be coated with calcite (i.e. carbonate-enriched surfaces, *e.g.* Chapter 3), these surfaces are ruled out as rock coatings because no depositional layering is observed (Figures 4.7 and 4.8). Rather, crystal boundaries are

seen within these potential surface coatings. The “coating” is thus inferred to be a relict calcite vein, exposed to the rock surface through fracture and subsequently subjected to carbonate dissolution, rather than a secondary rock coating formed through deposition. Cross-cutting calcite veins are observed in most rock samples (Figures 4.3 and 4.6), giving an additional line of evidence for this hypothesis.

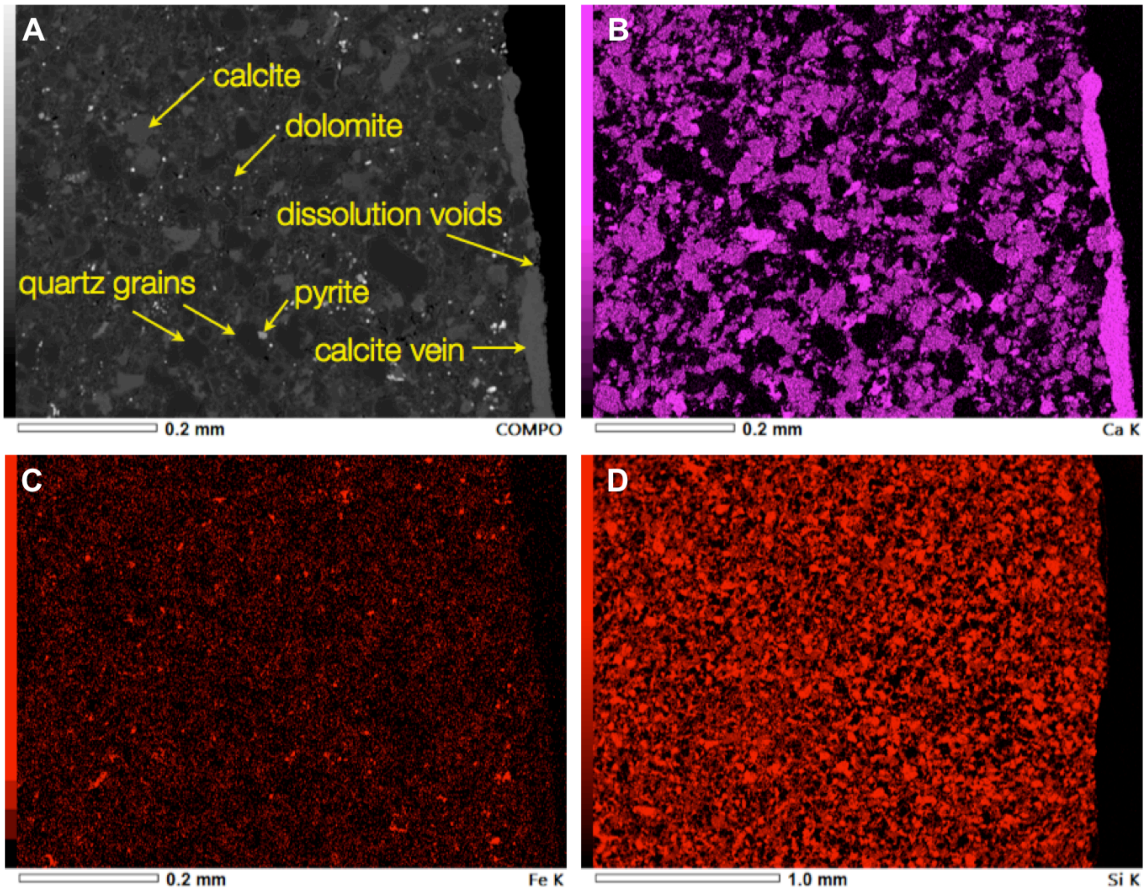

Figure 4.7. Microscopic images of supraglacial Palliser Fm sample with a candidate rock coating are shown in (A) a backscattered electron image (100X magnification); (B) an EDS chemical map of Fe; (C) an EDS chemical map of Si; and (D) an EDS chemical map of Ca. Large dark areas are Al-K phyllosilicates (unmapped in this figure). No immediate chemical trend is evident at this scale, but a discontinuous calcite rind is observed at the surface.

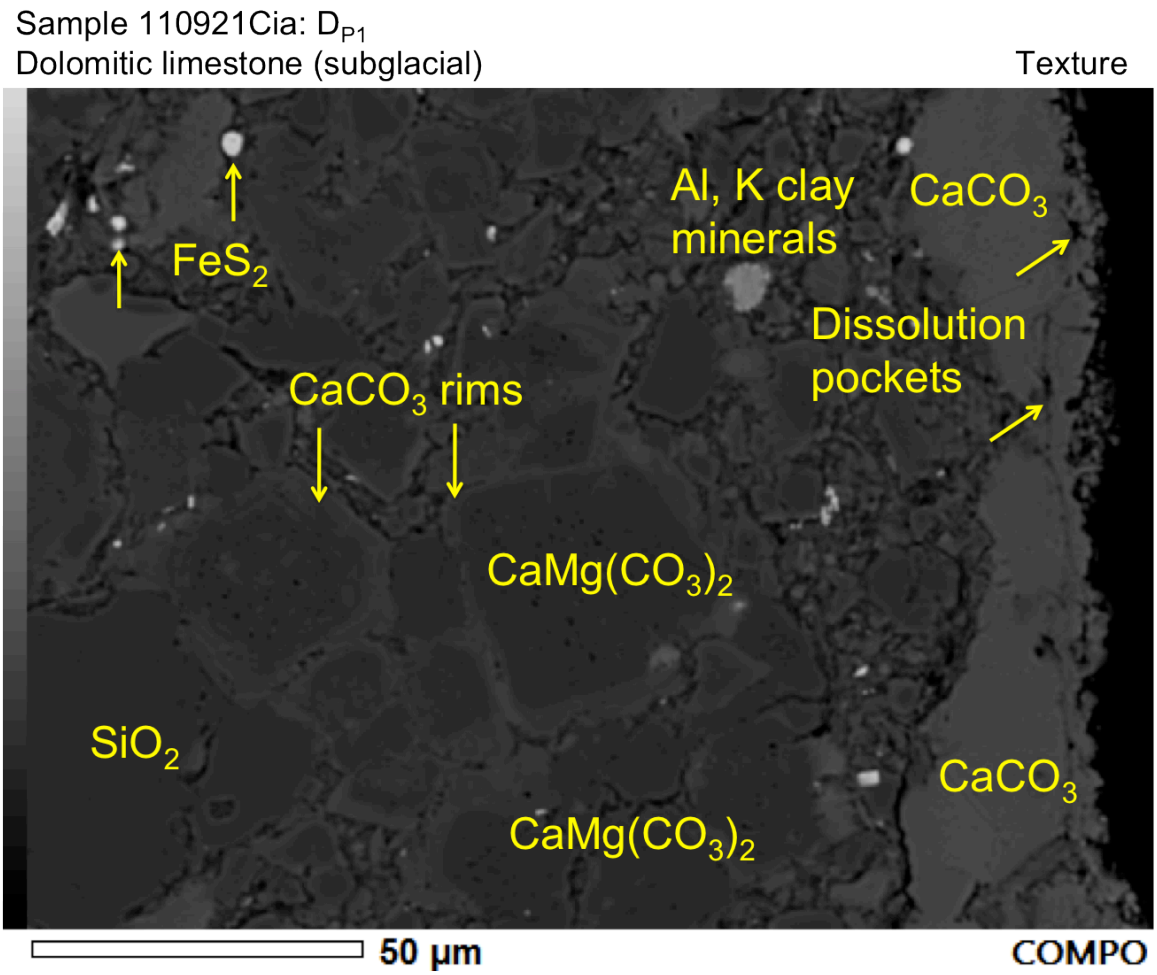

Figure 4.8. Subglacial Palliser Fm example of mineral-grain dissolution. Pits and pockets due to dissolution are observed at the weathered surface, a relict calcite vein. Note the calcite rims around dolomite crystals in the rock groundmass.

4.3.2. Chemistry

The textural evidence for weathering rinds described above is accompanied by geochemical changes mainly due to carbonate dissolution. Both grain-boundary dissolution (Figures 4.5 and 4.6) and mineral-grain dissolution (Figure 4.8) are indicated by the presence of voids resulting from the removal of soluble carbonate minerals. Electron microprobe analyses of areally-averaged transects inward from the rocks' surfaces show a general trend of decreasing Ca^{+2} cation abundances in the upper millimeter. One such example is shown in Figure 4.9. Calcium-silicon ratios decrease with distance into the rock rind. One outlier, shown in Figure 4.10, shows an inverse trend. This trend is inferred to be due to a relict calcite vein composing the weathered surface of this rock. The morphology of the veins observed in Figure 4.6 and 4.10 are comparable to the surface calcite layer in Figure 4.8. These surface features do not exhibit layering, as would be expected if they were depositional in nature, but rather are composed of proportionately large calcite crystals (Figure 4.8), giving weight to the relict calcite vein hypothesis.

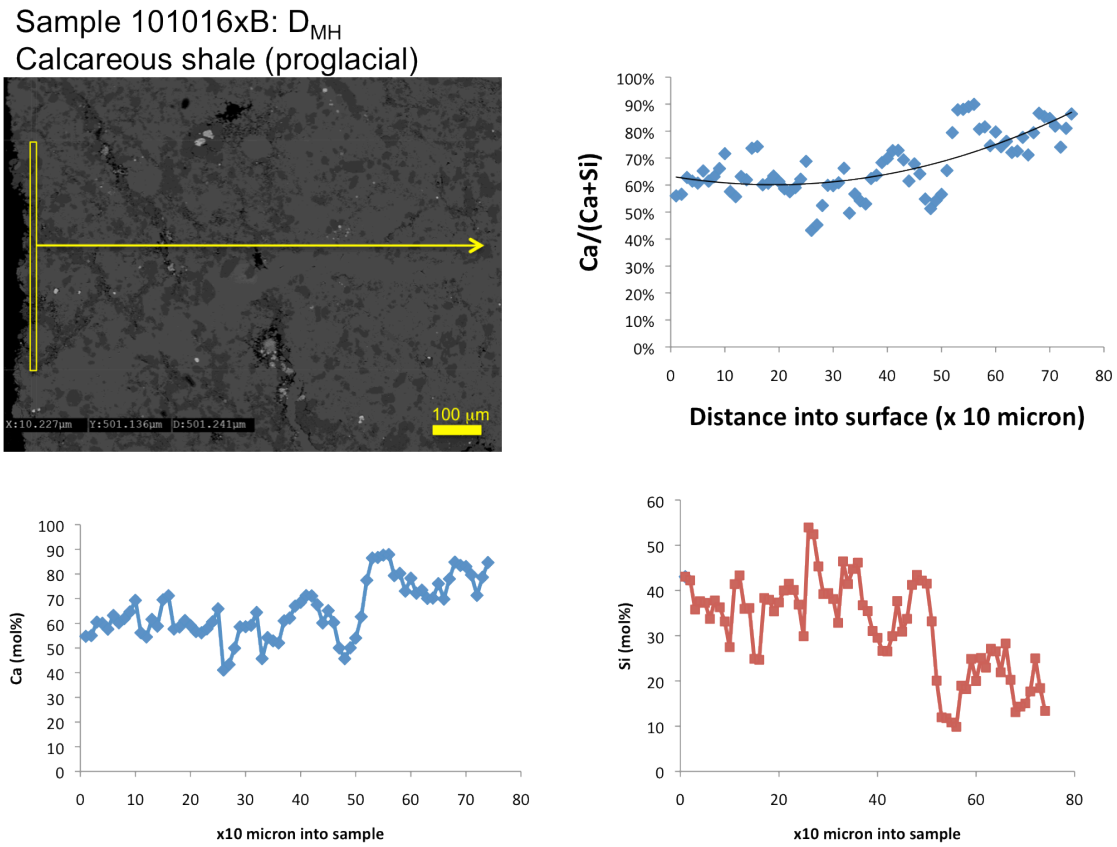

Figure 4.9. Example of EDS transect into proglacial Mount Hawk Fm sample (Figure 4.4), magnification 110X. Average spectra were collected over 10 µm x 500 µm areas (represented by yellow boxes), and measurements were repeated ~770 µm into sample. Lower plots show CaO (blue) and SiO (red) profiles into sample. Upper plot represents overall increasing trend of CaO relative to total CaO + SiO.

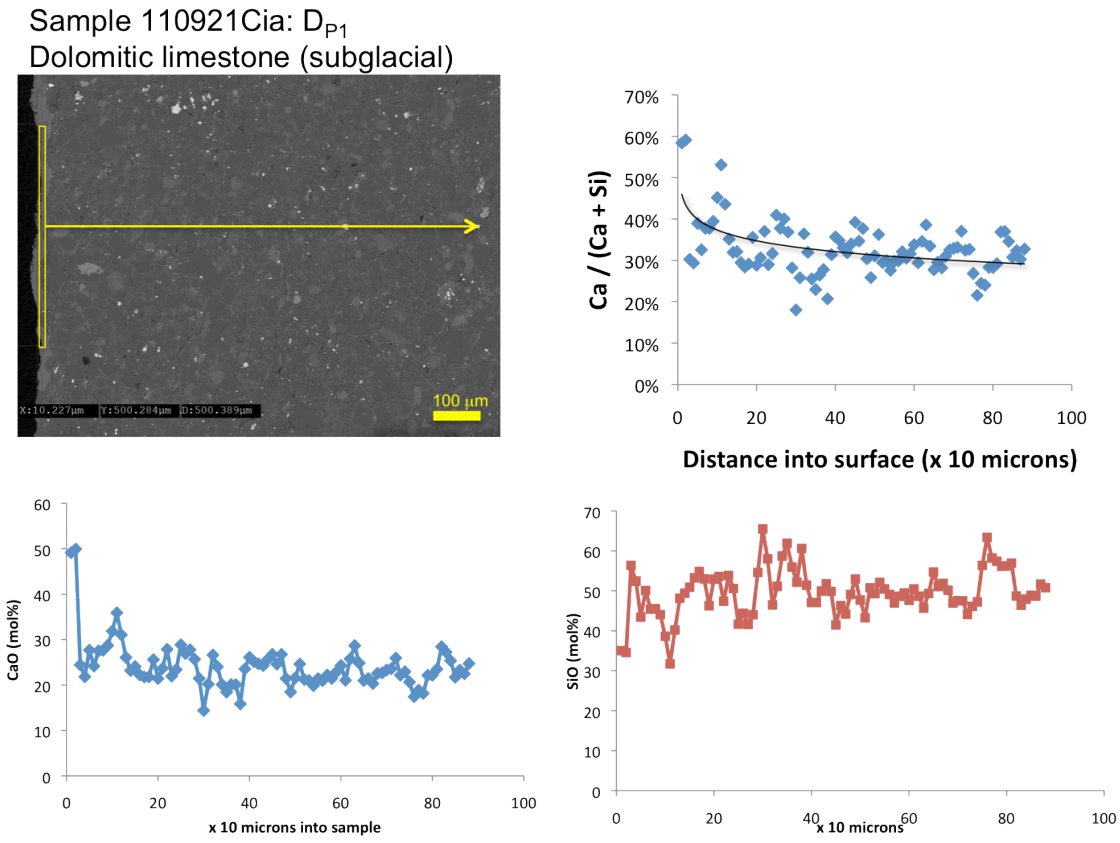

Figure 4.10. Example of EDS transect into subglacial Palliser Fm sample (Figure 4.7), magnification 110X. Average spectra were collected over 10 µm x 500 µm areas (represented by yellow boxes), and measurements were repeated ~900 µm into sample. Lower plots show CaO (blue) and SiO (red) profiles into sample. Upper plot represents overall decreasing trend of CaO relative to total CaO + SiO due to a calcite vein at the weathered surface.

4.3.3. Evidence for Pyrite Oxidation

The observed porous textures are strongly associated with the presence of pyrite and iron oxides, indicating a probable role for sulfuric acid in rock weathering (see Chapter 2 for further discussion). When subglacial waters contact iron sulfide crystals at the till bed, these iron-bearing minerals are exposed to oxygenated fluids, which results in sulfuric acid weathering of the surrounding carbonate crystals. Pyrites weathering and forming iron oxides are observed approximately 300 μm into one sample (Figure 4.11), indicating depth of fluid penetration. Weathered pyrite crystals are also associated with clays, which could provide a more permeable path from the sample exterior to the interior (Figure 4.12). Permeability is inferred from the amount of void space within the rock rinds (Figures 4.5 and 4.12).

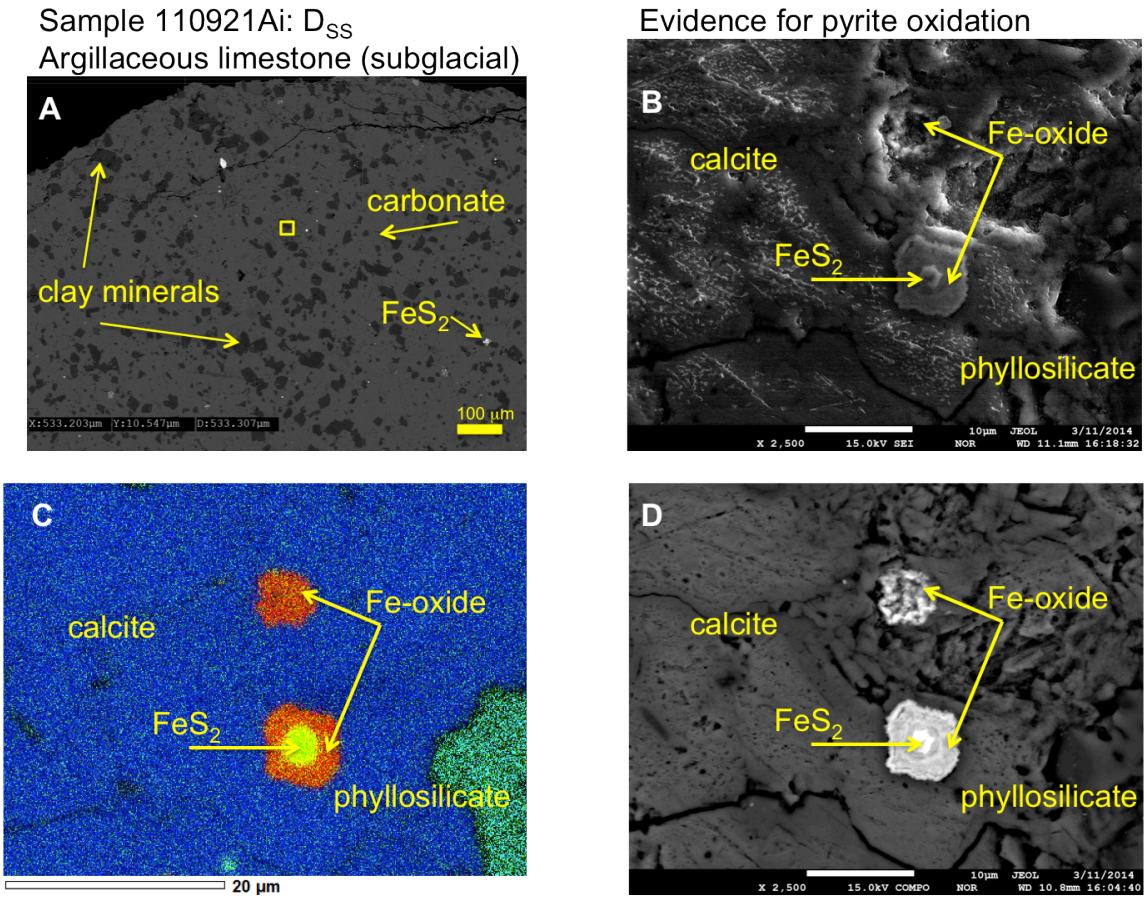

4.11. Evidence for pyrite oxidation in a subglacially-weathered sample. (A) Backscatter electron image; (B) secondary electron image of Fe_2S crystal surrounded by layers of iron oxide, ~300 µm from weathered surface (2,500X magnification); (C) EDS map of Fe_2S crystal surrounded by Fe-oxide, associated with calcite crystals and Al-K phyllosilicates; and (D) backscatter electron image of Fe_2S crystal and associated Fe-oxides.

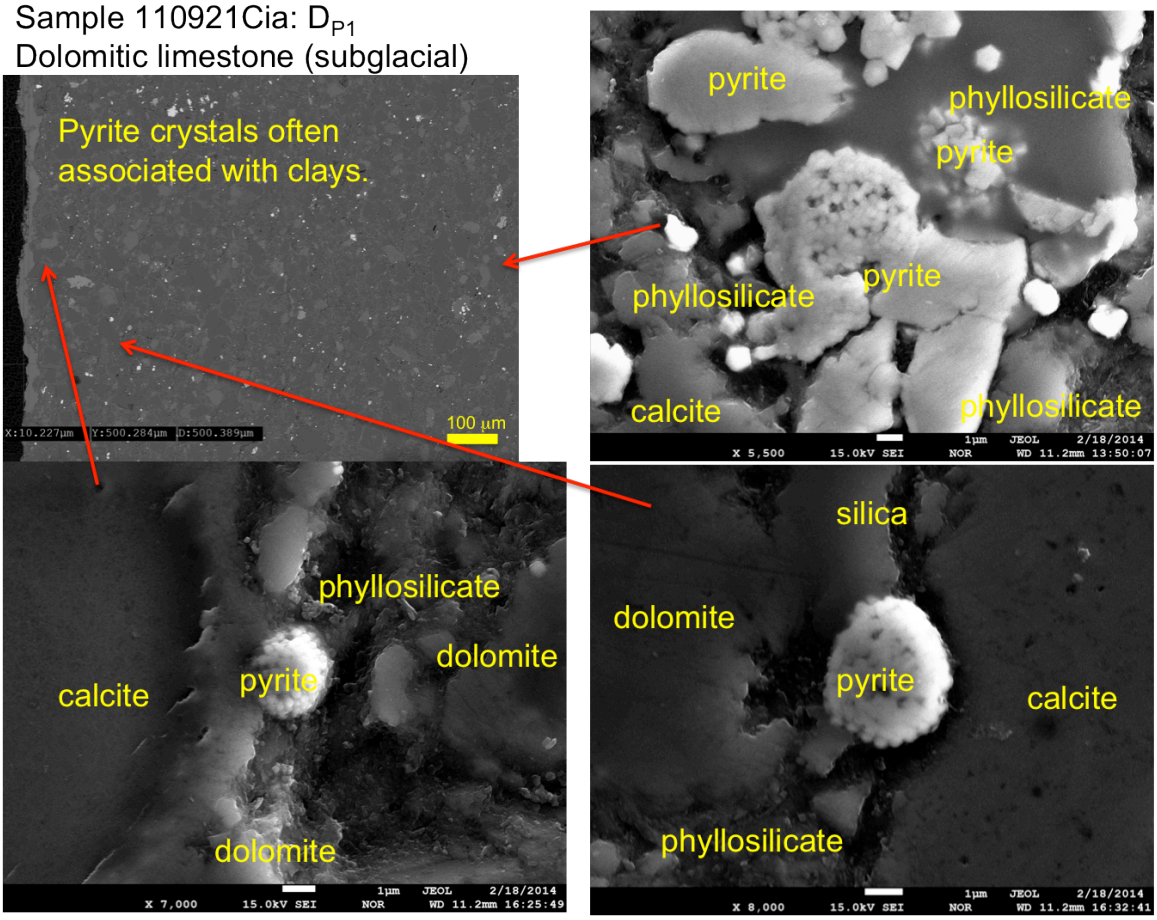

Figure 4.12. Fe_2S nodules are often associated with Al-K phyllosilicate minerals along planes up to ~800 µm from the weathered surface, implying potential access for surface waters. Images shown are backscattered electron (upper left) and secondary electron (5,500-8,000X magnification).

4.4. Discussion and Conclusions

The complex nature of weathering rinds formed by low-temperature weathering has received little attention until recently, and is still not well understood. This study investigates the formation of weathering rinds in glacially-altered, carbonate-clastic rocks. The weathering rinds presented in this study are evidently dominated by the dissolution of mineral grains by glacial meltwaters penetrating the rocks through preexisting fractures or clay mineral zones. The dissolution of carbonate minerals is accomplished through acidic weathering, probably dominantly sulfuric acid forming from pyrite oxidation within these rinds. Mineral-grain and grain-boundary dissolution has resulted in these weathering rinds exhibiting considerable porosity.

The fairly thin ($\leq$ 1 mm) weathering rind thicknesses are potentially controlled by glacial flow, *i.e.* the mechanical comminution of the subglacial till bed. As weakened zones form at the rock surface due to ion dissolution, void formation and fracturing, glacial action then pulverizes this outmost porous weathered zone. In the case of relict calcite veins being exposed at the rock surface through fracture, dissolution still takes place and a porous zone still occurs, but is prevented from migrating inward until dissolution pitting penetrates the surface "coating." Texturally speaking, no layered depositional coatings are observed in these samples.

Weathering rinds are abundant at Robertson Glacier. From previous aqueous geochemistry work in this valley (*Sharp et al.* [2002]; Chapter 2) and work in the geology of these cobbles (Chapter 3), it is obvious that acidic weathering - due to pyrite oxidation and atmospherically-coupled acid formation - plays a role in depleting the surfaces of glacially-associated rocks of carbonate minerals. This microscopic

investigation of weathering rinds shows that pyrite oxidation plays a dominant role in these surfaces' formation.

In conclusion, this study finds that discontinuous weathering rinds characterize the surfaces of clastic-carbonate cobbles from Robertson Glacier, Canada. These rinds are porous, thin, and form through the preferential dissolution of carbonate minerals. Weathering rind voids are strongly associated with the oxidation of pyrite, indicating the source of dissolution is primarily sulfuric acid. Their overall thickness is most likely controlled by low-temperature reaction rates, fluid flow rates, and glacial comminution.

The findings of this study strongly argue for further study of chemical weathering in glaciated terrains. While chemical processes clearly play a significant role in rock breakdown and ion transport, cold regions are still often thought of in terms of primarily mechanical weathering. The paradigm of future study should be that of chemical-mechanical breakdown of rock by glacial action and meltwaters.

CHAPTER 5

HYPSOMETRY OF LOBATE DEBRIS APRONS ON MARS

5.1. Introduction and Background

It has long been known that geologic features on Mars show evidence of modification by water and water ice [*Lucchitta*, 1981; *Squyres*, 1984; *Baker et al.*, 1992; *Parsons and Head*, 2005]. Past obliquity variations are theorized to have promoted the exchange of volatiles between the polar ice reservoirs and the midlatitude, allowing the accumulation of glaciers and the subsequent formation of periglacial terrain [*Fanale et al.*, 1986; *Head et al.*, 2003; *Forget et al.*, 2006].

Probable glacial features, such as lobate debris aprons (LDA), lineated valley fill (LVF), hourglass craters containing flow features concentric crater fill (CCF), and ice-cemented mantling deposits at the heads of gullies have been observed on the eastern rim of Hellas Basin and in Deuteronilus Mensae, ranging from latitudes of 30°N to 60°N and 30°S to 60°S (Figure 5.1) [*Crown et al.*, 1992; *Tanaka and Leonard*, 1995; *Christensen*, 2003; *Forget et al.*, 2006; *Dickson et al.*, 2007; *Levy et al.*, 2009].

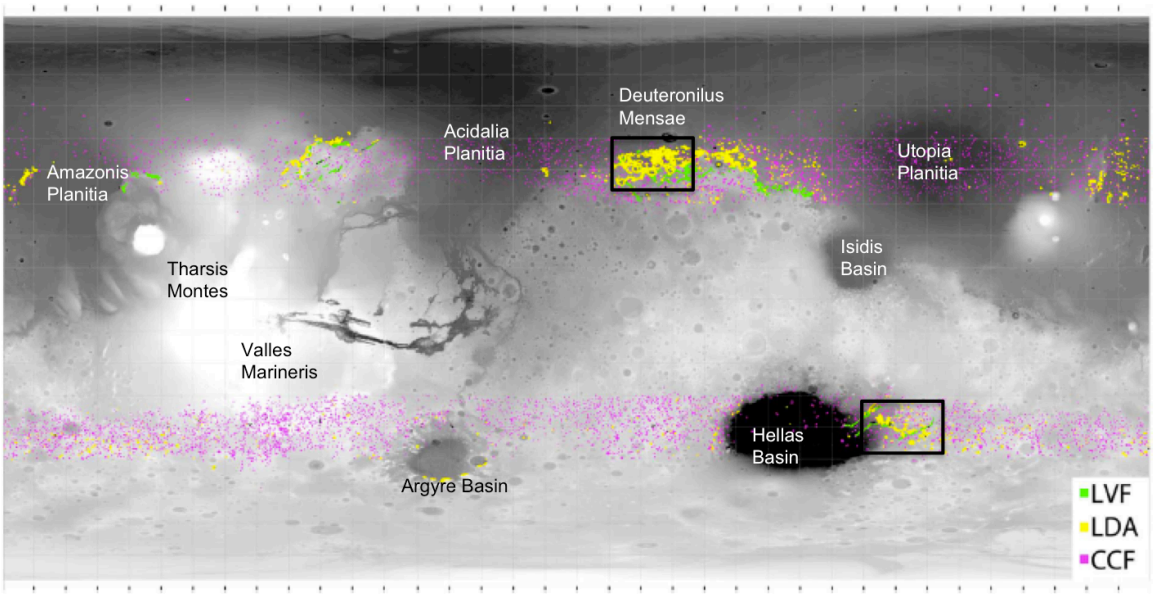

Figure 5.1. Distribution of midlatitude glaciers on Mars, with areas highlighted in this study outlined by black boxes and features of interest labeled. Icy features identified include linearted valley fill (LVF, in green), lobate debris aprons (LDA, in yellow) and concentric crater fill (CCF, in pink). Background is MOLA gridded topography, modified from *Levy et al.* [2014].

LDA originate at the base of steep massifs or scarps (Figure 5.2) and are characterized by lobes of gently sloping, convex-upward surfaces with relatively steep outer margins. The flow-like morphology of these features, including radial and concentric lineations, suggests these features formed by glacier-like viscous flow processes [*Pierce and Crown*, 2003; *Head et al.*, 2005]. The shallow radar (SHARAD) instrument aboard the Mars Reconnaissance Orbiter (MRO) returned results for these features consistent with massive ice deposits, supporting the hypothesis that these are

debris-covered glaciers [*Holt et al.*, 2008; *Plaut et al.*, 2009]. These features are thought to have formed from atmospheric precipitation of water ice during the late Amazonian [*Forget et al.*, 2006]. Studies using Thermal Emission Imaging System (THEMIS) analyses indicate that the surface temperature of debris aprons is cooler than the surrounding terrain, implying that the aprons are probably armored by relatively fine material compared to the surrounding material [*Piatek and Moersch*, 2007]. The ice is thought to have precipitated and flowed during climate excursions and became covered with debris during or towards the end of its emplacement [*Fastook et al.*, 2014].

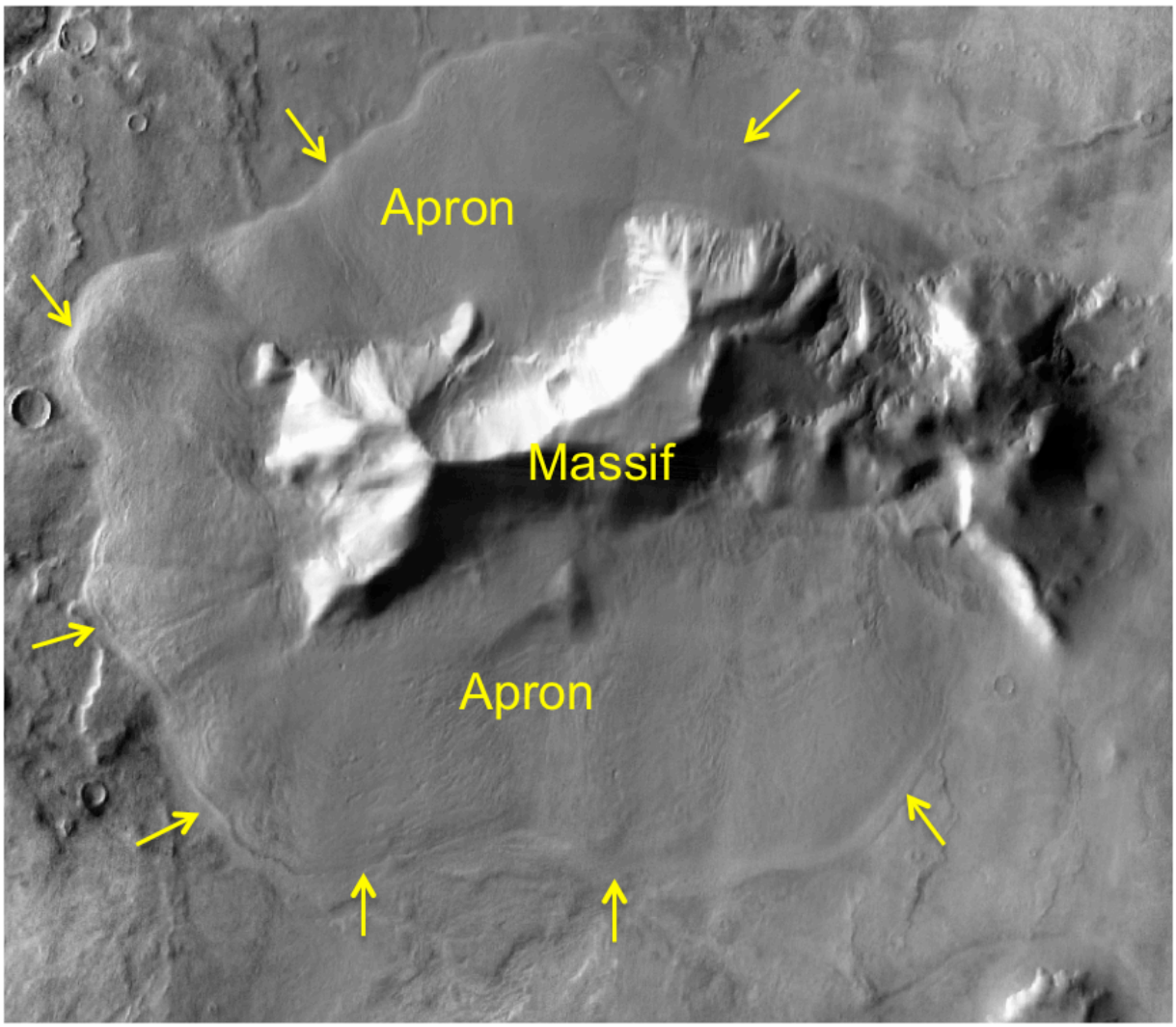

Figure 5.2. Typical LDA on the eastern rim of Hellas Basin, surrounding a central massif. Image centered at 45°S, 102°E. Imagery is THEMIS Day infrared imagey from the Global Mosaic [*Christensen et al.*, 2009]. Arrows indicate glacier snout.

Fastook et al. [2014] modeled LDA formation and found that collapsing regional ice sheets, coupled to a changing climate, is likely to be responsible for the formation of LDA (Figure 5.3).

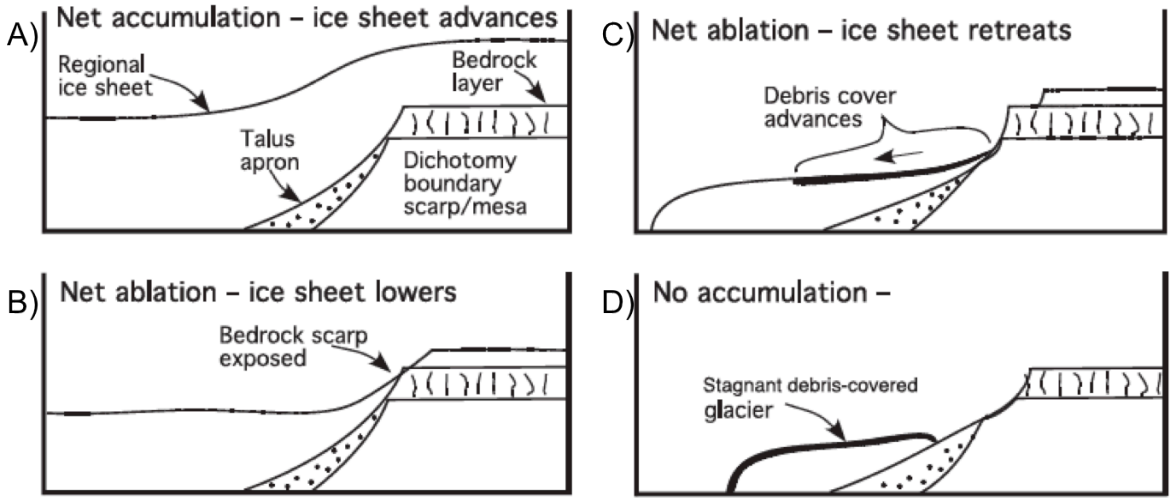

Figure 5.3. Possible formation mechanism for LDA proposed and modeled by *Fastook et al.* [2014]. (A) Larger regional ice sheet that buries topography. (B) As ice sheet collapses in ablating environment, surface drops below scarp level and debris begins to accumulate on ice surface. (C) Debris cover armors the surface and reduces sublimation (ablation). (D) As initial armoring begins, ice sheet evolves a surface slope and carries debris away from the scarp. As ice sheet collapse continues, the entrained debris reached the glacier snout and encompasses the entire LDA with an armored surface. Final LDA thickness and extent are controlled by sublimation and temperature in the *Fastook et al.* [2014] model.

These fairly young icy features, which contain the greatest volume of mid-latitude ice deposits [*Levy et al.*, 2014] are especially important because they represent significant amounts of present-day, near-surface ice, with implications for martian climate and geologic history, studies of the regional and global water distribution, and astrobiology studies. This study characterizes the area-elevation relationship, or hypsometry, of large glacial features known as lobate debris aprons (LDA) on the surface of Mars.

5.2. Materials and Methods

Terrestrial glaciology uses the hypsometric curve, or the empirical cumulative distribution function of elevations, as a method of constraining parameters such as the equilibrium line altitude (ELA) and mass balance of a glacier [*Adhikari and Marshall*, 2012]. ELA is the position, or elevation, at which accumulation is balanced by ablation. Mass balance, the difference between accumulation and ablation, is crucial to the survival of a glacier over time. Both these parameters can serve as key indicators of climate change, as they are closely related to temperature and precipitation.

We apply terrestrial glaciology inventory methods to the lobate debris aprons on the eastern rim of Hellas Basin and in the northern region of Deuteronilus Mensae, Mars to complete a detailed areal inventory of the buried ice deposits and to evaluate the hypsometric curve of each feature. We then examine the relationship between LDA hypsometry, latitude and elevation in order to understand the effect of past climatic variations on present-day, nonpolar ice distribution. Finally, we compare the hypsometric

curves and distribution of different curve types of the Deuteronilus Mensae population of LDA to the eastern Hellas population.

The Thermal Emission Imaging System (THEMIS) daytime infrared 100m Global Mosaic was used in conjunction with Mars Reconnaisance Orbiter Contact Camera (CTX) images to determine areal extent, and Mars Orbiter Laser Altimeter (MOLA) data were used to ascertain elevations [*Edwards et al.*, 2011]. The JMARS geographic information system software, developed at Arizona State University was used to process and assess these datasets (Figure 5.4 and 5.5) [*Christensen et al.*, 2009].

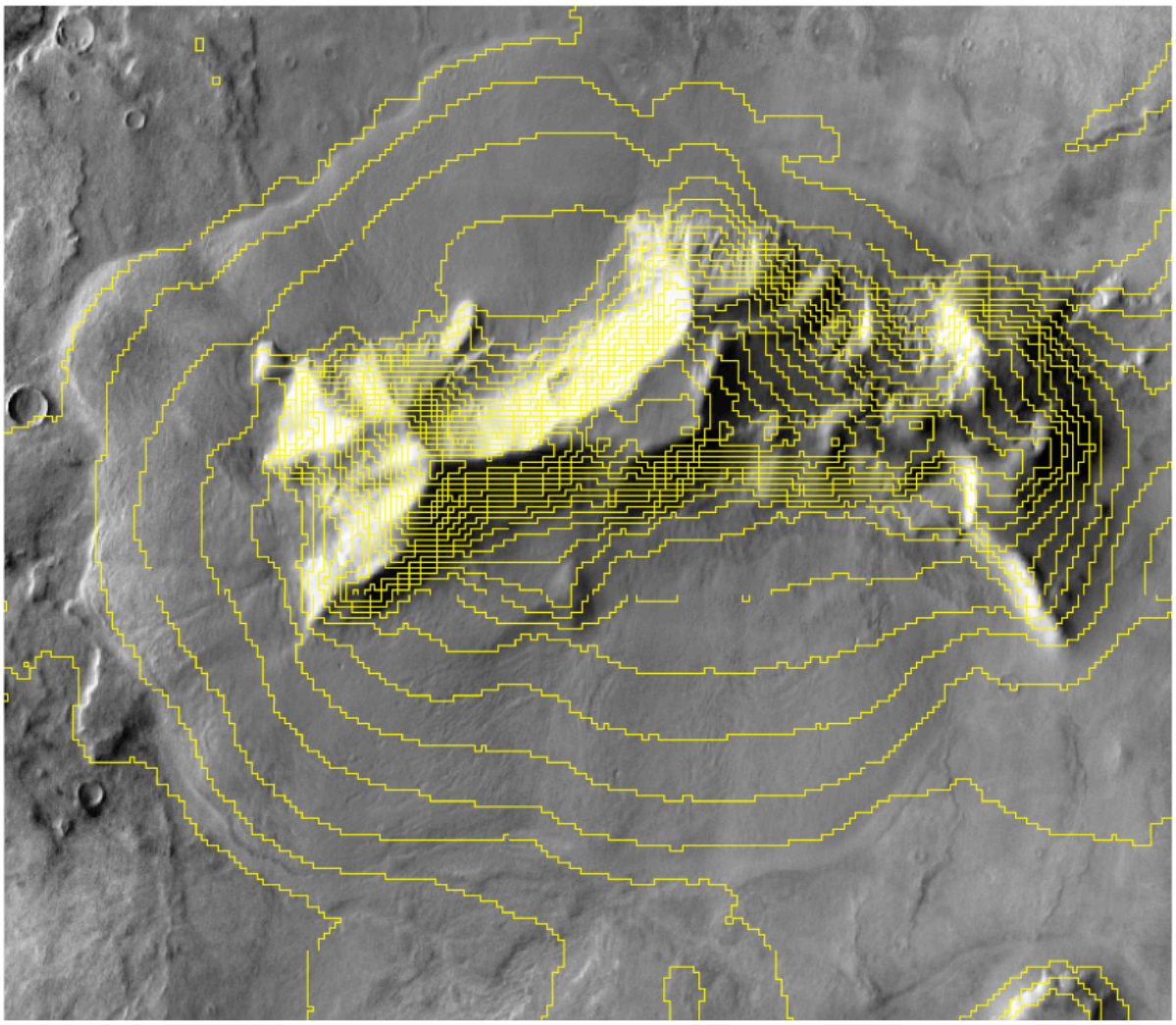

Figure 5.4. An example of the mapping method used in JMARS to determine the area-elevation bins used when determining the hypsometric curve of an LDA. THEMIS day IR base imagery overlain with MOLA elevation contours. Image centered at 45°S, 102°E.

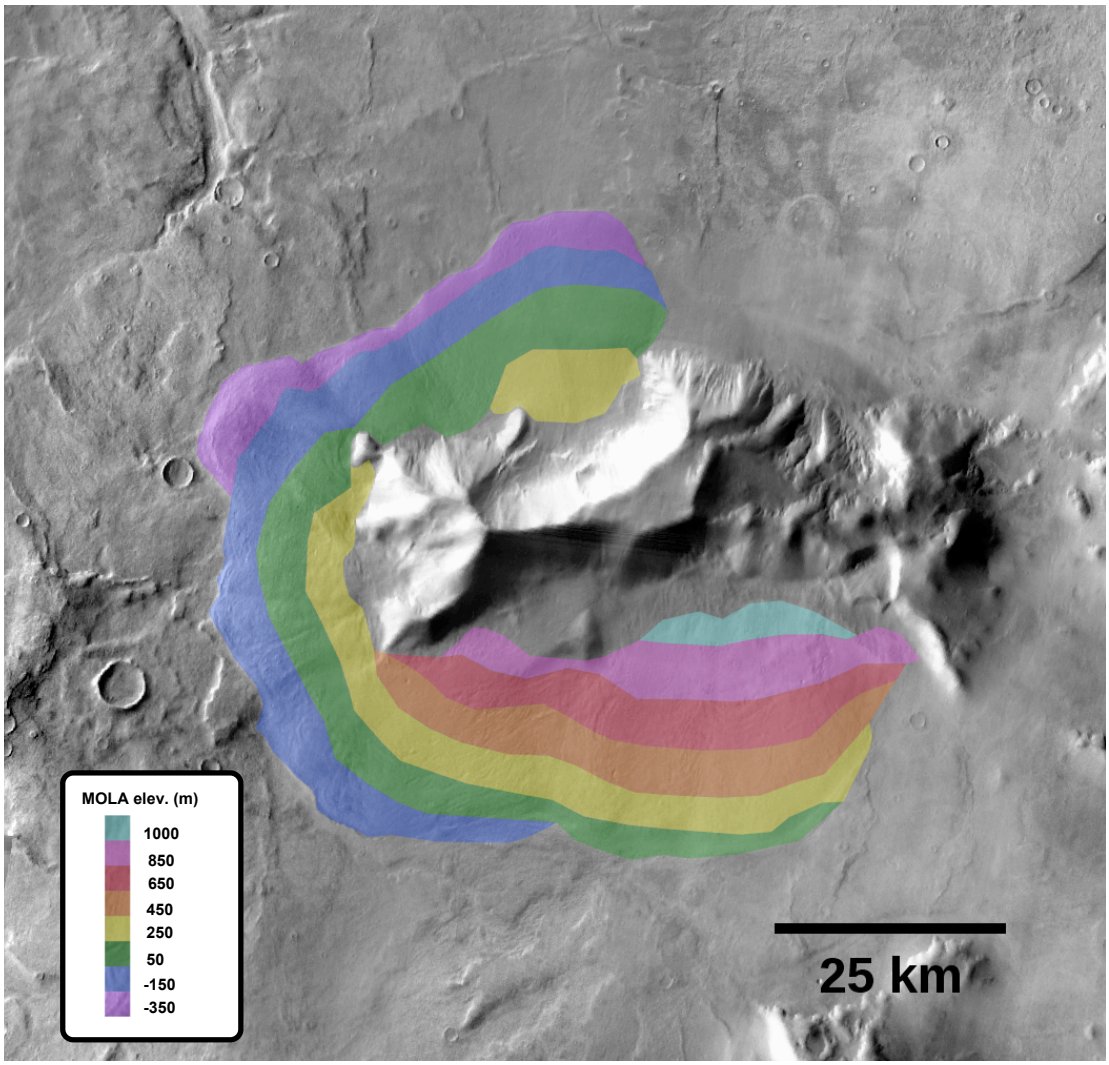

Figure 5.5. Sample hypsometric analysis of a high-elevation, higher-latitude lobate debris apron (LDA) surrounding a massif on the eastern rim of Hellas Basin, identified in Figure 5.1. Base imagery is THEMIS daytime infrared imagery in JMARS [*Christensen et al.*, 2009]. The base of the apron is at MOLA elevation -350m and it is centered at 45°S, 102°E. Average elevation bins are identified by color.

5.3. Results

Results from this survey show that in both the northern and southern populations, LDA exhibit three types of hypsometric curves: those with a single peak, classified as Type I curves; those with curves with two peaks where the downslope peak is larger than the upslope peak, classified as Type II; and double-peaked curves, where the upslope curve is larger than the downslope peak, classified as Type III (Figure 5.6.).

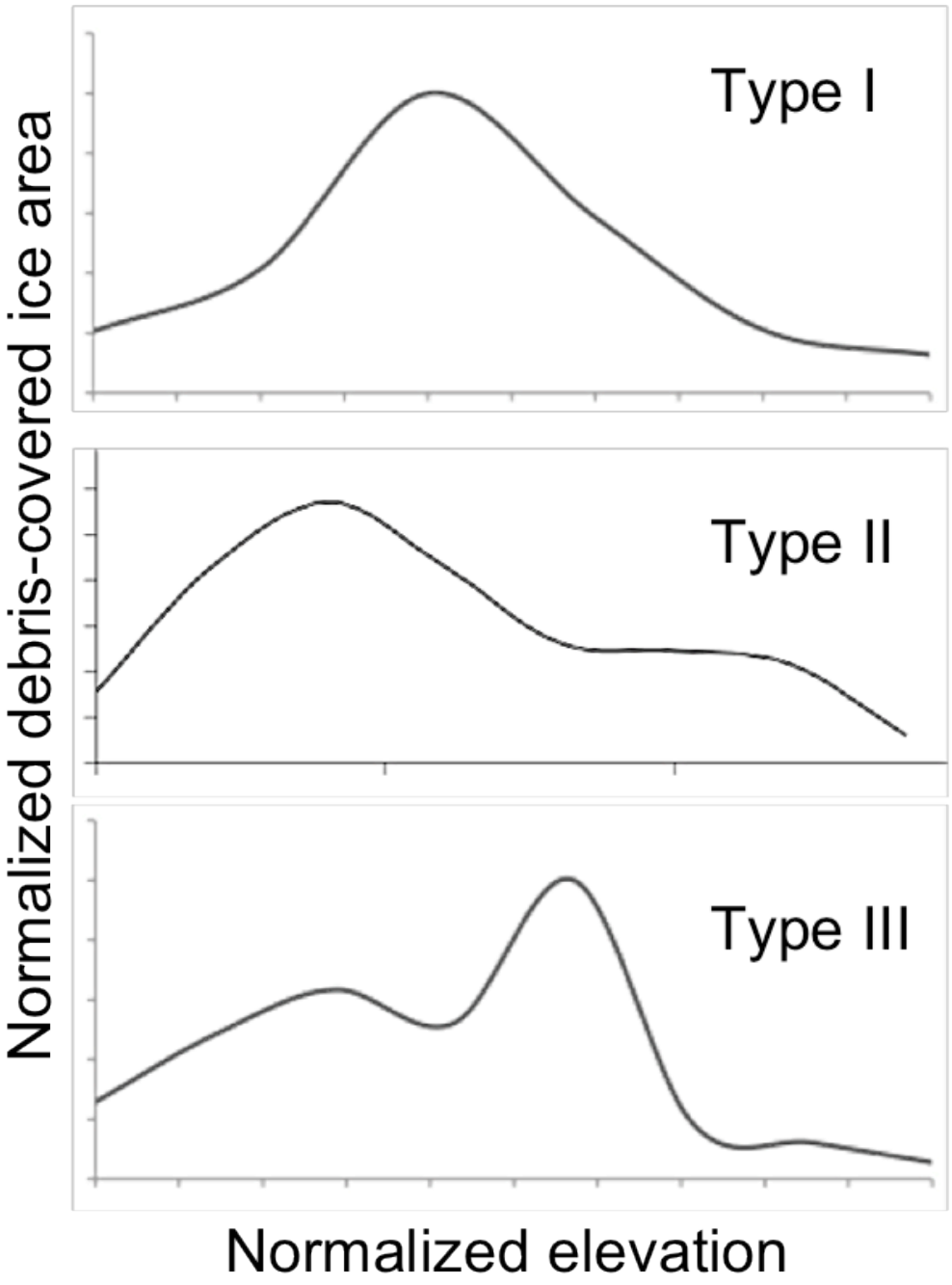

Figure 5.6. Types of hypsometric curves observed on LDA on Mars. Type I: A hypsometric curve similar to classic terrestrial alpine glaciers; the curve is steep at the upper and lower boundaries, and flattens in the midsection. This type of curve is indicative of a typical glacier with preserved (relict) accumulation and ablation zones.

For the southern population in eastern Hellas, at elevations above 500m MOLA, LDA exhibit hypsometric curves with a single peak, classified in this study as Type I curves. At MOLA elevations between -2000m and 500m, LDA hypsometry exhibits curves with two peaks, where the downslope peak is larger than the upslope peak (Figure 5.6.) These curves, classified as Type II, are similar to classic terrestrial alpine glaciers – they can be indicative of a typical glacier with both accumulation and ablation zones, and could potentially be used to determine the (probably defunct) equilibrium line altitude of a lobate debris apron. Finally, LDAs below -2000m MOLA elevation generally exhibit double-peaked curves, were the upslope curve is larger than the downslope peak. These hypsometric curves have been classified as Type III. Figure 5.7 illustrates the relationship of curve type to elevation and latitude. The observed change in hypsometry with elevation at Hellas Basin potentially signals a past shift in temperature and precipitation dependent on elevation.

Results from Deuteronilus Mensae indicate that the northern population of LDA exhibit Types I or Type II hypsometric curves, with no apparent trend with latitude or elevation (Figure 5.7). This lack of change in hypsometry with latitude could signal a regional trend, such as a large collapsing ice sheet during a climate shift. The ice sheet would have to be large enough to remain unaffected by local topography, as proposed in *Fastook et al.* [2014].

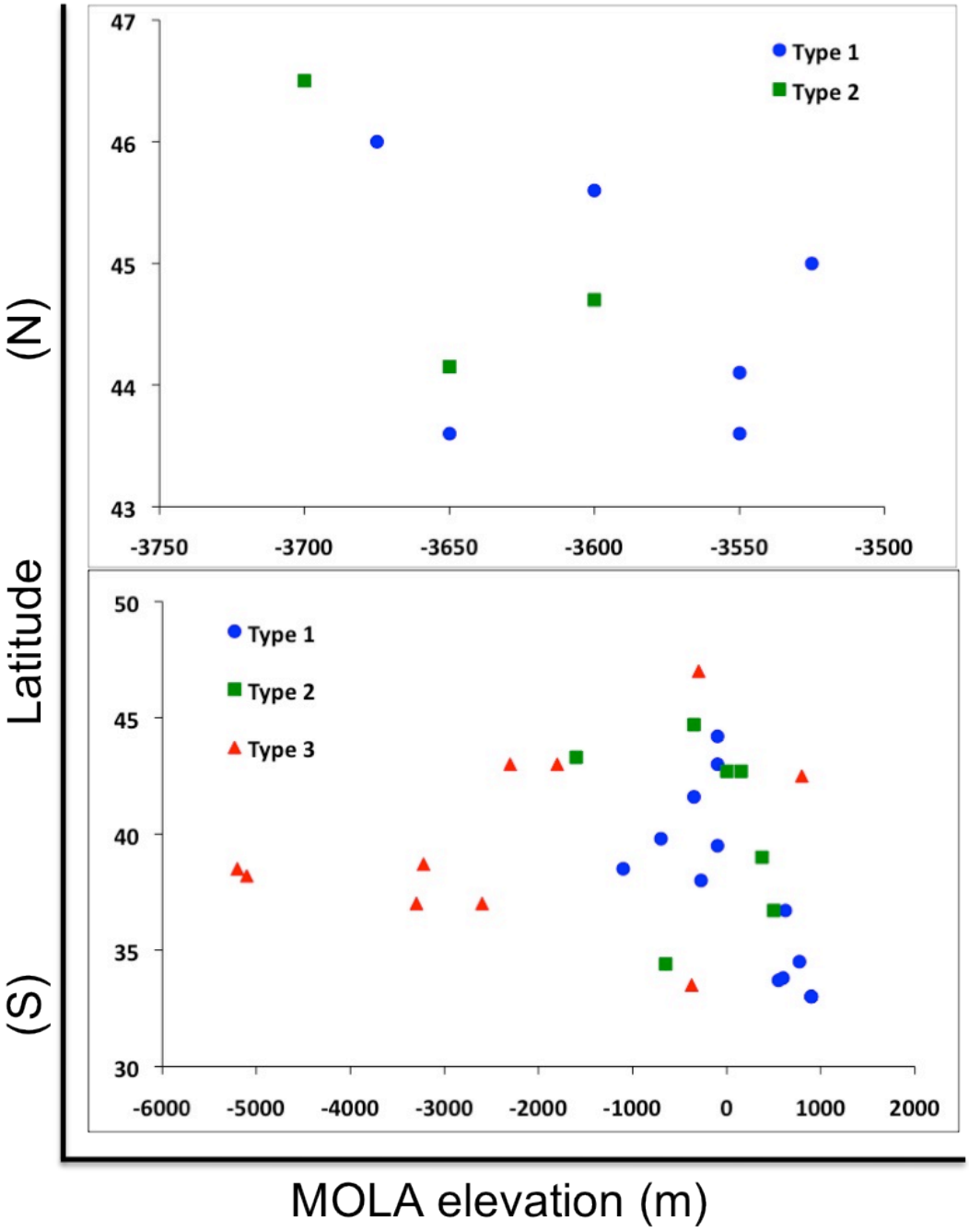

Figure 5.7. Hypsometric type distribution, plotted as base elevation versus latitude. The northern (Deuteronilus Mensae) population of LDA show no discernible trend but contain both Types I and II. No Type III curves are present in the northern population.

Figure 5.7. (cont'd) The southern (east Hellas) population exhibit all three types of curves, with the majority of Type III curves confined to the lowest elevations.

5.4. Discussion and Conclusions

Based on the observed results, several trends can be seen. The northern and southern LDA populations differ in that only the southern Hellas population has hypsometric curves of Type III. Types I and II appear to be somewhat dependent on elevation in the southern population, while in the northern population there appears to be no clear distinction between Types I and II based on elevation or latitude. Based on the three curve types, several conceptual models for formation can be proposed (Figure 5.8). These conceptual flow regimes coupled to hypsometry are consistent with *Fastook et al.* [2014] findings, which concluded that LDA in Deuteronilus Mensae could not have experienced much further flow once the stabilized post-ice sheet collapse. In our model, the LDA at lower elevations in Hellas Basin, temperatures could have approached or reached the ice melting point post-armoring, leading to pulses of subsequent flow, and resulting in the hypsometry of Type III aprons.

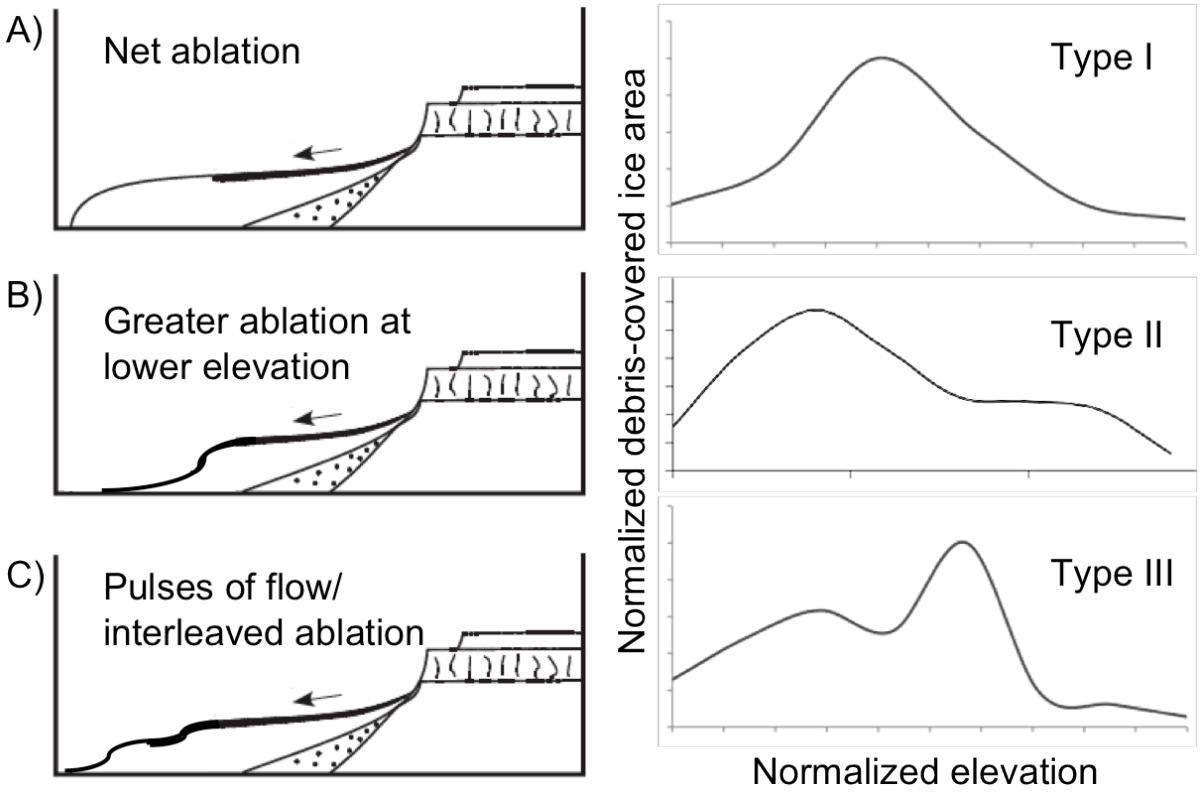

Figure 5.8. Potential formation mechanisms proposed for LDAs Types I, II, and III. Modified from *Fastook et al.* [2014]. (A) Debris cover advances as ablation begins, sublimation lag forms and armors surface against further sublimation. This process effectively preserves original glacial flow form, resulting in a hypsometric Type I, similar to terrestrial alpine glaciers. (B) Debris cover/surface armoring forms slowly while ablation thins the glacier terminus. This results in a hypsometric curve of Type II, in which the bulk of ice is preserved at higher local elevations. (C) Debris cover/sublimation lag forms while glacier continues to experience pulses of temperature-induced flow due to elevation; but accumulation ceases as the regional ice sheet has collapsed. This process results in a hypsometric curve Type III, wherein glacial ice is preserved in multiple lobes/volume stored at lower elevations.

This study characterized the area-elevation relationship, or hypsometry, of large glacial lobate debris aprons on the surface of Mars. The hypsometry of these large, debris-covered icy features, which formed around scarps in Mars' midlatitudes, gives us insight into their past flow regime and allows us to make predictions about past climate scenarios in the Late Amazonian (~700 Ma to ~100 Ma) that allowed snow and ice to accumulate and flow. The LDA in this study were found to fall into three major groups, strongly dependent on scarp elevation, implying regional controls on ice flow. The LDA at the lowest elevations on the rim of Hellas Basin likely experienced temperatures close to the melting point, allowing flow after LDA at higher elevations had stagnated due to changing climate conditions.

CHAPTER 6

CONCLUSION

This study examines glacial processes, chemical and physical, on Earth and Mrs. First, I use multidisciplinary methods to examine the weathering regime of Robertson Glacier, a small alpine glacier in a carbonate-clastic catchment. Aqueous geochemistry data show that multiple carbonate dissolution reactions are occurring in different zones of the valley. The subglacial system is dominated by carbonate dissolution due to sulfuric acid, which is formed through microbial pyrite oxidation in subglacial sediments, while the deglaciated till plain is dominated by carbonic acid dissolution due to atmospheric interactions. These findings imply a more active microbial population in the subglacial environment, which is in line with previous studies [*Sharp et al.*, 2002; *Boyd et al.*, 2011; *Hamilton et al.*, 2013]. TIR spectroscopy shows that dissolution signatures are detectable on rock surfaces at laboratory and orbital scales. The signature detection is extended to other valleys in the region with remote sensing data, finding that NW-facing valleys have a more detectable weathering signature than SE-facing valleys. It is proposed that regional topography controls runoff rates, leading the high-insolation southern valley to lack a detectable weathering signature. Finally, glacially-weathered carbonate rock surfaces are characterized with electron microscopy, which shows evidence for thin, porous weathering rinds. These rinds are characterized by chemical trends caused by carbonate dissolution, most likely due to sulfuric acid formed by pyrite oxidation.

Second, the area-elevation relationship, or hypsometry, of large glacial features known as lobate debris aprons (LDA) on the surface of Mars is characterized. The

hypsometry of these large, debris-covered icy features, which formed around scarps in Mars' midlatitudes, provides insight into their past flow regime and allows us to make predictions about past climate scenarios that allowed snow and ice to accumulate and flow. The LDAs in this study were found to fall into three major groups, strongly dependent on scarp elevation, implying regional controls on ice flow during emplacement by a regional ice sheet. A thinning atmosphere and associated climate change was most likely the major control of stagnating ice flow.

Glacial processes, both chemical and weathering, have affected planetary surfaces throughout the Solar System. Biological processes enhancing mineral breakdown affect how glacial weathering functions on Earth, contributing positive inputs to the global carbon cycle. If biology was once present under the ice on Mars, similar signatures may be detectable at orbital and rover scales. In terrestrial subglacial systems dominated by crystalline and noncarbonate sedimentary rocks, carbonate dissolution nonetheless dominates total solute fluxes [*Sharp et al.*, 1995; *Anderson et al.*, 2000; *Tranter*, 2003]. Thus, on the glaciated basaltic-andesitic surface of Mars, one might expect a similar incongruent weathering system to develop. As much as 10% of Mars' observed ice is sequestered in flowing, glacial form today [*Levy et al.*, 2015]. If these glacial forms were wet-based glaciers during past climate excursions, subglacial carbonate dissolution should have played a significant role in weathering the surface of Mars. Terrestrial analog studies on glaciated basalt flows could provide insight into pertinent weathering processes. Proposed sites for future study are highlighted in Figure 6.1.

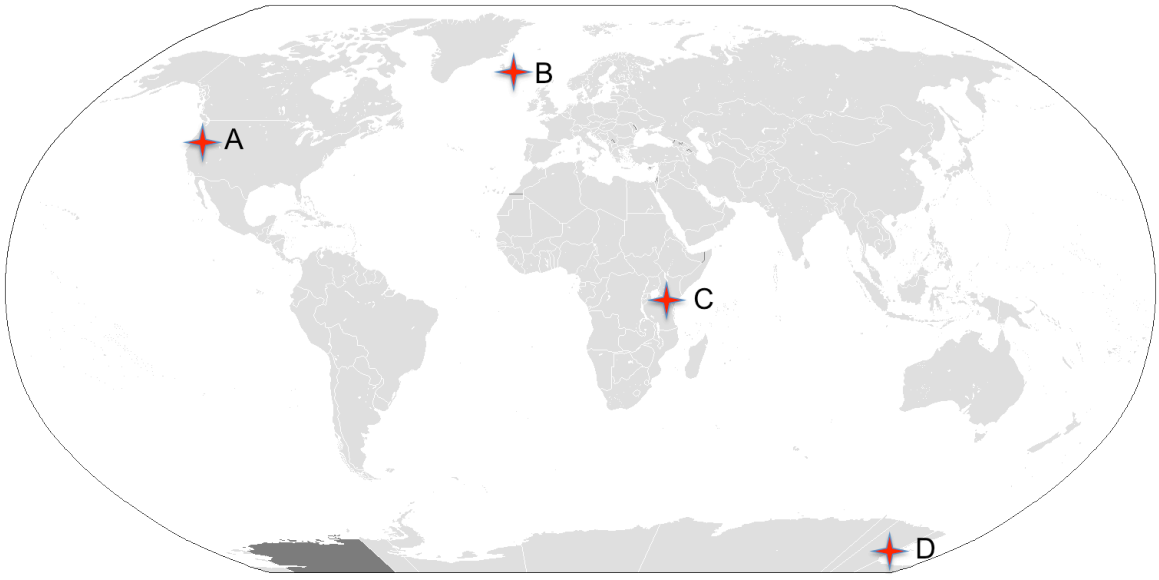

Figure 6.1. Map highlighting terrestrial analogs to Mars glaciers. All highlighted sites contain glaciers overriding mafic terrain. A) Collier Glacier, Oregon, USA; B) Skaftafellsjökull Glacier, Iceland; C) Southern Ice Field, Kilimanjaro, Tanzania; D) Taylor Glacier, Dry Valleys, Antarctica.

Glacier beds are active, dynamic weathering systems, harboring diverse communities of chemolithotrophic microorganisms. In recent years their significance as both agents of weathering and role as living ecosystems has begun to be recognized. This work adds weight to the argument that glacial systems are an important link in the global weathering and biogeochemical cycles (*e.g.* the carbon and strontium cycles), and may have played a similar role in weathering the surface of Mars in the past.

REFERENCES

Adhikari, S. and S. J. Marshall (2012), Glacier volume-area relation for high-order mechanics and transient glacier states, Geophys. Res. Lett., 39(L16505), doi:10.1029/2012GL052712.

Anderson, S. P., J. I. Drever, C. D. Frost, and P. Holden (2000), Chemical weathering in the foreland of a retreating glacier, *Geochimica et Cosmochimica Acta, 64*(7), 1173–1189.

Anderson, S. P., S. A. Longacre, and E. R. Kraal (2003), Patterns of water chemistry and discharge in the glacier-fed Kennicott River, Alaska: evidence for subglacial water storage cycles, *Chem. Geol., 202*(3-4), 297-312.

Anderson, S. P. (2007), Biogeochemistry of Glacial Landscape Systems, *Annu. Rev. Earth. Pl. Sc., 35*(1), 375–399, doi:10.1146/annurev.earth.35.031306.140033.

Baker, V. R., M. H. Carr, V. C. Gulick, C. R. Williams, and M. S. Marley (1992), Channels and valley networks, in *Mars*, ed. Kieffer, H.H., Tucson, Ariz., 493-522.

Ball, M. D. and D. G. McCartney (1981), The measurement of atomic number and composition in an SEM using backscattered detectors, *J. Microscopy, 124*, 57-68.

Bandfield, J. L., V. E. Hamilton, and P. R. Christensen (2000), A global view of Martian surface compositions from MGS-TES, *Science, 287*(5458), 1626-1630.

Bandfield, J. L., K. S. Edgett, and P. R. Christensen (2002), Spectroscopic study of the Moses Lake dune field, Washington: Determination of compositional distributions and source lithologies, *J. Geophys. Res., 107*(E11), 5092, doi:10.1029/2000JE001469.

Bottrell, S. H., and M. Tranter (2002), Sulphide oxidation under partially anoxic conditions at the bed of the Haut Glacier d'Arolla, Switzerland, *Hydrol. Process.*, *16*(12), 2363–2368, doi:10.1002/hyp.1012.

Boyd, E. S., R. K. Lange,M. Skidmore, A.C. Mitchell, C. Bakermans, and J.W. Peters (2010), Methanogenesis in subglacial sediments, *Environ. Microbio. Rep., 2*, 685–692.

Boyd, E. S., R. K. Lange, A. C. Mitchell, J. R. Havig, T. L. Hamilton, M. L. Lafrenière, E. L. Shock, J. W. Peters and M. Skidmore (2011), Diversity, abundance, and potential activity of nitrifying and denitrifying microbial assemblages in a subglacial ecosystem, *App. Environ. Microbiol., 77*, 4778-4787.

Boyd, E. S., T. L. Hamilton, J. R. Havig, M. L. Skidmore, and E. L. Shock (2014), Chemolithotrophic primary production in a subglacial ecosystem, *App. Environ. Microbiol., 80*, 6146-6153.

Casey, K. A. (2012) Supraglacial dust and debris: geochemical compositions from glaciers in Svalbard, southern Norway, Nepal and New Zealand, *Earth Syst. Sci. Data Discuss., 5*, 107-145, doi:10.5194/essdd-5-107-2012.

Casey, K. and A. Kääb (2012), Estimation of supraglacial dust and debris geochemical composition via satellite reflectance and emissivity, *Remote Sens., 4*, 2554-2575, doi:10.3390/rs4092554.

Casey, K. A., A. Kääb, and D. I. Benn (2012), Geochemical characterization of supraglacial debris via in situ and optical remote sensing methods: a case study in Khumbu Himalaya, Nepal, *The Cryosphere, 6*, 85-100, doi:10.5194/tc-6-85-2012/

Christensen, P. R., J. L. Bandfield, M. D. Smith, V. E. Hamilton, and R. N. Clark (2000a), Identification of a basaltic component on the Martian surface from Thermal Emission Spectrometer data, *J. Geophys. Res., 105*(E4), 9609-9621.

Christensen, P. R. J. L. Bandfield, V. E. Hamilton, D. A. Howard, M. D. Lane, J. L. Piatek, S. W. Ruff, and W. L. Stefanov (2000b), A thermal emission library of rock-forming minerals, *J. Geophys. Res., 105*(E4), 9735-9739.

Christensen, P. R. (2003), Formation of recent martian gullies through melting of extensive water-rich snow deposits, *Nature, 422*, 45-48.

Christensen, P. R., E. Engle, S. Anwar, S. Dickenshied, D. Noss, N. Gorelick, and M. Weiss-Malik (2009), JMARS – A Planetary GIS, *Amer. Geophys. Union Fall Mtg*, Abs. IN22A-06.

Clark, R. N. (1999), Spectroscopy of rocks and minerals, and principles of spectroscopy, in Rencz, A. N., ed., *Remote sensing for the Earth sciences, Manual of remote sensing*, Vol. 3 (third edition), New York, John Wiley and Sons, Inc., 3-58.

Cloutis, E. (2007) Analytical data for mineral and rock samples, *HOSERLab Mineral Database*, <c:\grants\analyses\Mineral_database_latest.doc>

Colman, S. M. and K. L. Pierce (1981) Weathering rinds on andesitic and basaltic stones as a Quaternary age indicator, *U.S. Geological Survey Professional Paper 1246*, 51 p.

Cooper, F. J., B. A. Adams, C. S. Edwards, and K. V. Hodges (2012), Large normal-sense displacement in the South Tibetan fault system in the eastern Himalaya, *Geology, 40*(11), 971-974, doi:10.1130/G33318.1.

Cox, A., E. Shock, J. Havig (2011), The transition to microbial photosynthesis in hot spring ecosystems, *Chemical Geology, 280*, 344-351.

Crown, D. A., K. H. Price, and R. Greeley (1992), Geologic evolution of the east rim of the Hellas Basin, Mars, *Icarus, 100*, 1-25.

Darmody, R. G., C. E. Thorn, R. L. Harder, J. P. L. Schlyter, and J. C. Dixon (2000), Weatehring implications of water chemistry in an arctic-alpine environment, northern Sweden, *Geomorphology, 34*, 89-100.

Dickson, J. L., J. W. Head, and M. Kreslavsky (2007) Martian gullies in the southern mid-latitudes of Mars: Evidence for climate-controlled formation of young fluvial features based upon local and global topography, *Icarus, 188*, 315-323 doi:10.1016/j.icarus.2006.11.020.

Dixon, J. C., C. E. Thorn, R. G. Darmondy, and S. W. Campbell (2002), Weathering rinds and rock coatings from an Arctic alpine environment, northern Scandinavia, *GSA Bulletin, 114*(2), 226-238.

Dixon, J. C., S. W. Campbell, C. E. Thorn, and R. G. Darmody (2006), Incipient weathering rind development on introduced machine-polished granite discs in an Arctic alpine environment, northern Scandinavia, *Earth Surf. Process. Landforms, 31*, 111-121.

Dorn, R. I. (1998) *Rock coatings*, Amsterdam, Elsevier, 429 p.

Edwards, C. S., P. R. Christensen, and V. E. Hamilton (2008), Evidence for extensive olivine-rich basalt bedrock outcrops in Ganges and Eos chasmas, Mars, *J. Geophys. Res., 113*(E11003), doi:10.1029/2008JE003091.

Edwards, C. S., K. J. Nowicki, P. R. Christensen, J. Hill, N. Gorelick, and K. Murray (2011), Mosaicking of global planetary image datasets: 1. Techniques and data processing for Thermal Emission Imaging System (THEMIS) multi-spectral data, *J. Geophys. Res., 116*(E10008), doi:10.1029/2010JE003755.

Etienne, S. (2002), The role of biological weathering in periglacial areas: a study of weathering rinds in south Iceland, *Geomorphology, 47*, 75-86.

Fairchild, I., L. Bradby, M. Sharp, and J.-L. Tison (1994), Hydrochemistry of carbonate terrains in alpine glacial settings, *Earth Surf. Process. Land., 19*, 33-54.

Fairchild, I. J., J. A. Killawee, B. Hubbard, and W. Dreybrodt (1999a), Interactions of calcareous suspended sediment with glacial meltwater: a field test of dissolution behavior, *Chem. Geol., 155*, 243-263.

Fairchild, I. J., J. A. Killawee, M. J. Sharp, B. Spiro, B. Hubbard, R. D. Lorrain, and J-L. Tison (1999b), Solute generation and transfer from a chemically reactive alpine glacial-proglacial system, *Earth Surf. Process. Landforms, 24*, 1189-1211.

Fanale, F. P., J. R. Salvail, A. P. Zent, and S. E. Postawko (1986), Global distribution and migration of subsurface ice on Mars, *Icarus, 67*, 1-18.

Fastook, J. L., J. W. Head, F. Forget, J.-B. Madeleine, and D. R. Marchant (2011), Evidence for Amazonian northern mid-latitude regional glacial landsystems on Mars: Glacial flow models using GCM-driven climate results and comparisons to geological observations, *Icarus, 216*, 23-39, doi:10.1016/j.icarus.2011.07.018.

Fastook, J. L., J. W. Head, and D. R. Marchant (2014), Formation of lobate debris aprons on Mars: Assessment of regional ice sheet collapse and debris-cover armoring, Icarus, 228, 54-63, doi:10.1016/j.icarus.2013.09.025.

Feely, K. and P. R. Christensen (1999), Quantitative compositional analysis using thermal emission spectroscopy: Application to igneous and metamorphic rocks, *J. Geophys. Res., 104*(E10), 24,195-24,210.

Forget, F., R. M. Haberle, F. Montmessin, B. Levrard, and J. W. Head (2006), Formation of glaciers on Mars by atmospheric precipitation at high obliquity, *Science, 311*, 368-371.

Fortner, S. K., M. Tranter, A. Fountain, W. Berry Lyons and K. A. Welch (2005), The geochemistry of supraglacial streams of Canada Glacier, Taylor Valley (Antarctica), and their evolution into proglacial waters, *Aquatic Geochemistry, 11*, 391-412.

Gillespie, A. R., A. B. Kahle, and R. E. Walker (1986), Color enhancement of highly correlated images. I. Decorrelation and HIS contrast stretches. *Remote Sens. Environ., 20*, 209-235.

Gillespie, A. R. (1992), Spectral mixture analysis of multispectral thermal infrared images, *Remote Sens. Environ., 42*, 137-145.

Gillespie, A. R., T. Matsunaga, S. Rokugawa, and S. J. Hook (1998), Temperature and emissivity separation from Advanced Spaceborne Thermal Emission and Reflection Radiometer (ASTER) images, *IEEE Transactions on Geoscience and Remote Sensing*, 36, 1113-1126, doi:10.1109/36.700995.

Glotch, T. D., R. V. Morris, P. R. Christensen, and T. G. Sharp (2004), Effect of precursor mineralogy on the thermal infrared emission spectra of hematite: Application to Martian hematite mineralization, *J. Geophys. Res., 109*(E07003).

Goldstein, J. I., D. E. Newbury, P. Echlin, D. C. Joy, C. Fiori, and E. Lifshin (1981) *Scanning Electron Microscopy and X-ray Microanalysis*, Plenum, New York, 673 p.

Hallet, B. (1975), Subglacial silica deposits, *Nature*, *254*, 682.

Hallet, B. (1976), Deposits formed by subglacial precipitation of CaCO3, *Geological Society of America Bulletin, 87*(7), 1003–1015.

Hamilton, V. E., P. R. Christensen, and H. Y. McSween (1997), Determination of Martian meteorite lithologies and mineralogies using vibrational spectroscopy, *J. Geophys. Res., 102*(E11), 25,593-25,603.

Hamilton, V. E., and P. R. Christensen (2000), Determining the modal mineralogy of mafic and ultramafic igneous rocks using thermal emission spectroscopy, *J. Geophys. Res., 105*(E4), 9717-9733.

Hamilton, T. L., J. W. Peters, M. L. Skidmore, and E. S. Boyd (2013), Molecular evidence for an active endogenous microbiome beneath glacial ice, *Intl. Soc. Microbio. Eco. J., 7*, 1402-1412.

Havig, J. R., J. Raymond, D. Meyer-Dombard, N. Zolotova, E. L. Shock (2011), Merging isotopes and community genomics in a siliceous sinter-depositing hot spring, *Journal of Geophysical Research, 116*, G01005, doi:10.1029/2010JG001415.

Head, J. W., J. F. Mustard, M. A. Kreslavsky, R. E. Milliken, and D. R. Marchant (2003), Recent ice ages on Mars, *Nature, 426*, 797-802.

Head, J. W., G. Neukum, R. Jaumann, H. Hiesinger, E. Hauber, M. Carr, P. Masson, B. Foing, H. Hoffmann, and M. Kreslavsky (2005), Tropical to mid-latitude snow and ice accumulation, flow and glaciation on Mars, *Nature*, *434*(7031), 346–351.

Hodgkins, R., M. Tranter, and J. A. Dowdeswell (1997), Solute provenance, transport, and denudation in a high Arctic glacierized catchment, *Hydrological Processes, 11*, 1813-1832.

Hodson, A. P. Porter, A. Lowe, and P. Mumford (2002), Chrmical denudation and silicate weathering in Himalayan glacier basins: Batura Glacier, Pakistan, *J. Hydrol., 262*, 193-208.

Holt, J. W., A. Safaeinili, J. J. Plaut, J. W. Head, R. J. Phillips, R. Seu, S. D. Kempf, P. Choudhary, D. A. Young, N. E. Putzig, D. Biccari, and Y. Gim (2008), Radar Sounding Evidence for Buried Glaciers in the Southern Mid-Latitudes of Mars, *Science*, *322*(5), 1235–1238, doi:10.1126/science.1164246.

Hook, S. J., E. A. Abbott, C. Grove, A. B. Kahle, and F. Palluconi (1999), Use of multispectral thermal infrared data in geological studies, in Rencz, A. N., ed., *Remote Sensing for the Earth sciences, Manual of Remote Sensing*, Vol. 3 (third edition), New York, John Wiley and Sons, Inc., 59-110.

Kahle, A. B., F. D. Palluconi, S. J. Hook, V. J. Realmuto and G. Bothwell (1991), The Advanced Spaceborne Thermal Emission and Reflectance radiometer (ASTER), *International Journal of Imaging System Technology, 3*, 144-156.

Lafrenière, M. J. and M. J. Sharp (2005), A comparison of solute fluxes and sources from glacial and non-glacial catchments over contrasting melt seasons, *Hydrol. Process., 19*, 2991-3012, doi:10.002/hyp.5812.

Lane, M. D., M. D. Dyar, J. L. Bishop, P. L. King, and E. Cloutis (2006), Laboratory emission, visible-near infrared, and Mössbauer spectroscopy of iron sulfates: Application to the bright Paso Robles soils in Gusev crater, Mars, *Lunar and Planetary Science XXXVII, Abstract 1799*, Lunar and Planetary Institute, Houston.

Levy, J. S., J. W. Head, and D. R. Marchant (2009), Concentric crater fill in Utopia Planitia : History and interaction between glacial "brain terrain" and periglacial mantle processes, *Icarus, 202*, 462-476, doi:10.1016/j.icarus.2009.02.018.

Levy, J. S., C. I. Fassett, J. W. Head, C. Schwartz, and J. L. Watters (2014), Sequestered glacial ice contribution to the global Martian water budget: Geometric constraints on the volume of remnant, midlatitude debris-covered glaciers, *J. Geophys. Res. Planets, 119*, doi:10.1002/2014JE004685.

Lucchitta, B.K (1981) Mars and Earth: Comparison of cold-climate features, *Icarus, 45*, 264-303.

Marzeion B., J. G. Cogley, K. Richter, and D. Parkes (2014), Attibution of global glacier mass loss to anthropogenic and natural causes, *Science, 345*, 919-921, doi:10.1126/science.1254702.

McDowell, M. L. and V. E. Hamilton (2009), Seeking phyllosilicates in thermal infrared data: A laboratory and Martian data case study, *J. Geophys. Res., 114*(E06007), doi:10.1029/2008JE003317.

McLaren, D. J. and E. W. Mountjoy (1962), Alexo equivalents in the Jasper area, *Geological Survey of Canada*, Paper 62-63, 36 p.

McMechan, M. E. (1988), *Geology of Peter Lougheed Provincial Park, Rocky Mountain Front Ranges, Alberta.* Open Field Report 2097. Geological Survey of Canada.

Michalski, J. R., M. D. Kraft, T. Deidrich, T. G. Sharp, and P. R. Christensen (2003), Thermal emission spectroscopy of the silica polymorphs and considerations for remote sensing of Mars, *Geophys. Res. Lett.*, *30*(19), doi:10.1029/2003GL018354.

Michalski, J. R., S. J. Reynolds, T. G. Sharp, and P. R. Christensen (2004), Thermal infrared analysis of weathered granitic rock compositions in the Sacaton Mountains, Arizona: Implications for petrologic classifications from thermal infrared remote-sensing data, *J. Geophys. Res, 109*, E03007, doi:10.1029/2003JE002197.

Michalski, J. R., M. D. Kraft, T. G. Sharp, and P. R. Christensen (2006), Effects of chemical weathering on infrared spectra of Columbia River Basalt and spectral interpretations of martian alteration, *Earth and Planetary Science Letters, 248*, 822-829, doi:10.1016/j.epsl.2006.06.034.

Mitchell, A., G. H. Brown, and R. Fuge (2001), Minor and trace element export from a glacierized Alpine headwater catchment (Haut Glacier d'Arolla, Switzerland). *Hydrological Processes, 15,* 3499-3524, doi:10.1002/hyp.1041.

Mitchell, A. C., M. J. Lafreniere, M. L. Skidmore, and E. S. Boyd (2013), Influence of bedrock mineral composition on microbial diversity in a subglacial environment, *Geology*, 1–43.

Morse, J. W. and R. S. Arvidson (2002), The dissolution kinetics of major sedimentary carbonate minerals, *Earth Sci. Rev., 58*, 51-84.

Parsons, R. L. and J. W. Head (2005) Ascraeus Mons fan-shaped deposit, Mars: Geological history and volcano-ice interactions of a cold-based glacier, *Lunar Planet. Sci. XXXVI*, Abs. 1139.

Piatek, J. L. and J. E. Moersch (2007), Thermophysical analysis of debris aprons in eastern Hellas using THEMIS, *Lunar Planet. Sci. XXXVIII,* Abs. 2281.

Pierce, T. L. and Crown, D. A. (2003), Morphologic and topographic analyses of debris aprons in the eastern Hellas region, Mars, *Icarus, 163*, 46-65, doi:10.1016/S0019-1035(03)00046-0.

Plaut, J. J., A. Safaeinili, J. W. Holt, R. J. Phillips, J. W. Head, R. Seu, N. E. Putzig, and A. Frigeri (2009), Radar evidence for ice in lobate debris aprons in the mid-nothern latitudes of Mars, *Geophys. Res. Lett., 36*(L02203), doi :10.1029/2008GL036379.

Raiswell, R., Benning, L.G., Davidson, L., Tranter, M., and S. Tulaczyk (2009), Schwertmannite in wet, acid, and oxic microenvironments beneath polar and polythermal glaciers, *Geology*, *37*, 431-434, doi:10.1130/G25350A.1.

Rampe, E. B., M. D. Kraft, T. G. Sharp, D. C. Golden, D. W. Ming, and P.R. Christensen (2012), Allophane detection on Mars with Thermal Emission Spectrometer data and implications for regional-scale chemical weathering processes, *Geology*, *40*(11), 995-998, doi:10.1130/G33215.1.

Rampe, E. B., M. D. Kraft, and T. G. Sharp (2013), Deriving chemical trends from thermal infrared spectra of weathered basalts: Implications for remotely determining chemical trends on Mars, *Icarus*, *225*, 749-762.

Ramsey, M. S., and P. R. Christensen (1998), Mineral abundance determination: Quantitative deconvolution of thermal emission spectra, *J. Geophys. Res., 103*, 577-596.

Ramsey, M. S., P. R. Christensen, N. Lancaster, and D. A. Howard (1999), Identification of sand sources and transport pathways at the Kelso Dunes, California, using thermal infrared remote sensing, *Geol. Soc. Am. Bull., 111*(5), 646-662.

Reimer, L. (1985), Scanning Electron Microscopy, Physics of Image Formation and Microanalysis, *Spring Series in Optical Sciences, 45*, Springer, Berlin.

Rockwell, B. W. and A. H. Hofstra (2008), Identification of quartz and carbonate minerals across northern Nevada using ASTER thermal infrared emissivity data – Implications for geologic mapping and mineral resource investigations in well-studied and frontier areas, *Geosphere, 4*(1), 218-246.

Ruff, S. W., P. R. Christensen, P. W. Barbera, and D. L. Anderson (1997), Quantitative thermal emission spectroscopy of minerals: A technique for measurement and calibration, *J. Geophys. Res., 102*, 14,899-14,913.

Ruff, S. W. (1998), Quantitative thermal emission spectroscopy applied to granitoid petrology, Ph.D. dissertation, Ariz. State Univ., Tempe.

Rutledge, A.M. and P.R. Christensen (2012), Infrared spectroscopy of subglacial and englacial weathering products in a silicate-carbonate system, *Intl. Glac. Soc. Symposium*, Abstract 63A250.

Rutledge, A. M., C. S. Edwards, and P. R. Christensen (2013), Glacially-developed weathering rinds at the micro-scale: Mineralogy and chemistry. Abstract EP13B-0871 presented at *2013 Fall Meeting, AGU*, San Francisco, Calif., 9-13 Dec.

Salisbury, J. W. and D. M. D'Aria (1992), Infrared (8-14μm) remote sensing of soil particle size, *Remote Sens. Environ., 42*, 157-165, doi:10.1016/0034-4257(92)90099-6.

Sharma, S., A. Sack, J. P. Adams, D. J. Vesper, R. C. Capo, A. Hartsock, and H. M.

Edenborn (2013), Isotopic evidence of enhanced carbonate dissolution at a coal mine drainage site in Allegheny County, Pennsylvania, USA, *Appl. Geochem., 29*, 32-42.

Sharp, M., M. Tranter, G. H. Brown, and M. Skidmore (1995), Rates of chemical denudation and CO2 drawdown in a glacier-covered alpine catchment, *Geology, 23*, 61-64.

Sharp M., J. Parkes, B. Cragg, I. J. Fairchild, H. Lamb, and M. Tranter (1999), Widespread bacterial populations at glacier beds and their relationship to rock weathering and carbon cycling, *Geology 27*(2), 107–110.

Sharp, M., R. A. Creaser, and M. Skidmore (2002), Strontium isotope composition of runoff from a glaciated carbonate terrain, *Geochimica et Cosmochimica Acta, 66*(4), 595-614, doi:10.1016/S0016-7037(01)00798-0.

Shock, E., M. Holland, D. Meyer-Dombard, J. P. Amend, G. R. Osburn, and T.P. Fischer (2010), Quantifying inorganic sources of geochemical energy in hydrothermal ecosystems, Yellowstone National Park, U.S.A., *Geochimica et Cosmochimica Acta, 74*, 4005-4043.

Skidmore, M. L., J. M. Foght, and M. J. Sharp (2000), Microbial life beneath a high Arctic glacier, *App. Environ. Microbiol*, *66*(8), 3214–3220.

Skidmore M., S. P. Anderson, M. Sharp, J. Foght, and B. D. Lanoil (2005), Comparison of microbial community compositions of two subglacial environments reveals a possible role for microbes in chemical weathering processes, *App. Environ. Microbiol.*, *71*(11), 6986–6997.

Squyres, S. W. (1984), The history of water on Mars, *Ann. Rev. Earth Planet. Sci., 12*, 83-106.

Switzer, S. B., W. G. Holland, D. S. Christie, G. C. Graf, A. S. Hedinger, R. J., McAuley, R. A. Wierzbicki, and J. J. Packard (2012), Devonian Woodbend-Winterburn strata of the Western Canada Sedimentary Basin, in *Geological Atlas of the Western Canada Sedimentary Basin*, Alberta Geological Survey.

Szynkiewicz, A., M. Modelska, S. Buczyński, D. M. Borrok, and J. P. Merrison (2013), The polar sulfur cycle in the Werenskioldbreen, Spitsbergen: Possible implications for understanding the deposition of sulfate minerals in the North Polar Region of Mars, *Geochimica et Cosmochimica Acta*, *106*(C), 326–343, doi:10.1016/j.gca.2012.12.041.

Tanaka, K. L. and G. J. Leonard (1995), Geology and landscape evolution of the Hellas region of Mars, *J. Geophys. Res., 100*(E3), 5407-5432.

Thorn, C. E., R. G. Darmody, J. C. Dixon, and P. Schylter (2001), The chemical weathering regime of Kärkevagge, Arctic alpine Sweden, *Geomorphology, 41*, 37-52.

Thorn, C. E., R. G. Darmody, S. W. Campbell, C. E. Allen, and J. C. Dixon (2007), Microvariability in the early stages of cobble weathering by microenvironment on a glacier foreland, Storbreen, Jotunheimen, Norway, *Earth Surf. Process. Landforms, 32*, 2199-2211, doi:10.1002/eps.1528.

Tranter, M., Brown, G.H., Hodson, A.J. and A. Gurnell (1996), Hydrochemistry as an indicator of subglacial drainage system structure: a comparison of alpine and sub-polar environments, *Hydrological Processes, 10*, 541-556.

Tranter, M., M. J. Sharp, H. R. Lamb, G. H. Brown, B. P. Hubbard, and I. C. Willis (2002), Geochemical weathering at the bed of Haut Glacier d'Arolla, Switzerland – a new model, *Hydrological Processes, 16*, 959-993.

Tranter, M. (2003), Geochemical weathering in glacial and proglacial environments, in *Surface and Ground Water, Weathering, and Soils*, ed. J. I. Drever, 5, 189-205, *Treatise on Geochemistry*, ed. H. D. Lamb and K. K. Turekian, Oxford, Elsevier-Pergamon.

Tricart, J. (1969), *Geomorphology of Cold Environments*, McMillan, London.

Vincent, R. K., and F. Thompson (1972), Spectral compositional imaging of silicate rocks, *J. Geophys. Res.*, *77*, 2465-2472.

Wadham, J. L., R. J. Cooper, M. Tranter, and S. Bottrell (2007), Evidence for widespread anoxia in the proglacial zone of an Arctic glacier, *Chemical Geology, 243*(1), 1–15, doi:10.1016/j.chemgeo.2007.04.010.

Washburn, A. L. (1979) *Geocryology, A Survey of Periglacial Processes*, Edward Arnold, London, 406 p.

Whalley, W. B., A. F. Gellatly, J. E. Gordon, and J. D. Hansom (1990), Ferromanganese rock varnish in North Norway: a subglacial origin, *Earth Surface Processes and Landforms*, *15*(3), 265–275.

Wyatt, M. B., V. E. Hamilton, H. Y. J. McSween, P. R. Christensen, and L. A. Taylor (2001), Analysis of terrestrial and Martian volcanic compositions using thermal emission spectroscopy: 1. Determination of mineralogy, chemistry, and classification strategies, *J. Geophys. Res., 106*(E7), 14,711-14,732.

Yamaguchi, Y., A. Kahle, H. Tsu, T. Kawakami, and M. Pniel (1998), Overview of the Advanced Spaceborne Thermal Emission and Reflectance Radiometer (ASTER),

IEEE Transactions on Geoscience and Remote Sensing, 36, 1062-1071, doi:10.1109/36.700991.

APPENDIX A

WATER CHEMISTRY OF ROBERTSON GLACIER

Table A.1 Water chemistry of Robertson Glacier

Sample	Location	pH	T (°C)
2009 season			
090914A	Primary glacial outwash ~20 m from edge of glacier	8.784	0.3
090914B	Pore water from 090914A	nd	nd
090914C	East-side outflow	8.713	0.1
090914D	Field blank	nd	nd
090915E	Subglacial flow, east side	8.774	0.2
090915F	Supraglacial water middle of glacier	8.597	0.1
090915G	Flowing yet ponded melt water east portion of glacier	8.35	0.1
090915H	Melted glacial ice	nd	nd
2010 season			
101014A	Outwash at glacier edge (primary outwash)	8.087	0.2
101014B	Filament Crick (side seep fed by subsurface ice)	8.18	3.8
101015C	Field Station Fresh Snow (snowfall in night/AM)	4.954	3.7
101015D	Blank (collected at Field Station)	nd	nd
101016E	Outwash at glacier edge (same place as 101014A)	8.082	0.1
101016F	Glacial Outwash at treeline (~2.5 miles from glacier)	8.104	0.8
101016G	Glacier ice	8.81	21*
101016H	Local Snow at glacier	9.049	21.2*
2011 season			
110925A	Subglacial seds with supraglacial outflow	8.56	0.3
110925B	Cryoconite sample	8.209	0.1
110925C	Supraglacial outflow	8.393	0.1
110925D	Filament Creek	7.994	2.9
110926E	Subglacial runoff	8.374	0
110927F	Filament Dew	8.011	2.2
110927G	Filament Tree	8.123	2.6
110929I	Equipment blank (DI in the lab)	nd	nd

* Collected after melting ice over stove.
nd = not detected

Table A.1 (cont'd) Water chemistry of Robertson Glacier

Sample	Ca^{+2}	Mg^{+2}	Na^{+}	Ni^{+2}	K^{+}	Fe
	(mol/kg)					
2009 season						
090914A	3.64E-04	4.41E-05	7.09E-06	5.11E-09	4.70E-06	2.12E-05
090914B	4.49E-04	6.15E-05	2.65E-05	1.82E-08	1.12E-05	5.17E-05
090914C	3.57E-04	3.81E-05	bdl	5.11E-09	bdl	4.35E-04
090914D+	2.73E-05	bdl	bdl	7.84E-09	bdl	2.61E-05
090915E	3.59E-04	3.01E-05	bdl	2.73E-08	bdl	1.83E-04
090915F	2.48E-04	7.62E-06	bdl	2.21E-09	bdl	1.49E-05
090915G	5.40E-04	7.82E-05	4.69E-06	3.75E-09	7.11E-06	2.01E-04
090915H	1.35E-04	bdl	4.67E-06	1.33E-08	bdl	8.95E-05
2010 season						
101014A	6.75E-04	2.84E-04	6.56E-06	1.94E-08	7.25E-06	1.61E-08
101014B	7.20E-04	4.48E-04	8.06E-06	6.99E-09	1.52E-05	1.79E-08
101015C	3.49E-06	bdl	3.96E-06	1.87E-08	bdl	3.17E-08
101015D+	bdl	bdl	bdl	1.36E-09	bdl	5.91E-09
101016E	5.95E-04	2.45E-04	4.28E-06	1.19E-09	7.08E-06	1.45E-08
101016F	8.25E-04	4.39E-04	5.54E-06	1.53E-09	7.57E-06	1.56E-08
101016G	9.86E-05	4.77E-06	5.83E-07	2.39E-09	bdl	2.76E-08
101016H	5.58E-05	bdl	8.10E-06	9.88E-09	5.19E-06	4.60E-08
2011 season						
110925A	4.05E-04	6.05E-05	4.84E-06	7.33E-09	bdl	2.85E-08
110925B	2.40E-04	1.06E-05	5.42E-05	4.43E-09	bdl	3.28E-07
110925C	2.90E-04	1.77E-05	6.32E-05	2.42E-09	bdl	6.45E-08
110925D	4.72E-04	4.86E-04	1.12E-05	5.03E-09	2.05E-05	1.37E-08
110926E	3.90E-04	1.29E-04	1.20E-05	5.33E-09	4.92E-06	2.04E-08
110927F	5.59E-04	5.44E-04	2.94E-05	6.44E-09	1.13E-05	3.12E-08
110927G	3.83E-04	1.17E-04	3.84E-05	5.45E-09	bdl	4.83E-08
110929H	1.84E-04	1.15E-05	6.77E-06	2.08E-09	5.31E-06	1.04E-08
110929I+	bdl	bdl	1.06E-05	9.88E-10	bdl	1.86E-08

"+" = field blank

Table A.1 (cont'd) Water chemistry of Robertson Glacier

Sample	NH_4^+	Cu	Zn	Mo	Li	Al
			(mol/kg)			
2009 season						
090914A	bdl	7.40E-09	1.04E-08	2.40E-09	6.34E-07	6.12E-07
090914B	3.38E-06	4.42E-08	1.99E-08	1.07E-08	1.55E-06	8.97E-07
090914C	bdl	1.46E-08	2.29E-08	2.61E-09	6.34E-07	3.11E-06
090914D+	bdl	4.25E-07	7.65E-08	3.13E-09	1.48E-07	1.82E-06
090915E	bdl	4.25E-08	4.89E-08	1.77E-09	6.56E-07	5.41E-07
090915F	bdl	5.98E-09	6.42E-08	2.29E-09	6.05E-07	7.41E-07
090915G	bdl	8.81E-09	1.84E-08	5.63E-09	6.48E-07	7.52E-07
090915H	bdl	1.35E-08	2.60E-08	7.09E-10	6.05E-07	6.56E-07
2010 season						
101014A	bdl	5.98E-09	4.43E-08	1.15E-08	3.86E-07	5.52E-07
101014B	bdl	2.05E-09	2.75E-08	1.29E-08	4.03E-07	7.08E-07
101015C	bdl	4.25E-08	1.21E-07	2.08E-09	2.16E-07	2.59E-07
101015D+	bdl	2.20E-09	4.89E-08	5.11E-10	1.22E-07	1.07E-07
101016E	bdl	7.87E-10	1.97E-08	1.36E-09	4.28E-07	2.63E-07
101016F	bdl	7.40E-10	3.06E-08	1.04E-09	3.65E-07	2.59E-07
101016G	bdl	1.02E-09	3.52E-08	1.25E-09	2.98E-07	1.22E-06
101016H	2.39E-06	2.68E-09	5.20E-08	1.56E-08	2.13E-07	3.04E-07
2011 season						
110925A	bdl	2.00E-09	5.96E-09	8.23E-09	1.25E-07	2.82E-07
110925B	2.88E-06	5.05E-09	7.34E-08	2.92E-10	1.12E-07	8.75E-07
110925C	bdl	2.30E-09	2.63E-08	2.81E-10	1.05E-07	2.11E-07
110925D	bdl	6.61E-09	8.76E-08	8.96E-09	3.27E-07	2.13E-07
110926E	bdl	4.48E-09	2.22E-08	5.43E-09	2.31E-07	2.15E-07
110927F	bdl	6.92E-09	6.41E-08	7.30E-09	8.36E-07	2.52E-07
110927G	bdl	1.48E-08	7.34E-08	3.34E-10	5.19E-07	4.45E-07
110929H	3.21E-06	1.29E-09	6.42E-08	8.96E-10	4.47E-07	1.67E-07
110929I+	bdl	4.56E-10	2.80E-07	6.78E-10	1.70E-07	2.04E-07

"+" = field blank

Table A.1 (cont'd) Water chemistry of Robertson Glacier

Sample	Cl^-	SO_4^{-2}	S	DIC
	(mol/kg)			
2009 season				
090914A	5.54E-06	7.51E-05	6.05E-06	4.76E-04
090914B	2.47E-05	8.21E-05	bdl	7.30E-04
090914C	1.44E-06	3.33E-05	8.05E-06	5.20E-04
090914D+	bdl	bdl	bdl	5.20E-05
090915E	3.00E-06	2.28E-05	3.56E-06	6.03E-04
090915F	1.72E-06	1.25E-06	4.37E-07	4.05E-04
090915G	3.17E-06	5.47E-05	4.99E-07	8.96E-04
090915H	4.10E-06	7.45E-07	bdl	1.54E-04
2010 season				
101014A	2.85E-06	5.71E-04	3.12E-07	9.94E-04
101014B	4.01E-06	4.03E-04	2.18E-07	1.92E-03
101015C	7.20E-06	2.00E-06	bdl	9.82E-06
101015D+	bdl	6.25E-08	bdl	1.03E-05
101016E	2.40E-06	4.61E-04	5.30E-07	9.94E-04
101016F	4.17E-06	5.31E-04	bdl	1.78E-03
101016G	4.25E-06	2.94E-06	bdl	1.60E-04
101016H	1.36E-05	4.56E-06	bdl	8.61E-05
2011 season				
110925A	4.27E-06	1.11E-04	1.03E-06	6.37E-04
110925B	3.16E-05	5.74E-06	1.88E-05	3.22E-04
110925C	8.61E-06	1.76E-06	3.74E-07	4.64E-04
110925D	4.17E-06	3.91E-04	3.74E-07	1.73E-03
110926E	2.41E-06	1.87E-04	2.49E-06	5.88E-04
110927F	1.09E-05	4.46E-04	5.93E-07	2.21E-03
110927G	7.05E-06	6.53E-05	2.18E-07	6.88E-04
110929H	1.28E-05	3.26E-06	bdl	3.35E-04
110929I+	2.90E-06	5.29E-07	bdl	3.15E-05

"+" = field blank

Table A.1 (cont'd) Water chemistry of Robertson Glacier

Sample	SiO2(aq)	F^-	PO_4^{-3}	NO_3^-
		(mol/kg)		
2009 season				
090914A	8.82E-05	5.71E-07	bdl	2.04E-06
090914B	bdl	1.68E-05	bdl	7.60E-06
090914C	7.66E-05	3.16E-06	bdl	2.97E-06
090914D+	bdl	bdl	bdl	bdl
090915E	1.45E-04	4.61E-07	bdl	bdl
090915F	6.82E-05	6.84E-08	bdl	bdl
090915G	7.99E-05	8.79E-06	bdl	2.52E-06
090915H	bdl	1.63E-06	bdl	
2010 season				
101014A	7.32E-05	2.47E-06	bdl	1.39E-05
101014B	5.74E-04	3.05E-06	bdl	1.62E-05
101015C	bdl	2.84E-06	bdl	3.14E-06
101015D+	bdl	3.37E-07	bdl	bdl
101016E	1.78E-04	2.26E-06	bdl	1.37E-05
101016F	7.16E-05	2.37E-06	bdl	1.00E-05
101016G	bdl	1.03E-05	bdl	2.90E-07
101016H	6.16E-05	6.00E-06	bdl	7.42E-06
2011 season				
110925A	bdl	3.86E-06	bdl	1.02E-06
110925B	bdl	4.13E-06	bdl	6.75E-06
110925C	bdl	2.34E-07	bdl	6.94E-07
110925D	bdl	2.93E-06	2.10E-06	2.29E-05
110926E	bdl	1.85E-06	bdl	5.93E-06
110927F	bdl	1.08E-06	bdl	8.62E-06
110927G	bdl	8.87E-07	bdl	4.71E-06
110929H	bdl	3.49E-05	2.09E-07	6.54E-07
110929I+	bdl	2.61E-07	bdl	3.37E-07

"+" = field blank

APPENDIX B

LITHOLOGIC SAMPLES FROM ROBERTSON GLACIER

Table B.1. Rock samples from Robertson Glacier

Location	Sample	Inferred lithologic unit
Supraglacial	110922Ai*	Sassenach
	110922Ai2	Sassenach
	110922Bi*	Sassenach
	110922Bii	Mount Hawk
	110922Bii2	Sassenach
	110921Ci*	Mount Hawk
	110922Ci*	Palliser
	110922Ci2	Mount Hawk
	110922Cii*	Sassenach
	110922Cii2	Palliser
	110922Di*	Palliser
	110922Di2	Sassenach
	110922Ei*	Sassenach
	110922Eii	Sassenach
	110922Fi*	Sassenach
	110922Fi2	Sassenach
	110922Gi*	Sassenach
	110922Gi2	Sassenach
	110922Hi*	Sassenach
	110922Hi2	Sassenach
	110922Hii	Palliser
	110922I*	Sassenach
	110922I2	Sassenach
	110922J*	Sassenach
	110922J2	Mount Hawk
	110921Ci	Palliser
	110921C_fresh*	Mount Hawk
	110921Ciii	Sassenach
	101014D1	Sassenach
	101014E1	Sassenach
	101014E2	Mount Hawk
	101014E3	Palliser
	101014D1sed*	Palliser
	101014Bsed*	Palliser
	101014Dsed*	Palliser

*sample too small to bisect with rock saw

Table B.1. (cont'd) Rock samples from Robertson Glacier

Location	Sample	Inferred lithologic unit
Subglacial	110921Ai*	Palliser
	110921Ai2	Sassenach
	110921Ai3	Sassenach
	110921Aii*	Mount Hawk
	110921Aii2	Mount Hawk
	110921Aii3	Palliser
	110921Aiv*	Palliser
	110921Bi	Mount Hawk
	110921Bi2	Mount Hawk
	110921Bii*	Palliser
	110921Bii2	Sassenach
	110921Bii3	Sassenach
	110921Biv*	Palliser
	110921Biv2	Mount Hawk
	101016H1	Sassenach
	101016I	Mount Hawk
Proglacial	101014C2	Mount Hawk
	101016K1	Palliser
	101014C1	Palliser
	101014B1	Mount Hawk
	101014A3	Sassenach
	101014A2	Mount Hawk
	101014A4	Palliser
	101014A1*	Mount Hawk
	101014C2*	Mount Hawk
	101016K*	Mount Hawk
	101014B6*	Mount Hawk
	101014C1*	Sassenach
	101014B3*	Mount Hawk
	101014x*	Mount Hawk
	101014xp*	Mount Hawk
	110923Bsed*	Palliser
	110921Aiiised*	Palliser

*sample too small to bisect with rock saw